Queen Mary University of London

School of Physics and Astronomy

Submitted in partial fulfillment of the requirements of the Degree of Doctor of Philosophy

Time-dependent CP violation in charm mesons

Author:
Gianluca Inguglia

Supervisor:
Dr. Adrian Bevan
co-Supervisor:
Dr. Marcella Bona

Statement of Originality

I, Gianluca Inguglia, confirm that the research included within this thesis is my own work or that where it has been carried out in collaboration with, or supported by others, that this is duly acknowledged below and my contribution indicated. Previously published material is also acknowledged below.

I attest that I have exercised reasonable care to ensure that the work is original, and does not to the best of my knowledge break any UK law, infringe any third partys copyright or other Intellectual Property Right, or contain any confidential material.

I accept that the College has the right to use plagiarism detection software to check the electronic version of the thesis.

I confirm that this thesis has not been previously submitted for the award of a degree by this or any other university.

The copyright of this thesis rests with the author and no quotation from it or information derived from it may be published without the prior written consent of the author.

Signature: Gianluca Inguglia
Date: 11/02/2014

Details of collaboration and publications:
Super$B$ Collaboration,
Arachnid Collaboration;

A. J. Bevan, G. Inguglia, B. Meadows. Time-dependent CP asymemtries in D and B decays. Phys. Rev. D**84**, 114009 (2011) [arXiv:1106.5075 [hep-ph]].
Super$B$ Collaboration. Super$B$ technical design report. ArXiv: 1306.5655 [Hep-ex] (2013).

A. J. Bevan, G. Inguglia, M. Zoccali. Neutral meson tests of time-reversal symmetry invariance. ArXiv: 1302.4191 (2013).

This work is dedicated to Fabiola Gianotti, the person who put me in right mindset a few years ago to undertake this exceptional adventure into the world of particle physics. When you have a dream, you should not let it go away from you but you must believe that it is possible for it to come true, and then you have to work hard to make it happen.

Abstract

CP violation is a well established phenomenon for B and K mesons, but for D^0 mesons, bound states made up of a quark-antiquark pair containing a charm quark, a conclusive answer to the question whether there is CP violation or not, has yet to be determined. I show here the phenomenology of time-dependent CP asymmetries in charm decays, and discuss the implications of experimental tests aimed at the measurement of CP violation in the interference between mixing and decays of charm mesons, in particular when studying the decay channels $D^0 \to h^+h^-$ ($h = K, \pi$). The decay channels considered can also be used to constrain quantities that are poorly measured or still to be investigated, such as ϕ_{MIX} and $\beta_{c,eff}$, provided that the effects of penguin pollution are ignored. I considered correlated production of D^0 mesons at the Super$B$ experiment and its planned asymmetric run at the charm threshold and performed a study of simulated events, finding that a boost factor $\beta\gamma = 0.28$ would not be sufficient to produce competitive results; the desirable resolution on the decay vertex separation between two D mesons in an event can be obtained with $\beta\gamma = 0.9$. Vertex detectors play the major role in this analysis and new vertex detectors with high granularity might help improving these studies. The reference pixels (25×25 μm pixel sensors implementing a 4T architecture with a deep n-well implant) of the Cherwell sensor, studied within the ARACHNID Collaboration, might be a candidate as a vertexing/tracking system, in particular for the layers of an SVT which are just around the beam pipe. I show the results of a study performed with data collected during a test beam at CERN, where the Cherwell sensor has been irradiated with pion beams, in terms of the charge deposited in the pixels by the charged particles passing through it, and show that this is mostly collected by the eight pixels ring surrounding the pixel hit by the particle beam. This work culminates in the definition of the clustering algorithm used by ARACHNID.

Acknowledgements

I would like to thank first of all my supervisor, Adrian Bevan. It has been a very enriching experience working with you in the past three years, looking back at when I first arrived at Queen Mary University of London I would have never expected to write a thesis all based on original work on phenomenology, experimental techniques, and hardware studies. All of this was possible simply because you are an amazing physicist.
I also want to thank Brian Meadows for all his important suggestions during preparation of papers, talks and proceedings, and Tamsin and James for the very kind collaboration and support for the hardware studies, also during Christmas!
It was a very nice experience to work in the Super$B$ and ARACHNID Collaborations, and I wish to thank all the people who are or were involved in these Collaborations for all the time spent together in sorting out solutions to any kind of problem faced in the last years related to my research.
I want to thank Queen Mary University of London for financial support during my studies and in particular for covering all my travel expenses to various destination for my participation at international conferences and Collaboration meetings.
Finally I want to thank the hundreds of people I crossed path with all over the world during these years.

"O frati," dissi, "che per cento milia
perigli siete giunti a l'occidente,
a questa tanto picciola vigilia
d'i nostri sensi ch' del rimanente
non vogliate negar l'esperenza
di retro al sol, del mondo sanza gente.
Considerate la vostra semenza:
fatti non foste a viver come bruti,
ma per seguir virtute e canoscenza[1]*."*

Dante Alighieri, Divina Commedia,
Inferno XXVI.

[1] "O brothers!" I began, "woe to the west through perils without number now have we reach'd; to this the short remaining watch, that yet our senses have to wake, refuse not proof of the unpeopled world, following the track of Phoebus. Call to mind from whence ye sprang: ye were not form'd to live the life of brutes, but virtue to pursue and knowledge high."

Contents

List of Figures

List of Tables

Chapter 1

Introduction

Today the Big Bang theory is considered the model that describes the evolution of the Universe we live in, and on this basis the Universe should have contained equal amounts of matter and antimatter[1] at the time of the big bang 13.7 billion years ago. Since all the experiments aimed at searching for antimatter in the Universe have measured a very small presence of this with respect to ordinary matter, scientists then conclude that a physical mechanism that favours matter over antimatter has to exist now and in particular during the first instants of the Universe itself. This mechanism is referred to as CP violation and the possibility to relate this with the observed matter-antimatter asymmetry was realised by A. Sakharov [1].

1.1 Discrete quantum operators

In quantum mechanics CP represents a discrete operator which is the combination of the *charge conjugation* operator C, and the *parity* operator P. Parity, often called mirror symmetry, represents the discrete symmetry of the law of physics with respect to the inversion of spatial coordinates, and charge conjugation represents the transformation of a particle into its antiparticle.

[1] Very often one can find in the literature describing the Big Bang theory expressions like "the Universe has been created with equal amounts of matter and antimatter". I refuse to adopt this expression on this thesis, due to fact that I prefer to keep the word creation for other fields such as philosophy.

When these operators act on a wave function $\Psi(r,t)$ they transform it as follows:

$$C|\Psi(r,t)\rangle = e^{+i\phi_C}|\Psi^*(r,t)\rangle. \tag{1.1}$$

$$P|\Psi(r,t)\rangle = e^{+i\phi_P}|\Psi(-r,t)\rangle, \tag{1.2}$$

The combination of the C and P operators is given by the CP operator and this acts on a wave function as follows:

$$CP|\Psi(r,t)\rangle = e^{+i\phi_{CP}}|\Psi^*(-r,t)\rangle, \tag{1.3}$$

and

$$CP|\Psi^*(r,t)\rangle = e^{-i\phi_{CP}}|\Psi(-r,t)\rangle. \tag{1.4}$$

A third important discrete symmetry exists, that of time reversal, which is denoted by T and when applied to a wave function this transforms as

$$T|\Psi(r,t)\rangle = e^{+i\phi_T}|\Psi(r,-t)\rangle. \tag{1.5}$$

It was believed that the combination of the operators C and P was a symmetry of nature, until the scenario was ruled out in 1964: neutral kaons violate the symmetry CP [2], and CP symmetry breaking may explain the matter-antimatter asymmetry observed in the Universe. Following on from these results measurements on B^0, B_s^0 and $B^{\pm}$ mesons have been performed, showing that these also violate CP [3] [4] [5] [6]. The C, P and T operators can be combined to obtain the CPT operator:

$$CPT|\Psi(r,t)\rangle = e^{+i\phi_{CPT}}|\Psi^*(-r,-t)\rangle, \tag{1.6}$$

$$CPT|\Psi^*(r,t)\rangle = e^{-i\phi_{CPT}}|\Psi^*(-r,-t)\rangle. \tag{1.7}$$

The arbitrary phases $\phi_j, (j = C, P, CP, CPT)$ are chosen in such a way that the eigenvalues of the various C, P, T operators and their combinations are either ± 1. Nowadays, CPT symmetry is considered a fundamental symmetry of Nature due to the so called CPT theorem, which states that that any Lorentz invariant local quantum field theory, such as the standard model (SM), must be symmetric under CPT transformations. As a consequence of the CPT theorem, due to CP violation, the T symmetry has to be broken.

Tests of T non invariance have been performed by the *BABAR* Collaboration leading to the observation of T non invariance with a significance of 14σ in the interference between mixing and decay of processes involving B^0 mesons [7], and today there is a significant effort focussed on experimental and theoretical ways to find some sign of CPT violation.

1.2 Quantum numbers in the standard model

All elementary particles, being quantum objects, are characterised by their quantum numbers. The first quantum number to identify elementary particles is their spin: half-integer for fermions (quarks and leptons) and integer for bosons (8 gluons related to the strong interaction, $W^{\pm}$ and Z^0 related to the weak interaction, the photon γ related to the electromagnetic interaction, and the Higgs boson). The *baryon number* is a quantum number defined for hadrons (both mesons and baryons) as $B = 1/3(n_q - n_{\bar{q}})$ where n_q and $n_{\bar{q}}$ is the number of quarks and antiquarks, and by definition each quark carries a baryon number $B = 1/3$. Also leptons carry a similar quantum number that is called *lepton number* and that by definition is $+1$ for leptons and -1 for antileptons. A quantum number called *isospin* and the third component of which is indicated by the symbol I_3 is also defined for quarks, with values equal to $1/2$ for the *up* quark and $-1/2$ for *down* quark. In addition to baryon and lepton numbers, quarks and leptons carry other quantum numbers that define their properties. Electric charge is defined as the sum of the contribution of the weak isospin, indicated by T_3 and the hypercharge Y for which quarks and leptons assume values according to Table 1.1.

1.2.1 Flavour numbers

Additional quantum numbers defined for both quarks and leptons are the flavour numbers which refer to the type of particle. Charged and neutral leptons can have different flavours: electron (e), muon (μ), and tau (τ), electron neutrino (ν_e), muon neutrino (ν_μ), and tau neutrino (ν_τ). In the quark sector the *up* (u) and *down* (d) quarks are considered unflavoured and flavour is defined for the remaining four quarks. Strangeness, related to

Table 1.1: The weak isospin (T_3), hypercharge (Y), and electric charge (Q) for fermions.

	T_3	Y	Q
q_u	$+1/2$	$+1/6$	$+2/3$
q_d	$-1/2$	$+1/6$	$-1/3$
l	$-1/2$	$-1/2$	-1
ν_l	$+1/2$	$-1/2$	0

the number of strange quarks (s) contained in a hadron, and is defined as $S = -(n_s - n_{\bar{s}})$ and it is equal to -1 for the strange quark. Charm, related to number of charm quarks (c) contained in a hadron, is defined as $C = (n_c - n_{\bar{c}})$ and it is equal to $+1$ for the charm quark. The bottomness, related to number of bottom quarks (b), of a hadron is defined as $B = -(n_b - n_{\bar{b}})$ and it is equal to -1 for the bottom quark. It is possible to define a topness for the top quark (t) as $T = (n_t - n_{\bar{t}})$ and it is equal to $+1$ for the top quark, however one should notice that due to the high value of the mass of the top quark, top quarks do not hadronize to form bound states before they decay.

1.2.2 A general picture of the standard model

A graphical representation for the standard model is shown in Fig. (1.1). Quarks and leptons are grouped in three different generations. Quarks are subjected to all the fundamental forces and in particular to the strong interaction, allowing them to form strongly bound states (mesons are made up of a quark-antiquark pair and baryons are made up of three quarks or three antiquarks), charged leptons interact with the weak bosons and with the photon, neutral leptons only interact with the weak bosons, and all particles apart from gluons and the photon interact with the Higgs boson (including the Higgs boson itself via self interaction).

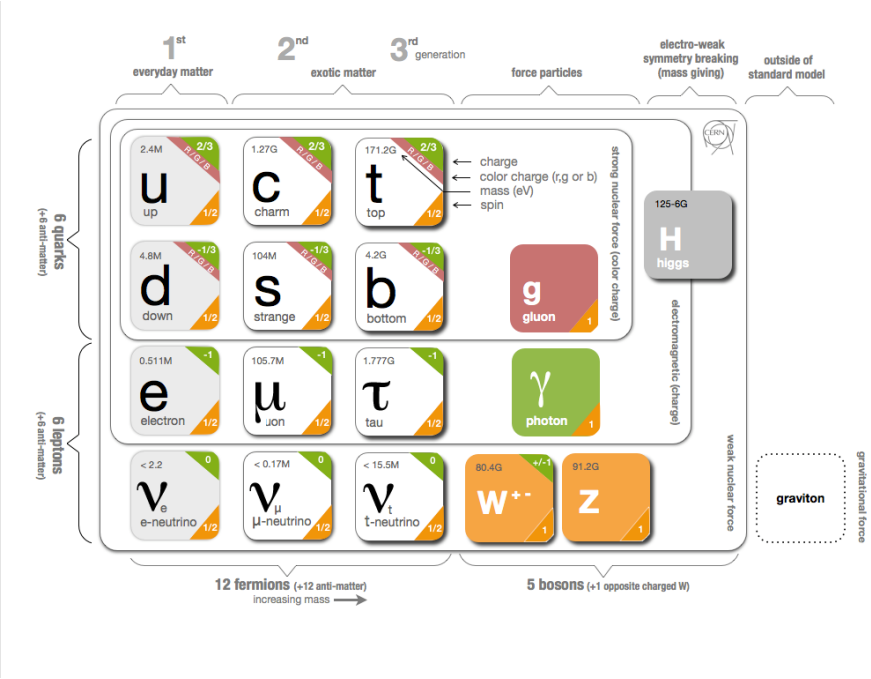

Figure 1.1: Infografic of the standard model [8].

1.3 Neutral meson mixing

Some neutral meson systems, the K^0 ($d\bar{s}$), D^0 ($c\bar{u}$), and $B_{d,s}$ ($d\bar{b}$, $s\bar{b}$), do exhibit a very peculiar behaviour that is referred to as mixing of states or mixing between particle and antiparticle, generally indicated by $P^0 \rightleftarrows \overline{P}^0$ ($P = K$, D, $B_{d,s}$). Mixing between particle and antiparticle is due to the fact that the mass eigenstates are eigenstates of the full Hamiltonian (with all strong, electroweak and electromagnetic components) while flavour eigenstates are eigenstates of the strong interaction (which preserves flavour). Since flavour changing neutral currents (FCNC's) through the emission of a Z^0 boson are forbidden at tree level in the standard model, meson mixing proceeds through so-called *box diagrams* in which the two quarks exchange two W bosons. If one defines $F = S$, C, B as the quantum number of flavour discussed previously, box diagrams allow a $|\Delta F| = 2$ transition as depicted in Fig. (1.2) and in Fig. (1.3), where t- and *s-channel* box diagrams for $D^0 \rightleftarrows \overline{D}^0$ mixing are shown respectively. The Lagrangian for the couplings between quarks

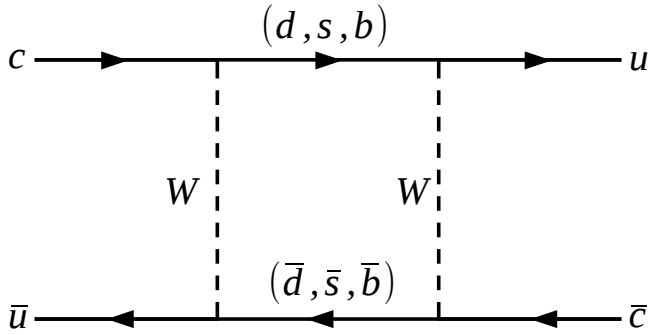

Figure 1.2: Example of a *t-channel* box diagram for $D^0 \rightleftarrows \overline{D}^0$ mixing.

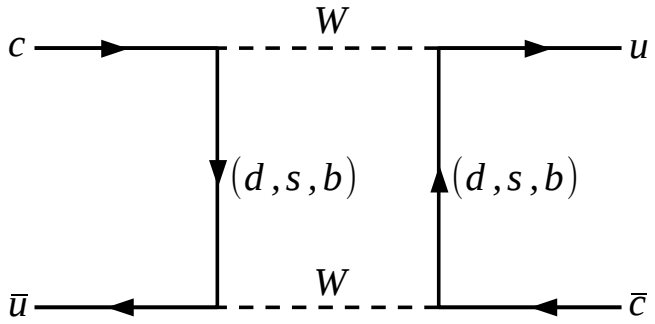

Figure 1.3: Example of an *s-channel* box diagram for $D^0 \rightleftarrows \overline{D}^0$ mixing.

and W bosons can be written as:

$$\mathcal{L}_W = \frac{g_\omega}{\sqrt{2}} \sum_{j,k=1,2,3} [V_{jk} \bar{u}_{jL} \gamma^\mu d_{kL} W_\mu^+ + V_{jk}^* \bar{d}_{kL} \gamma^\mu u_{jL} W_\mu^-], \tag{1.8}$$

where $u_{1,2,3} = u, c, t$ and $d_{1,2,3} = d, s, b$, the W boson only couples to the left-handed components of the quark fields (indicated by the subscript L),

g_ω is the weak coupling constant and V_{jk} denotes elements of the CKM matrix that will be described in Sec. 2.2. It is clear, due to the properties of the CP operator, that in order to have a transition that violates the CP symmetry the CKM matrix cannot be real, consequently some of the elements V_{jk} involved in the transition have to be complex. This represents the first main requirement for CP violation to be manifest: the couplings (related in this case to the CKM matrix elements) must be complex. The mathematical formalism to define mixing is common to all the neutral meson systems discussed above, and the effective Hamiltonian describing neutral meson mixing is given by

$$\mathcal{H}_{eff} \;=\; \mathbf{M} - \frac{i\mathbf{\Gamma}}{2} = \begin{pmatrix} M_{11} & M_{12} \\ M_{21} & M_{22} \end{pmatrix} - \frac{i}{2}\begin{pmatrix} \Gamma_{11} & \Gamma_{12} \\ \Gamma_{21} & \Gamma_{22} \end{pmatrix}. \tag{1.9}$$

Consequently the phenomenon can be described by

$$\begin{pmatrix} |P_1\rangle \\ |P_2\rangle \end{pmatrix} = \mathcal{H}_{eff} \begin{pmatrix} |P^0\rangle \\ |\overline{P}^0\rangle \end{pmatrix}, \tag{1.10}$$

where $|P^0\rangle$ and $|\overline{P}^0\rangle$ are flavour eigenstates of neutral B, D, or K mesons. The mass eigenstates $|P_{1,2}\rangle$ are therefore admixtures of the flavour eigenstates. The matrix elements in Eq. (1.10) must satisfy $M_{11} = M_{22}$ and $\Gamma_{11} = \Gamma_{22}$ in order to be consistent with CPT symmetry conservation. A further constraint can be obtained in the limit of CP or T invariance, where $\Gamma_{12}/M_{12} = \Gamma_{21}/M_{21}$ must be real. The mass eigenstates may be written as an admixture of the strong eigenstates in the following way

$$|P_{1,2}\rangle = p|P^0\rangle \pm q|\overline{P}^0\rangle, \tag{1.11}$$

where $q^2 + p^2 = 1$ to normalize the wave function, and

$$\frac{q}{p} = \sqrt{\frac{M_{12}^* - i\Gamma_{12}^*/2}{M_{12} - i\Gamma_{12}/2}}. \tag{1.12}$$

The magnitude of q/p is one in the SM when CP is conserved in mixing. If one considers the mass eigenstates under the CP operator, it follows that $|P_1\rangle$ is CP even, and $|P_2\rangle$ is CP odd. The mass and width differences ΔM

and $\Delta\Gamma$ between the mass eigenstates are given by

$$\Delta M = M_2 - M_1, \tag{1.13}$$

$$\Delta\Gamma = \Gamma_1 - \Gamma_2, \tag{1.14}$$

where $M_{1,2}$ and $\Gamma_{1,2}$ represent the mass and width of $|P_{1,2}\rangle$ and neutral mesons oscillate from a particle to anti-particle state with the characteristic mixing frequency ΔM. In the literature charm mixing is often described in terms of the two parameters x and y defined as

$$x = \frac{\Delta M}{\Gamma}, \tag{1.15}$$

$$y = \frac{\Delta\Gamma}{2\Gamma}. \tag{1.16}$$

The current world average for the values of x, y, $\left|\frac{q}{p}\right|$ and $arg\left(\frac{q}{p}\right)$ obtained by the HFAG Collaboration are [9] [10]

$$x(\%) = 0.39^{+0.16}_{-0.17}, \tag{1.17}$$

$$y(\%) = 0.67^{+0.07}_{-0.08}, \tag{1.18}$$

$$\left|\frac{q}{p}\right| = 0.91^{+0.11}_{-0.09}, \tag{1.19}$$

$$arg\left(\frac{q}{p}\right)(^\circ) = -10.8^{+10.5}_{-12.3}, \tag{1.20}$$

when CP violation is allowed in the fit, and

$$x(\%) = 0.53^{+0.16}_{-0.17}, \tag{1.21}$$

$$y(\%) = 0.67 \pm 0.09, \tag{1.22}$$

when the CP conserving hypothesis is considered in the fit. The results discussed above for x and y are shown in Fig. (1.4) and Fig. (1.5), and in Fig. (1.6) where the *one-to-five* σ allowed regions are depicted [9]; the first two show the combination of results for which CP violation is allowed in the fit, the third considers the CP conserving hypothesis in the fit.
From both Fig. (1.4) and Fig. (1.6) one can see that the no mixing hypothesis is excluded at more than 5σ proving that charm mixing is a well established phenomenon.

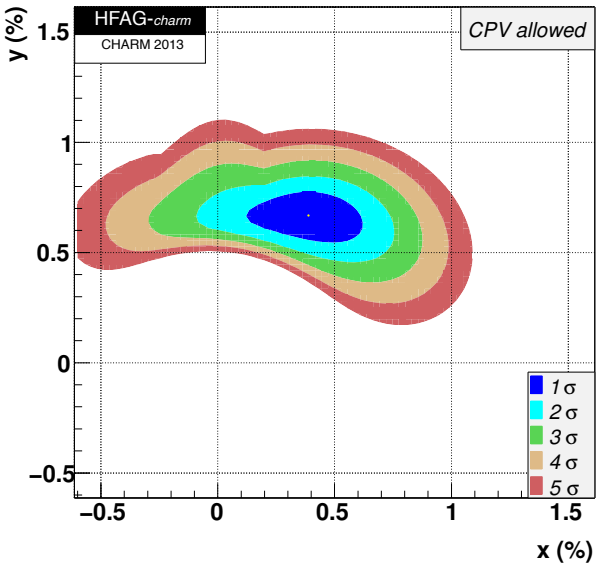

Figure 1.4: *One-to-five* σ allowed regions for x with respect to y allowing for CP violation in the fit [9] [10].

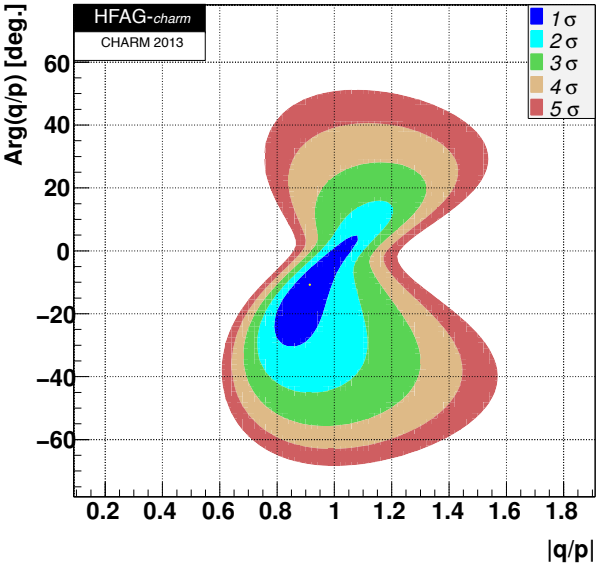

Figure 1.5: *One-to-five* σ allowed regions for $\left|\frac{q}{p}\right|$ with respect to $arg\frac{q}{p}$ allowing for CP violation in the fit [9] [10].

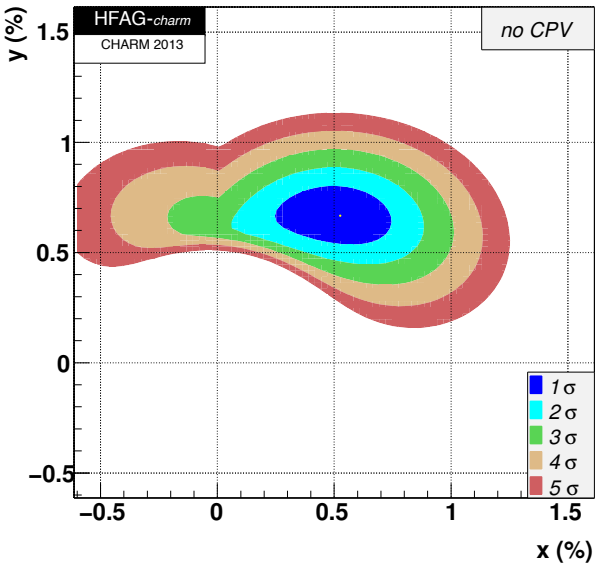

Figure 1.6: *One-to-five* σ allowed regions for x with respect to y assuming the CP conserving hypothesis in the fit [9] [10].

1.4 CP violation

As discussed in Sec. 1 the mechanism that may allow matter to dominate over antimatter in the evolution of the Universe is the violation of the CP symmetry. The breaking of the CP symmetry in quarks can be generated in three different ways which are referred to as *indirect*, *direct*, and CP violation in the interference between mixing and decay (or $interference\ CP$ violation). The observation of CP violation in any of these three possible ways in a particular process (decay) is equivalent to observing a different behaviour of matter and antimatter under that process. The strong interaction does not violate CP[2], because it appears that CP violation only occurs in flavour changing processes, and the strong interaction is flavour blind. Weak interactions however, in flavour changing processes, may violate C, P, and their combination CP. This means that when referring to CP violation, one

[2]This is known as the strong CP problem due to the fact that the QCD Lagrangian which describes the strong interaction contains terms that may violate the CP symmetry but this is not observed experimentally.

normally requires CP violation in weak decays.

1.4.1 Types of CP violation

Indirect CP violation

As previously mentioned, CP violation was observed for the first time in the neutral K system. In particular Cronin, Fitch, Christensen and Turlay [2] were studying K_L^0 mesons that have a CP eigenvalue equal to -1 and decay predominantly to three pions (CP eigenstate equal to -1). As a consequence of the possibility of mixing of states, neutral mesons oscillate back and forth between particle and antiparticle, and due to quantum mechanics the two states coexist for a certain time. When the particle decays the wave function collapses, one of the two states has to be filtered by the decay, providing it with a well defined flavour. However, the probability of the oscillation particle to antiparticle may be not the same as the one for antiparticle to particle, and when this happens CP symmetry is broken in mixing. Considering the parameters p and q, the necessary condition to have CP violation in mixing is $p/q \neq 1$.

Direct CP violation

A particle with a given CP eigenvalue should decay (ignoring mixing related effects) into a final state with the same CP eigenvalue, to preserve the CP symmetry. The same is true for the antiparticle, which should decay to the conjugated final state with opposite CP eigenvalue to that of the particle in order to preserve CP. Let's call P the particle, $\overline{P}$ its antiparticle, and f_{CP} the flavour specific CP eigenstate that P decays to, similarly $\overline{f}_{CP}$ will denote the flavour specific CP eigenstate that $\overline{P}$ decays to, $|A_f|$ the module of the decay amplitude for $P \to f_{CP}$ and $|\overline{A_f}|$ the module of the decay amplitude for $\overline{P} \to \overline{f}_{CP}$. If $f_{CP} = \overline{f}_{CP}$, and $|A_f| \neq |\overline{A_f}|$ then CP is broken in the decay. This process is a small effect when compared to indirect CP violation in the kaon system, and is referred to as *direct* CP violation. I will show in the next chapter that in order for direct CP violation to be manifest two different decay amplitudes with different strong and weak phases are needed

(see Sec. 2.3.1).

CP violation in the interference between mixing and decay

In general, when different decay amplitudes contribute to a particular decay channel, and if there is a weak phase mismatch between them, CP violation is manifest. Here it is useful to define a parameter, λ_f, from which one can see that only when this parameter is equal to one the CP symmetry is preserved:

$$\lambda_f = \frac{q}{p}\frac{\overline{A}}{A} = \left|\frac{q}{p}\right| e^{i\phi_{MIX}} \left|\frac{\overline{A}}{A}\right| e^{i\phi_{CP}} \tag{1.23}$$

where q and p are the parameters defining the mixing seen previously and A ($\overline{A}$) is the amplitude for the P ($\overline{P}$) decay to a final state f. If $q/p \neq 1$ CP is violated in mixing (indirect CPV), and $|A|^2 \neq |\overline{A}|^2$ implies direct CP violation (in the decay). Through the study of λ_f one is able to probe the combination of CP violation due to mixing and due to decay, and this form of CP violation is referred to as CP violation in the interference between mixing and decay. In the case of the decay $D^0 \to \pi^+\pi^-$ there are two possible ways the D^0 might decay to the final state, as depicted in Fig. (1.7). The first is the direct decay $D^0 \to \pi^+\pi^-$ with its own decay amplitudes and topology that will be discussed in detail in the next chapter, the second possibility is the process $D^0 \to \overline{D}^0 \to \pi^+\pi^-$. The interference between the mixed decay amplitude and the direct decay amplitude might violate CP through a complex phase, equal to $\phi_{MIX} - 2\beta_c$, where β_c is one angle of the charm unitarity triangle (discussed in the next chapter). This type of CP violation has been observed in the neutral B meson system [3], but has not yet been observed in the D meson system. A method to perform studies of CP violation and mixing in neutral D mesons and how to relate this study to searches for physics beyond the standard model (BSM), otherwise referred to as new physics (NP), is the main focus of this thesis and is based on work published in [11].

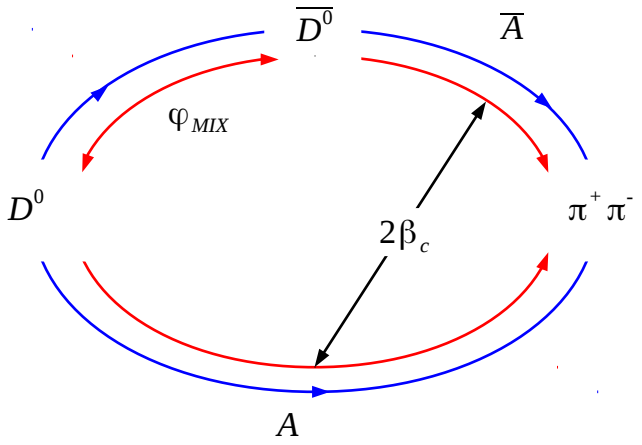

Figure 1.7: Diagram showing how the phase $2\beta_c$ is introduced in $D^0 \to \pi^+\pi^-$ decays. In the bottom path the D^0 meson decays directly to the final state $\pi^+\pi^-$, in the top path the D^0 meson undergoes mixing first, then the $\overline{D}^0$ meson decays to the final state $\pi^+\pi^-$. The phase mismatch ($2\beta_c$) between the D^0 and $\overline{D}^0$ decays to $\pi^+\pi^-$ violates CP.

Chapter 2

CP violation in charm decays

2.1 Introduction

The study of time-dependent CP violation in charm mesons may provide a very powerful tool to test the Cabibbo-Kobayashi-Maskawa (CKM) mechanism as the origin of CP violation [12] [13] and in general it can be used as a test of the standard model (SM) itself. In general one can measure $\phi_{MIX} - 2\beta_{c,eff}$ using $D^0 \to \pi^+\pi^-$ decays. In the SM β_c is small, and if one can understand the effect of phase shifts from penguins one can measure ϕ_{MIX} in this channel. If one assumes ϕ_{MIX} is measured elsewhere then one can attempt to constrain β_c, up to the theoretical uncertainty imposed by hadronic corrections from penguin diagrams. This can be done through the measurement (or constraint) of the angle $\beta_{c,eff}$. The angle $\beta_{c,eff}$ is related to the angle β_c in the charm unitarity triangle which will be presented in Sec. 2.2.2 and the relationship between $\beta_{c,eff}$ and β_c will be summarised in Sec. 2.5.3. One can constrain $\beta_{c,eff}$ by combining the measured CP asymmetries in the decays $D^0 \to K^+K^-$ and $D^0 \to \pi^+\pi^-$ [11]. In e^+e^- collisions at the charm threshold (energy at which the c-$\bar{c}$ resonance $\Psi(3770)$ is produced), pairs of D^0 mesons are produced in a quantum entangled state, as discussed later, and the measurement of any time-dependent asymmetry is related to the measurement of the position of the two decay vertices of the D^0 and $\overline{D}^0$ mesons in the event. In the remainder of this chapter the phenomenology of CP violation in charm decays is presented.

2.2 The CKM Matrix and the unitarity triangle(s)

In the SM, CP symmetry breaking is generated by a complex phase appearing in the Cabibbo-Kobayashi-Maskawa (CKM) matrix [12] [13]. The CKM matrix is a unitary 3×3 matrix which provides a description of quark mixing in terms of the coupling strengths for *up*- to *down-type* quark transitions, and it may be written as

$$V_{CKM} = \begin{pmatrix} V_{ud} & V_{us} & V_{ub} \\ V_{cd} & V_{cs} & V_{cb} \\ V_{td} & V_{ts} & V_{tb} \end{pmatrix}. \tag{2.1}$$

Within this framework the probability to observe a transition between a quark q to a quark q' is proportional to $|V_{qq'}|^2$. A 3×3 matrix is parametrised by 18 parameters. Due to unitarity the number of independent parameters is reduced to 9: three angles and six complex phases. Here, if one transforms the quark fields present in Eq. (1.8) as $d_j \to e^{i\phi_j^d} d_j$ and $u_k \to e^{i\phi_k^u} u_k$ then the V_{jk} elements transform to $V_{jk} e^{i(\phi_j^d - \phi_k^u)}$. With this last operation one can remove five of the six phases, because they are unphysical, and this leaves only one phase, so finally the CKM matrix can be parametrised by 4 physical quantities, three (Euler) rotation angles and a complex phase. The three Euler rotations matrix are written as

$$U_{12} = \begin{pmatrix} c_{12} & s_{12} & 0 \\ -s_{12} & c_{12} & 0 \\ 0 & 0 & 1 \end{pmatrix}, \tag{2.2}$$

$$U_{13} = \begin{pmatrix} c_{13} & 0 & s_{13} \\ 0 & 1 & 0 \\ -s_{13} & 0 & c_{13} \end{pmatrix}, \tag{2.3}$$

$$U_{23} = \begin{pmatrix} 1 & 0 & 0 \\ 0 & c_{23} & s_{23} \\ 0 & -s_{23} & c_{23} \end{pmatrix}, \tag{2.4}$$

and the phase matrix is

$$U_\delta = \begin{pmatrix} 1 & 0 & 0 \\ 0 & 1 & 0 \\ 0 & 0 & e^{-i\delta_{13}} \end{pmatrix}. \tag{2.5}$$

The CKM matrix can then be written as a combination of these matrices as

$$V_{CKM} = U_{23} U_\delta^\dagger U_{13} U_\delta U_{12}, \tag{2.6}$$

obtaining the standard PDG parametrisation $V = V_{CKM}$ [14]

$$V = \begin{pmatrix} c_{12}c_{13} & s_{12}c_{13} & s_{13}e^{-i\delta_{13}} \\ -s_{12}c_{23} - c_{12}s_{23}s_{13}e^{i\delta_{13}} & c_{12}c_{23} - s_{12}s_{23}s_{13}e^{i\delta_{13}} & s_{23}c_{13} \\ s_{12}s_{23} - c_{12}c_{23}s_{13}e^{i\delta_{13}} & -c_{12}s_{23} - s_{12}c_{23}s_{13}e^{i\delta_{13}} & c_{23}c_{13} \end{pmatrix}, \tag{2.7}$$

where $c_{ij} = \cos\theta_{ij}$, $s_{ij} = \sin\theta_{ij}$ and δ_{13} is the complex term responsible for CP violation. The phenomenology of CP violation is discussed in a convention dependent way, however due to re-phasing invariance, the underlying physical observables computed are independent of convention.

2.2.1 Unitarity and Parametrisations of the CKM Matrix

Different parametrisations of the CKM matrix are available; the Wolfenstein parametrisation [15] is one of the most used parametrisations. This parametrisation is an expansion in terms of $\lambda = \sin\theta_c, A, \rho, \eta$ (θ_c is the Cabibbo angle) based on the magnitude of the elements in terms of λ and is shown in Eq. (2.8)

$$V_{CKM} = \begin{pmatrix} 1 - \lambda^2/2 & \lambda & A\lambda^3(\rho - i\eta) \\ -\lambda & 1 - \lambda^2/2 & A\lambda^2 \\ A\lambda^3(1 - \rho - i\eta) & -A\lambda^2 & 1 \end{pmatrix} + \\ + \mathcal{O}(\lambda^4). \tag{2.8}$$

A variant of this parametrisation expanded up to and including terms $\mathcal{O}(\lambda^5)$ is shown in Eq. (2.9) [11]

$$V_{CKM} = \begin{pmatrix} 1-\frac{\lambda^2}{2}-\frac{\lambda^4}{8} & \lambda & A^3\lambda^3\overline{\xi}(1+\frac{\lambda^2}{2}) \\ -\lambda+\frac{A^2\lambda^5}{2}(1+2\overline{\zeta}) & 1-\frac{\lambda^2}{2}-\frac{\lambda^4}{8}(1+4A^2) & A\lambda^2 \\ A\lambda^3(1+\overline{\zeta}) & -A\lambda^2+\frac{A\lambda^4}{2}(1+2\overline{\zeta}) & 1-A^2\frac{\lambda^4}{2} \end{pmatrix} + \\ +\mathcal{O}(\lambda^6), \quad (2.9)$$

where in Eq. (2.9)

$$\overline{\xi} = \overline{\rho} - i\overline{\eta}, \quad (2.10)$$

$$\overline{\zeta} = -\overline{\rho} - i\overline{\eta}, \quad (2.11)$$

$$\overline{\rho} = \rho[1-\lambda^2/2+\mathcal{O}(\lambda^4)], \quad (2.12)$$

$$\overline{\eta} = \eta[1-\lambda^2/2+\mathcal{O}(\lambda^4)]. \quad (2.13)$$

For this study we will use this latter parametrisation of the CKM matrix. The choice to consider the CKM matrix with an expansion up to $(\lambda^5)+\mathcal{O}(\lambda^6)$, is due to the fact that while the expansion up to λ^3, was sufficient for the B factories era, now it becomes necessary to consider additional terms as we move into the era of LHCb and of the Super Flavour Factories (SFF's), not only from a completeness point of view but mainly because CP violation in charm is expected to be very small in the SM ($< 1\%$) and at $\mathcal{O}(\lambda^3)$ no CP violation would be predicted. In fact it should be mentioned that the LHCb collaboration has reported a large difference in direct CP asymmetries in the decays $D^0 \to K^+K^-$ and $D^0 \to \pi^+\pi^-$ that was 3.5σ from the CP conserving hypothesis [17], however the disagreement with the CP conserving hypothesis decreased to 1.9 σ when adding additional data [18]. The result was also disfavoured by an alternative analysis of data collected at the LHCb experiment that used D^0 tagged mesons coming from semileptonic decays of b-hadrons [19] (for the method used see Sec. 2.3). The values of the parameters used in the CKM matrix are shown in Tab. (2.1)[1]. The convention to write the CKM matrix in terms of $\overline{\rho}$ and $\overline{\eta}$ was adopted because unitarity

[1]UTFit and CKM Fitter groups results are shown along with a naive arithmetic average of the two that we used in our study. We decided to use the naive average in this study to simply find a common point between the different approach of the two groups.

Table 2.1: Constraints on the Wolfenstein parameters A, λ, ρ, η, $\overline{\rho}$, and $\overline{\eta}$ obtained by the UTFit and CKM fitter groups.

Parameter	UTFit	CKM Fitter	Naive Mean Used
λ	0.22545 ± 0.00065	0.22543 ± 0.00077	0.22544 ± 0.00071
A	0.8095 ± 0.0095	$0.812^{+0.013}_{-0.027}$	0.811 ± 0.015
ρ	0.135 ± 0.021	–	–
η	0.367 ± 0.013	–	–
$\overline{\rho}$	0.132 ± 0.020	0.144 ± 0.025	0.138 ± 0.022
$\overline{\eta}$	0.358 ± 0.012	$0.342^{+0.016}_{-0.015}$	0.350 ± 0.014

of the CKM matrix gives rise to six unitarity triangles in the complex plane and $\overline{\rho}$ and $\overline{\eta}$ represents the coordinates of the apex of the bd unitarity triangle given in Eq. (2.18) below. Since unitarity triangles are mathematically exact, it is very important to measure their angles and sides to verify unitarity. This allows one to check if the CKM mechanism is the ultimate answer to the CP violation problem in the quark sector or if some new physics (NP) effects are required to describe Nature. In this sense, a recent article [20] has pointed out that the measured value for $\sin 2\beta$ in the beauty-unitarity triangle differs by 3.2 standard deviations from the predicted value. In the paper the authors claim that this discrepancy could be interpreted as an indication that CKM mechanism is breaking down. The six unitarity triangle relationships of the CKM matrix may be written as

$$V_{ud}^* V_{us} + V_{cd}^* V_{cs} + V_{td}^* V_{ts} = 0, \tag{2.14}$$

$$V_{us}^* V_{ub} + V_{cs}^* V_{cb} + V_{ts}^* V_{tb} = 0, \tag{2.15}$$

$$V_{ud}^* V_{td} + V_{us}^* V_{ts} + V_{ub}^* V_{tb} = 0, \tag{2.16}$$

$$V_{cd}^* V_{td} + V_{cs}^* V_{ts} + V_{cb}^* V_{tb} = 0, \tag{2.17}$$

$$V_{ud}^* V_{ub} + V_{cd}^* V_{cb} + V_{td}^* V_{tb} = 0, \tag{2.18}$$

$$V_{ud}^* V_{cd} + V_{us}^* V_{cs} + V_{ub}^* V_{cb} = 0, \tag{2.19}$$

where Eq. (2.18) is a well known and studied case referred to as the *bd* triangle or unitarity triangle (UT), Eq. (2.19) represents the *cu* triangle that we will call the *charm* unitarity triangle or simply *charm* triangle.

2.2.2 The charm unitarity triangle

In the previous section we have seen that Eq. (2.19) defines the *charm* unitarity triangle. The angles of this triangle are

$$\alpha_c = \arg\left[-V_{ub}^* V_{cb}/V_{us}^* V_{cs}\right], \tag{2.20}$$
$$\beta_c = \arg\left[-V_{ud}^* V_{cd}/V_{us}^* V_{cs}\right], \tag{2.21}$$
$$\gamma_c = \arg\left[-V_{ub}^* V_{cb}/V_{ud}^* V_{cd}\right]. \tag{2.22}$$

Using the averages of CKM Fitter and UTFit values for A, λ, $\overline{\rho}$ and $\overline{\eta}$ and their errors given in Tab. 2.1, we predict that, to order λ^5

$$\alpha_c = (111.5 \pm 4.2)^\circ, \tag{2.23}$$
$$\beta_c = (0.0350 \pm 0.0001)^\circ, \tag{2.24}$$
$$\gamma_c = (68.4 \pm 0.1)^\circ. \tag{2.25}$$

These predictions for the angles of the charm triangle should be tested experimentally, either directly (through time-dependent CP asymmetries) or indirectly (through measurements of the sides of the triangle). On comparing Eq. (2.21) with Eq. (2.9), one can see that $V_{cd} = |V_{cd}|e^{i(\beta_c - \pi)}$ [2]. The *charm* triangle is shown in Fig. 2.1, where the sides are not to scale. If one takes the triangle represented at the top in Fig. 2.1 and divides through by $V_{us}^* V_{cs}$ the triangle shown at the bottom is obtained, in which the baseline is normalised to one. A measurement of, or a constraint on, β_c is possible through the study of time-dependent CP asymmetries in D^0 decays by combining the measured asymmetries in $D^0 \to K^+K^-$ and $D^0 \to \pi^+\pi^-$ as described in Sec. 2.4.

[2] The following phenomenological analysis is based on this parametrisation, however the phase differences are re-phasing invariant.

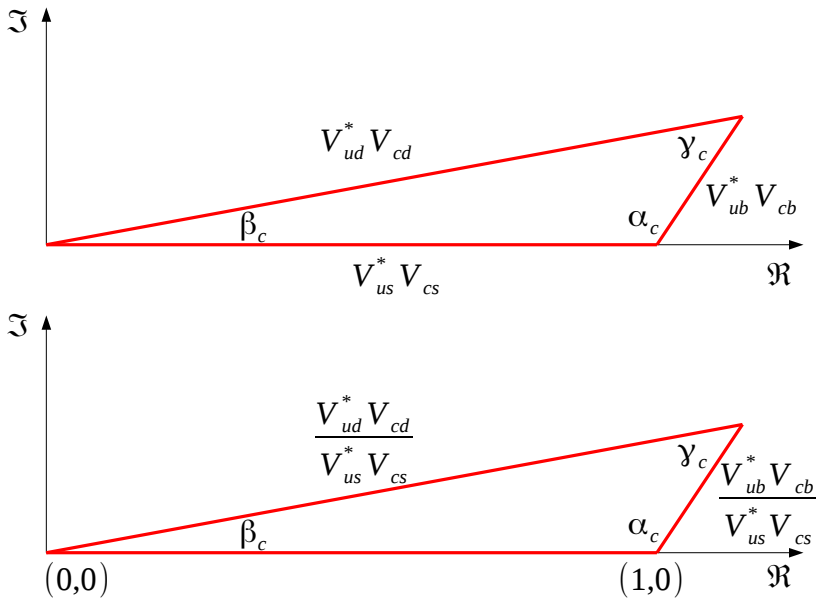

Figure 2.1: The *charm* triangle before (top) and after (bottom) baseline normalization represented in the complex plane.

2.3 Time integrated approach: A_{CP} and ΔA_{CP}

As discussed in the introduction, there are various ways to test CP violation, and one of these is the time integrated approach, in which one compares the rate of a particle decay to some CP eigenstate f_{CP} with that of the antiparticle to the same eigenstate. In this context one defines the asymmetry as

$$A_{CP}(f_{CP}) = \frac{|\overline{A}|^2 - |A|^2}{|\overline{A}|^2 + |A|^2} \tag{2.26}$$

where $\overline{A}$ and A refer to the decay amplitudes of $\overline{D}^0 \to f_{CP}$ and $D^0 \to f_{CP}$, respectively. The asymmetry evaluated using Eq. (2.26) consists of two components, direct and indirect as follows [16]

$$A_{CP}(f_{CP}) = a^{dir}_{CP}(f_{CP}) + \frac{\langle\tau\rangle}{t} a^{ind}_{CP}(f_{CP}) \tag{2.27}$$

where τ is the lifetime of the D^0 meson and t is the average decay time. Note that the second term in Eq. (2.27) is due to the acceptance of the trigger.
From an experimental point of view the situation is complicated by the presence of possible contributions to A_{CP} coming from detector related issues; this is the case for hadron machines or for e^+e^- colliders running at a centre-of-mass energy equivalent to that of the $\Upsilon(4S)$ where a D^0 ($\overline{D}^0$) meson is produced in the decay $D^{*+} \to D^0\pi^+$ ($D^{*-} \to \overline{D}^0\pi^-$) (let's call these two situations case a) and case b), respectively), where in general the asymmetry is evaluated "counting" the number of D^0 and $\overline{D}^0$ decaying to f_{CP}. In case a) one has:

$$A_{CP}(f_{CP}) = A_{raw}(f_{CP}) - A_D(f_{CP}) - A_D(\pi^\pm_s) - A_P(D^{*\pm}) \tag{2.28}$$

where $A_{raw}(f_{CP})$ is the observed asymmetry, $A_D(f_{CP})$ is the asymmetry coming from the selection of D mesons decaying to f_{CP}, $A_D(\pi^\pm_S)$ is the asymmetry coming from the selection of $\pi^{\pm 3}_s$ and $A_P(D^{*\pm})$ is the production asymmetry for $D^{*\pm}$. In case b) the situation is similar and one would expect:

$$A_{CP}(f_{CP}) = A_{raw}(f_{CP}) - A_{FB} - A_\epsilon(f_{CP}) \tag{2.29}$$

[3]The subscript s indicates that the pion used to tag the D^0 has a low momentum (soft pion) if compared to a pion coming from a decay of the D^0 meson. A more detailed discussion about flavour tagging can be found in Sec. 2.6.

where A_{FB} is the *forward-backward* asymmetry for $e^+e^- \to c\bar{c}$ processes and $A_\epsilon(f_{CP})$ is the particle detection asymmetry which depends on the final state. Due to the various asymmetry contributions to A_{CP}, a time integrated measurement may be difficult. However, examining Eq. (2.28) one can see that the last two asymmetry contributions are the same for different final states (K^+K^-, $\pi^+\pi^-$), then it is possible to combine the observed asymmetries in two different decay channels to cancel them. One can consider the asymmetry between two decay channels, ΔA_{CP}. The detection asymmetry $A_D(\pi_S^\pm)$ and production asymmetry cancel in this difference. For the decays $D^0 \to K^+K^-$ and $D^0 \to \pi^+\pi^-$ one obtains

$$\begin{aligned} \Delta A_{raw} = A_{CP}(K^+K^-) + A_D(K^+K^-) + A_D(\pi_s^\pm) + A_P(D^{*\pm}) \quad - \\ A_{CP}(\pi^+\pi^-) + A_D(\pi^+\pi^-) + A_D(\pi_s^\pm) + A_P(D^{*\pm}) \quad = \\ A_{CP}(K^+K^-) - A_{CP}(\pi^+\pi^-) + \Delta A_{D_{\pi^+\pi^-}^{K^+K^-}}, \end{aligned} \tag{2.30}$$

where $\Delta A_{D_{\pi^+\pi^-}^{K^+K^-}} = A_D(K^+K^-) - A_D(\pi^+\pi^-)$. However, "*for a two-body decay of a spin-0 particle to a self-conjugate final state there can be no D^0 detection asymmetry, i.e. $A_D(K^+K^-) = A_D(\pi^+\pi^-) = 0$*" [17]. Finally

$$\Delta A_{raw} = A_{CP}(K^+K^-) - A_{CP}(\pi^+\pi^-) = \Delta A_{CP}, \tag{2.31}$$

showing that the extracted value of ΔA_{raw} can be considered as a measurement of CP violation. This measurement has already been performed by many experiments [17] [18] [19] [21] [22], and the combined results are shown in Fig. 2.2 for which $\Delta A_{CP}^{dir} = -0.00329 \pm 0.00121$ and $a_{CP}^{ind} = -0.00010 \pm 0.00162$ [9], showing that data are consistent with the CP conserving hypothesis at 2.1% confidence level (2.0% in more recently presented results during the CHARM 2013 conference [10]). It is clear from Fig. 2.2 that with the current sensitivity it is not possible to provide a conclusive answer to the existence of CP violation in charm decays, but the results can be used to evaluate if it is possible to constrain some quantities such as the strong or the weak phase differences (discussed in the next section).

2.3.1 Interpreting ΔA_{CP}

The theoretical interpretation of ΔA_{CP} is non trivial. This much can be seen from the numerous claims of new physics and standard model compatible

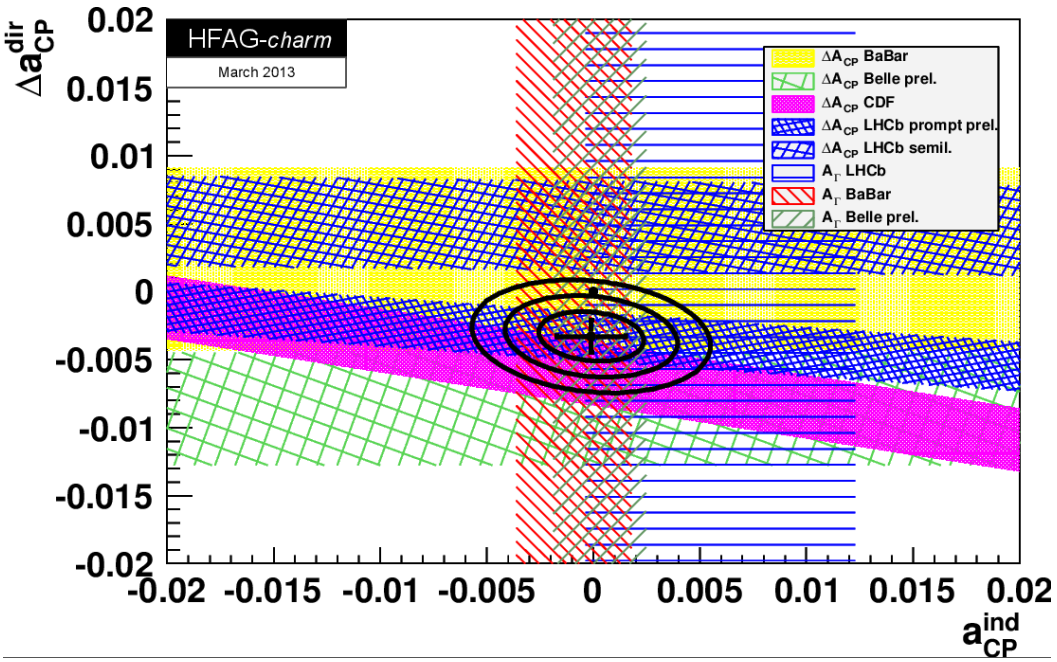

Figure 2.2: HFAG combination for indirect vs. direct CP violation in charm (March 2012). The data are consistent with the CP conserving hypothesis at 2.1% confidence level [9].

results that came about from each update of the measurement from LHCb. The purpose of this section is to explore, using a simple toy model, the basic problem with trying to interpret ΔA_{CP}. The assumptions made here are not supposed to be realistic, rather they are imposed as they are sufficient to allow us to illustrate the understand the underlying physics issues and what we can learn from the $D \to hh$ decays. While a more realistic model could be considered this would add complexity without adding any additional physics insight. When writing Eq. (2.26) only general decay amplitudes have been considered, but an explicit expression for these has been omitted. Here we assume, for the purposes of simplicity and for illustration, that ΔA_{CP} is dominated by one mode, and that that mode has only two interfering

amplitudes (e.g. a tree and a penguin in the context of the SM) with different strong and weak phases that contribute to the decays considered (i.e. $D^0 \to h^+h^-, h = K, \pi$) so that

$$A = A_T e^{i(\phi_T+\delta_T)} + A_N e^{i(\phi_N+\delta_N)} \tag{2.32}$$

where a *new* sub-leading order amplitude A_N with strong and weak phases respectively δ_N and ϕ_N interferes with the leading order *tree* amplitude A_T with strong and weak phases respectively δ_T and ϕ_T. The weak and strong phase differences are $\Delta\delta$ and $\Delta\phi$, and for example Eq. (2.26) can be written as

$$A_{CP} = \frac{2A_N A_T \sin\Delta\phi \sin\Delta\delta}{|A_N|^2 + |A_T|^2 + 2A_N A_T \cos\Delta\phi \cos\Delta\delta}. \tag{2.33}$$

One can also define a useful parameter $r = A_N/A_T$ which defines the ratio between the sub-leading to leading order amplitudes. In the evaluation of ΔA_{CP} two decay channels are considered while Eq. (2.33) contains only one decay. Looking at the CKM matrix element, one can see that a tiny CP asymmetry may arise from the $D^0 \to K^+K^-$ decay channel, in fact just considering the standard parametrisation of the CKM matrix shown in Eq. (2.7) we find:

$$V_{cd}V_{ud}^* = (-s_{12}c_{23} - c_{12}s_{13}s_{23}e^{i\delta_3})c_{12}c_{13} \tag{2.34}$$

and

$$V_{cs}V_{us}^* = (c_{12}c_{23} - s_{12}s_{13}s_{23}e^{i\delta_3})s_{12}c_{13} \tag{2.35}$$

where the Eq. (2.34) refers to the CKM matrix elements involved in the decay $D^0 \to \pi^+\pi^-$ (tree level) and Eq. (2.35) to the CKM matrix elements involved in the decay $D^0 \to K^+K^-$ (tree level). It follows from Eq. (2.34) and Eq. (2.35) that while the real part is the same for both decays except for a flipped sign ($c_{12}c_{13}c_{23}s_{12}$), the imaginary part which is responsible for CP violation is different, and in particular is much larger for $D^0 \to \pi^+\pi^-$ than for $D^0 \to K^+K^-$ (i.e. $c_{12}^2c_{13}s_{13}s_{23} >> s_{12}^2c_{13}s_{13}s_{23}$). From these considerations we assume ΔA_{CP} is dominated by $D^0 \to \pi^+\pi^-$, here it must be re-emphasised that this interpretation neglects the contribution of direct CP

violation in $D^0 \to K^+K^-$, which is generally considered to be the most likely explanation of any larger-than-expected value of this quantity [23]. In other words $D^0 \to \pi^+\pi^-$ measures a phase $\phi_{\pi\pi} = \phi_{MIX} - 2\beta_c$ and $D^0 \to K^+K^-$ measure a phase $\phi_{KK} \simeq \phi_{MIX}$ as shown in Sec. 2.2.2, and the difference between the two phases at tree level is $\phi_{KK} - \phi_{\pi\pi} \simeq \phi_{MIX} - \phi_{MIX} + 2\beta_c = 2\beta_c$. One can consider the level of direct CP violation in terms of r, $\Delta\delta$ and $\Delta\phi$. Figures 2.3 and 2.4 show ΔA_{CP} as a function of $\Delta\delta$ and $\Delta\phi$ for $r = 0.01$ and $r = 0.1$, respectively, under the assumption that the CP symmetry is preserved in $D^0 \to K^+K^-$ [4]. It can be seen that one can infer constraints on (r, $\Delta\delta$) for a given measurement of A_{CP}. As very large penguins or new physics in charm decays is implausible, we can assume a more modest value for r ($r = 0.01$) to be plausible, however the conclusions are independent of the value of r chosen as long as $r > 0$. The current ΔA_{CP} measurement from HFAG of ΔA_{CP} can be translated into the constraint shown in Fig. 2.5.

This shows that a priori, only constraints on combinations of $\Delta\delta$ and $\Delta\phi$ can be made for a given r. In particular a large $\Delta\phi$ cannot be excluded a priori. As discussed in the previous section, when evaluating the difference of the observed phases in $D^0 \to K^+K^-$ and $D^0 \to \pi^+\pi^-$ one would expect to measure $\Delta\phi = 2\beta_c = 0.07^\circ = 0.0012$. Of course when comparing a *real* measurement with an *ideal* one, it has to be taken into account that there are penguin uncertainties that need to be kept under control. One should then consider that this measurement provides insights about $\beta_{c,eff}$, where the *eff*(*ective*) subscript means that there are hadronic uncertainties that

[4] Under U-spin symmetry one would expect to observe the same amount of direct CP violation in $D^0 \to K^+K^-$ and $D^0 \to \pi^+\pi^-$ but with different sign, so this preliminary study just describes the starting point toward a more detailed analysis. There is insufficient data to test this relation at the current time, however it is known that U-spin breaking effects may be large in these modes [24], which also follows directly from the measured branching fractions of these two decays. Furthermore, a-priori it is not valid to assume that the strong phase differences in the KK mode and $\pi\pi$ mode are the same, and it is not possible for theorists to reliably compute these phase differences. Thus while the U-spin relation is interesting, it can not be relied upon until proven and may ultimately turn out to be an inadequate description. This highlights the fact that direct *CP* asymmetries are not clean observables and interpretation of these quantities is difficult (ε' in the kaon system is the classic example of this issue). Time will tell if this U-spin relation is a good approximation to use.

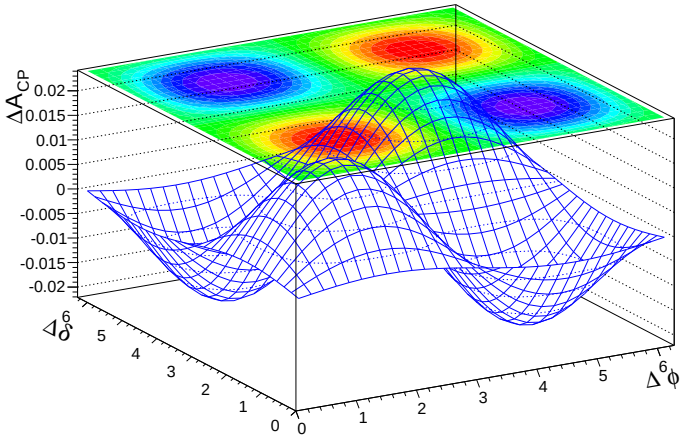

Figure 2.3: The expected value of ΔA_{CP} when $r = 0.01$,and assuming no CP violation in $D^0 \to K^+K^-$.

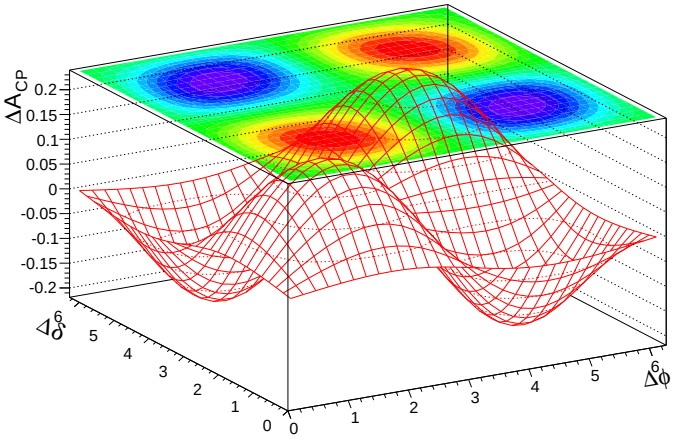

Figure 2.4: The expected value of ΔA_{CP} when $r = 0.1$ and assuming no CP violation in $D^0 \to K^+K^-$.

need to be calculated and that will systematically influence the result. If one ignores penguin contributions and considers the ΔA_{CP} HFAG average, then the results is 3.8σ in disagreement with predictions.

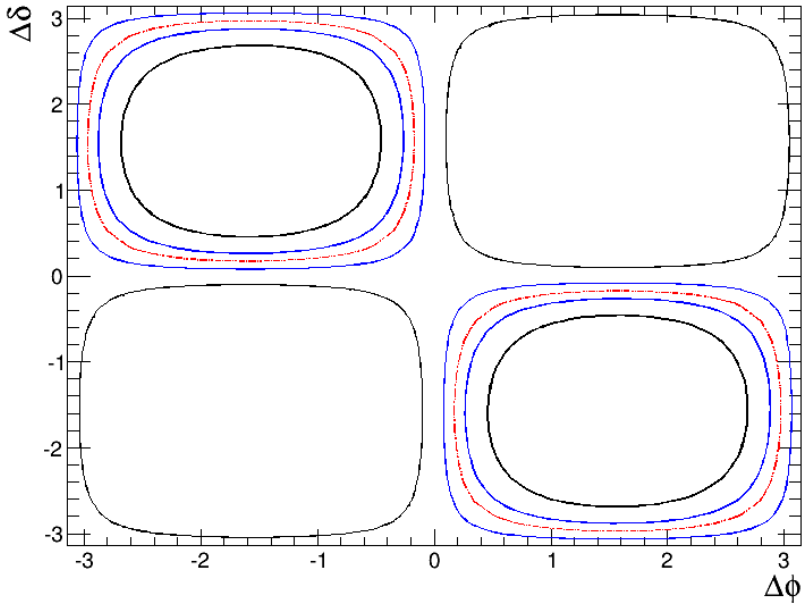

Figure 2.5: One to three standard deviation allowed regions for $\Delta\phi$ and $\Delta\delta$ assuming $\Delta A_{CP} = -0.00329$ (HFAG 2013) and $r = 0.01$. The red contour shows the central value, while the blue and black contours show the 1σ and 3σ contours, respectively.

The results is interesting, however I think that it does not tell us much about CP violation and furthermore about β_c. The problem is that when one tries to make any consideration about the results on the quantity ΔA_{CP}, one needs to make a set of assumptions, due to the fact that there are many parameters involved: $\Delta\phi_{\pi\pi}$ and $\Delta\delta_{\pi\pi}$, $\Delta\phi_{KK}$ and $\Delta\delta_{KK}$, $r_{\pi\pi}$ and r_{KK} (where suffixes $\pi\pi$ and KK refer to decay channel). Using a more realistic model will just complicate matters and not provide additional insight as the problem is underconstrained, i.e. there are six parameters to determine and only one measurement. A better way to study CP violation in charm decays would require a couple of additional ingredients. First of all one ideally wants individual measurements, in which not too many variables are involved if one wants to try to make some comment about the level of CP violation. A first step here would be to measure A_{CP} independently in the two decay channels

$D^0 \to K^+K^-$ and $D^0 \to \pi^+\pi^-$. A second main ingredient is given by performing a set of independent measurements that may be used as both cross checks and to constrain the various parameters involved, for example ϕ_{MIX} and $\beta_{c,eff}$. This can be done for example by performing time-dependent studies of the two decays $D^0 \to K^+K^-$ and $D^0 \to \pi^+\pi^-$, allowing one to disentangle CP violation in interference and decay amplitudes. As discussed in the next section, a time-dependent approach not only may suggest if there is new physics showing up in the charm sector (through the constraint of $\beta_{c,eff}$), but it may provide an alternative method for a high precision measurement of ϕ_{MIX}.

2.4 Time-dependent formalism

To define the time-dependent formalism of the decay of a D^0 meson, two different cases of D^0 meson production have been considered: un-correlated and correlated D^0 production. Un-correlated D^0's are produced from the decays of B mesons in electron-positron colliders when particles are collided at a center of mass energy corresponding to the $\Upsilon(4S)$ resonance (or above[5] threshold there is a non-zero finite cross section for B mesons production; for $\sqrt{s} > 10.58 GeV/c^2$ one produces B's which decay subsequently into D's), or from $c\bar{c}$ continuum, or in hadron machines they can be produced both promptly or as decay products of heavier particles. The correlated D^0 mesons are instead produced in an electron-positron machine running at a center of mass energy corresponding to the $\Psi(3770)$ resonance ($J^{PC} = 1^{--}$), and the correlation refers to the fact that the $D^0 - \overline{D}^0$ pairs are produced as an ensemble of entangled states Φ [25]:

$$\Phi = \frac{1}{\sqrt{2}} \left(D_1^0 \overline{D}_2^0 - \overline{D}_1^0 D_2^0 \right) \tag{2.36}$$

where the subscript 1, 2 indicates the first or second meson in the pair and the wave function is antisymmetric because of Bose symmetry. At the time one of the mesons decays the wave function collapses into a definite state

[5] Above the $b\bar{b}$ threshold.

corresponding to either the first ($D_1^0\overline{D}_2^0$) or the second ($\overline{D}_1^0 D_2^0$) ordering [25] (for a discussion on entanglement see for example ref. [26]).

Due to quantum number conservation, when the decay of the first of the D meson happens (D^0 mesons are pseudoscalars, so $J^P = 0$) at some time t_1, the flavour of both are determined as the opposite types. This follows straight from Eq. 2.36. The un-decayed D meson is allowed to mix as it propagates through space-time, until it finally decays at time t_2. We are interested in events where one D decays into a flavour specific final state so that we can tag the charm quark as a c or $\overline{c}$ and the other D decays into a *CP* eigenstate of interest (either K^+K^- or $\pi^+\pi^-$). The proper time difference *Deltat* between the decay of the two D mesons is a signed quantity, where $\Delta t > 0$ when the *CP* decay occurs after the flavor tag decay, whilst $\Delta t < 0$ is for the opposite time ordering of decays. For example in this thesis negative Δt is obtained when the decay to the *CP* eigenstate happens before the semileptonic decay used for tagging, and positive t is related to events in which the decay into the *CP* eigenstate happens after the semileptonic decay. We have obtained the time evolution for both situations described above [11], and these are summarised in the next section.

2.4.1 The time evolution of D^0 mesons

The equations describing the time evolution of correlated and un-correlated D^0 mesons have been obtained in [11], these are (un-correlated case through the process $e^+e^- \to D^{*+}X$, $D^{*+} \to D^0\pi_s^+$)

$$\Gamma(P^0 \to f) \propto e^{-\Gamma_1 t}\left[\frac{(h_+)}{2} + \frac{Re(\lambda_f)}{1+|\lambda_f|^2}(h_-) \quad + \right.$$
$$\left. e^{\Delta\Gamma t/2}\left(\frac{1-|\lambda_f|^2}{1+|\lambda_f|^2}\cos\Delta M t - \frac{2Im(\lambda_f)}{1+|\lambda_f|^2}\sin\Delta M t\right)\right], \tag{2.37}$$

$$\Gamma(\overline{P}^0 \to f) \propto e^{-\Gamma_1 t}\left[\frac{(h_+)}{2} + \frac{Re(\lambda_f)}{1+|\lambda_f|^2}(h_-) \quad + \right.$$
$$\left. e^{\Delta\Gamma t/2}\left(-\frac{1-|\lambda_f|^2}{1+|\lambda_f|^2}\cos\Delta M t + \frac{2Im(\lambda_f)}{1+|\lambda_f|^2}\sin\Delta M t\right)\right], \tag{2.38}$$

(correlated case, e.g. $e^+e^- \to \Psi(3770) \to \overline{D^0}D^0$)

$$\Gamma(P^0 \to f) \propto e^{-\Gamma_1|\Delta t|}\left[\frac{h_+}{2} + \frac{Re(\lambda_f)}{1+|\lambda_f|^2}h_- \quad + \right.$$
$$\left. e^{\Delta\Gamma\Delta t/2}\left(\frac{1-|\lambda_f|^2}{1+|\lambda_f|^2}\cos\Delta M\Delta t - \frac{2Im(\lambda_f)}{1+|\lambda_f|^2}\sin\Delta M\Delta t\right)\right], \tag{2.39}$$

$$\Gamma(\overline{P}^0 \to f) \propto e^{-\Gamma_1|\Delta t|}\left[\frac{h_+}{2} + \frac{Re(\lambda_f)}{1+|\lambda_f|^2}h_- \quad + \right.$$
$$\left. e^{\Delta\Gamma\Delta t/2}\left(-\frac{1-|\lambda_f|^2}{1+|\lambda_f|^2}\cos\Delta M\Delta t + \frac{2Im(\lambda_f)}{1+|\lambda_f|^2}\sin\Delta M\Delta t\right)\right], \tag{2.40}$$

where $h_\pm = 1 \pm e^{\Delta\Gamma\Delta t}$ and $\lambda_f = \frac{q}{p}\frac{\overline{A}}{A}$. Monte Carlo samples according to the obtained time evolutions have been generated and these, for the correlated case, are shown in Fig. 2.6. Considering Eqns (2.37,2.38,2.39,2.40) the

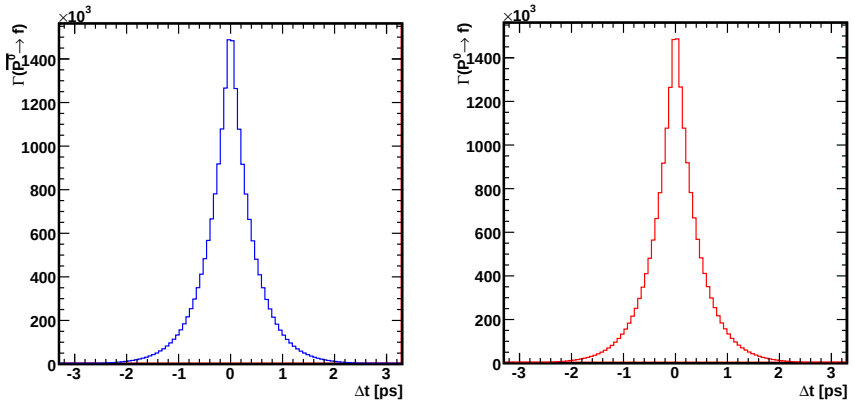

Figure 2.6: Generated distributions of decay time according to Eqs. (2.39) and (2.40) for $\overline{D^0} \to f$(left) and for $D^0 \to f$(right) produced at the center-of-mass energy of the $\Psi(3770)$.

time-dependent asymmetries associated with the time evolution of the D^0 mesons are written in terms of the physical decay rates including the mistag probability as follows

$$\Gamma^{Phys}(t) = (1-\omega)\Gamma(t) + \overline{\omega}\,\overline{\Gamma}(t), \tag{2.41}$$
$$\overline{\Gamma}^{Phys}(t) = \omega\Gamma(t) + (1-\overline{\omega})\overline{\Gamma}(t), \tag{2.42}$$

and

$$\Gamma^{Phys}(\Delta t) = (1-\overline{\omega})\Gamma(\Delta t) + \omega\,\overline{\Gamma}(\Delta t), \quad (2.43)$$

$$\overline{\Gamma}^{Phys}(\Delta t) = \overline{\omega}\Gamma(\Delta t) + (1-\omega)\overline{\Gamma}(\Delta t), \quad (2.44)$$

where $\Gamma(t)$ and $\overline{\Gamma}(t)$ are from Eqns. (2.37) and (2.38), $\Gamma(\Delta t)$ and $\overline{\Gamma}(\Delta t)$ are from Eqns. (2.39) and (2.40), and ω ($\overline{\omega}$) represents the mistag probability for the particle (anti-particle). Hence for un-correlated mesons the CP asymmetry is

$$\mathcal{A}^{Phys}(t) = \frac{\overline{\Gamma}^{Phys}(t) - \Gamma^{Phys}(t)}{\overline{\Gamma}^{Phys}(t) + \Gamma^{Phys}(t)} = \Delta\omega + \frac{(D-\Delta\omega)e^{\Delta\Gamma t/2}[(|\lambda_f|^2-1)\cos\Delta M t + 2Im\lambda_f \sin\Delta M t]}{h_+(1+|\lambda_f|^2)/2 + Re(\lambda_f)h_-}, \quad (2.45)$$

where $\Delta\omega = \omega - \overline{\omega}$ and D is the dilution factor defined as $D = 1 - 2\omega$. From the convention we followed in the definition of the dilution factor we obtain a non-trivial asymmetry offset in the event that $\omega \neq \overline{\omega}$. With a similar procedure for the correlated meson production case one obtains

$$\mathcal{A}^{Phys}(\Delta t) = \frac{\overline{\Gamma}^{Phys}(\Delta t) - \Gamma^{Phys}(\Delta t)}{\overline{\Gamma}^{Phys}(\Delta t) + \Gamma^{Phys}(\Delta t)} = -\Delta\omega + \frac{(D+\Delta\omega)e^{\Delta\Gamma\Delta t/2}[(|\lambda_f|^2-1)\cos\Delta M\Delta t + 2Im\lambda_f \sin\Delta M\Delta t]}{h_+(1+|\lambda_f|^2)/2 + Re(\lambda_f)h_-}. \quad (2.46)$$

(Note the difference in sign between the first term in Eqns. (2.45) and (2.46), which arises from the fact that ω and $\overline{\omega}$ get interchanged between the correlated and uncorrelated cases. For a fuller discussion see Ref. [11].) The above equations may be written in terms of x and y allowing for the measurement of the mixing parameters. We report here the time-dependent asymmetry equation for correlated mesons (similar results may be obtained in the uncorrelated case):

$$\mathcal{A}^{Phys}_{x,y}(\Delta t) = -\Delta\omega + \frac{(D+\Delta\omega)e^{y\Gamma\Delta t}[(|\lambda_f|^2-1)\cos x\Gamma\Delta t + 2Im\lambda_f \sin x\Gamma\Delta t]}{h_+(1+|\lambda_f|^2)/2 + Re(\lambda_f)h_-}. \quad (2.47)$$

I will show in Sec. 2.7 the results of numerical simulations based on Eq. (2.47), showing that only a measurement of x is possible.

2.5 CP eigenstates

In Ref. [11] we considered a sample of 35 two and three body CP eigenstate decays of D^0 mesons and evaluated the CKM contributions to the decay amplitudes, and the decays of interest ($D^0 \to K^+K^-$ and $D^0 \to \pi^+\pi^-$) are shown in Tab. (2.2). We are interested in the weak phase that may be

Table 2.2: CP eigenstate modes showing topologies involved in the process in terms of the CKM factors related to T (tree), CS (color suppressed tree), P_q, and W_{EX} (W-exchange) transitions and their relative η_{CP} eigenvalue [11].

mode	η_{CP}	T	CS	P_q	W_{EX}
$D^0 \to K^+K^-$	$+1$	$V_{cs}V_{us}^*$		$V_{cq}V_{uq}^*$	$V_{cd}V_{ud}^*$
$D^0 \to \pi^+\pi^-$	$+1$	$V_{cd}V_{ud}^*$		$V_{cq}V_{uq}^*$	$V_{cd}V_{ud}^*$

extracted using each decay of the list shown and we concentrate here on two of these channels: $D^0 \to K^+K^-$ and $D^0 \to \pi^+\pi^-$. When studying time-dependent CP violation, as previously mentioned, we are interested in the value of λ_f which contains the relative phase of $D^0 \leftrightarrows \overline{D}^0$ mixing (ϕ_{MIX}), and an overall weak phase difference related to the decay of the D^0 meson to a specific CP eigenstate f_{CP} (ϕ_{CP}), and the amplitude $\overline{A}$ (A) of the decay of a $\overline{D}^0$ meson. The amplitude A may be written as

$$A = |T|e^{i(\phi_T+\delta_T)} + |CS|e^{i(\phi_{CS}+\delta_{CS})} + |W|e^{i(\phi_W+\delta_W)} + \sum_{q=d,s,b} |P_q|e^{i(\phi_q+\delta_{P_q})} \tag{2.48}$$

where the ϕ_j, $j = T, CS, W, q$ are the weak phases of the tree, color suppressed tree, W exchange and penguin amplitudes (mediated by a loop involving down type quarks q) respectively, δ_j are the strong phases associated with the different processes and the coefficients of the exponentials are the magnitudes corresponding to those amplitudes. The decays $D^0 \to K^+K^-$ and $D^0 \to \pi^+\pi^-$ are tree dominated and for a first rudimentary measurement of time-dependent CP asymmetries other contributions can be neglected. It follows that

$$\lambda_f \approx \left|\frac{q}{p}\right| e^{i\phi_{MIX}} e^{-2i\phi_T^W}, \tag{2.49}$$

where in the ratio $\overline{A}/A$, $|T|$ and $e^{i\delta_T}$ cancel. By considering the elements of Tab. (2.2) one can evaluate the products of the CKM factors involved in all the process and for the decays $D^0 \to K^+K^-$ and $D^0 \to \pi^+\pi^-$. These are given by

$$V_{cs}V_{us}^* = \lambda - \frac{\lambda^3}{2} - \left(\frac{1}{8} + \frac{A^2}{2}\right)\lambda^5, \tag{2.50}$$

$$V_{cd}V_{ud}^* = -\lambda + \frac{\lambda^3}{2} + \frac{\lambda^5}{8} + \frac{A^2\lambda^5}{2}[1 - 2(\bar{\rho} + i\bar{\eta})], \tag{2.51}$$

$$V_{cb}V_{ub}^* = A^2\lambda^5(\bar{\rho} + i\bar{\eta}), \tag{2.52}$$

where $V_{cd}V_{ud}^*$ and $V_{cb}V_{ub}^*$ are complex. $V_{cb}V_{ub}^*$ has a large phase equivalent to γ_c and $V_{cd}V_{ud}^*$ is related to the small phase β_c. We are interested in the study of these two decay channels because a constraint of the angle β_c in the *charm* triangle could be obtained by combining the two as shown in Section 2.5.3 (clearly a more precise measurement of this angle would require the understanding of the role of the penguin topologies and a precision measurement of q/p as well as good systematic control which is long way off).

2.5.1 $D^0 \to K^+K^-$

The decay channel $D^0 \to K^+K^-$ is dominated by a real tree amplitude involving the $V_{cs}V_{us}^*$ CKM factor which is of the order of λ, while the imaginary part of $V_{cd}V_{ud}^*$ (of the order of λ^5) only appears in a sub-dominant penguin transition and in the negligible weak exchange amplitude. The different decay topologies are illustrated in Fig. 2.7. Hence one would expect at leading

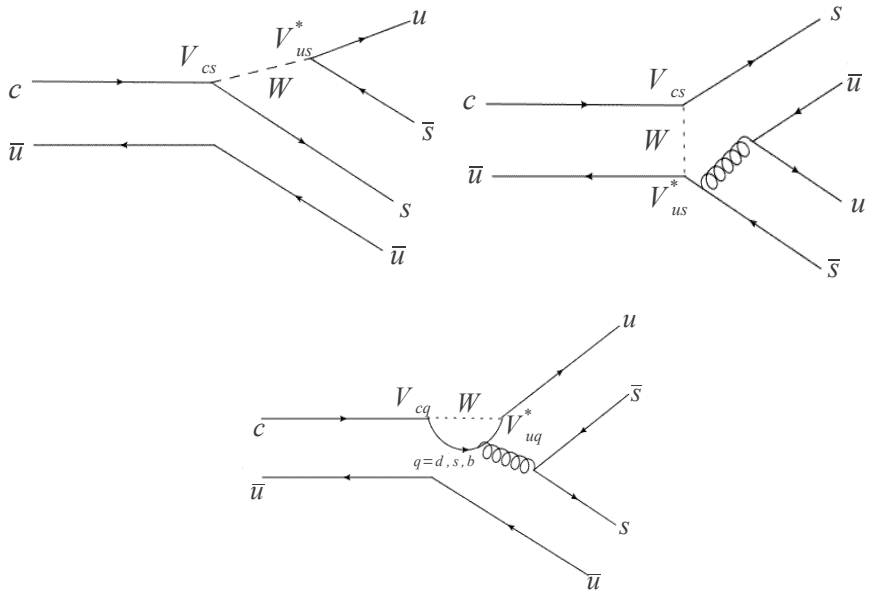

Figure 2.7: Tree (top-left), W exchange(top-right) and penguin (bottom) topologies for $D^0 \to K^+K^-$.

order to observe an asymmetry which is consistent with the mixing phase ϕ_{MIX} without any contribution from the CKM phase. Hence this channel may be used to provide a measurement of both $|q/p|$ and ϕ_{MIX}, in addition to other channels that are available. The SM prediction of the CP asymmetry for this channel is small hence this is an ideal mode to use when searching for new physics.

2.5.2 $D^0 \to \pi^+\pi^-$

The decay channel $D^0 \to \pi^+\pi^-$ measures $V_{cd}V_{ud}^*$ in the leading order tree, in the W-exchange and in one of penguin amplitudes topologies (Fig. 2.8). One of the two remaining penguin amplitudes, mediated by a b quark loop is negligible, the other is of the order of λ. The non-trivial penguin topologies are doubly Cabibbo suppressed (DCS) loops proceeding at order λ^2, whereas the tree amplitude is a singly Cabibbo suppressed (SCS) process. A first

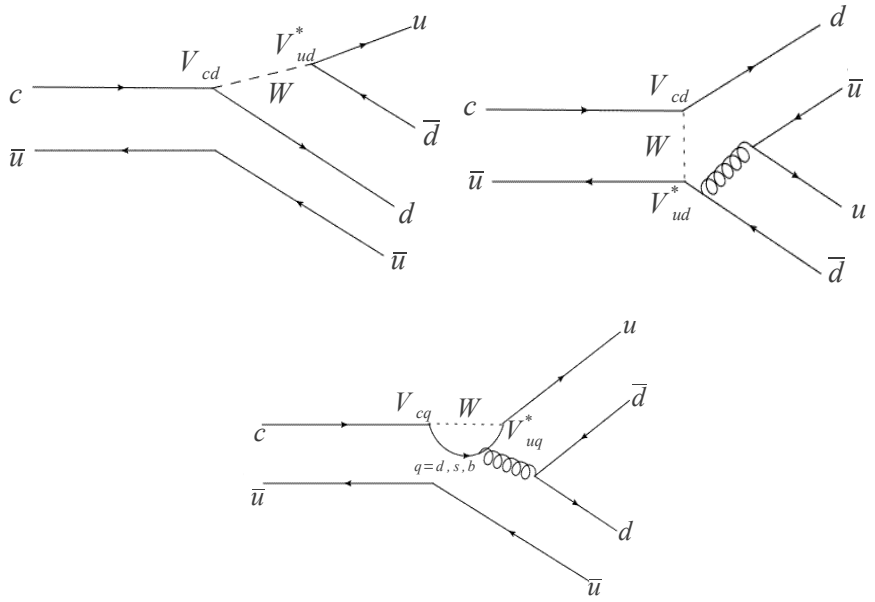

Figure 2.8: Tree (top-left), W exchange (top-right) and penguin (bottom) topologies for $D^0 \to \pi^+\pi^-$.

measurement of this channel, ignoring the penguin amplitudes contribution to the decay, would yield $Im\lambda_f \approx sin(\phi_{MIX} - 2\beta_c)$. So in principle a measurement of β_c could be made up to a four-fold ambiguity that would arise from taking the arcsin of the phase, if one is able to precisely determine the mixing phase. However, in general a more complete theoretical analysis is required to extract the weak phase and disentangle the contribution from the $c \to s \to u$ penguin using an $Isospin$ analysis which also considers the $D^+ \to \pi^+\pi^0$ and $D^0 \to \pi^0\pi^0$ decay [27].

2.5.3 A first measurement of $\beta_{c,eff}$

I have shown in the previous sections that the decays $D^0 \to \pi^+\pi^-$ and $D^0 \to K^+K^-$ provide measurements of $arg(\lambda_f) = arg(\lambda_{\pi\pi}) = \phi_{MIX} - 2\beta_{c,eff}$ and $arg(\lambda_f) = arg(\lambda_{KK}) \simeq \phi_{MIX}$, respectively. If one combines the two channels by taking the difference between the measured phases, it is possible to constrain the value of $\beta_{c,eff}$ considering that $arg(\lambda_{\pi\pi}) - arg(\lambda_{KK}) = \phi_{MIX} + 2\beta_{c,eff} - \phi_{MIX} = 2\beta_{c,eff}$.

It is very important to mention here that while this measurement is very appealing, since it might allow one to study the CKM structure of CP violation through the study of one angle the charm unitarity triangle, it presents some possibly strong limitations. The contribution from penguin amplitudes with weak phases that differ from the leading order tree amplitude means that one does not measure β_c directly, but measures an effective parameter $\beta_{c,eff}$. The difference between the two parameters has been estimated to be $\simeq$3 degrees [27]. In order to probe small values of β_c it would be necessary to develop a reliable strategy to control the biases caused by these contributions.

2.6 Flavour tagging

In this section the different ways to flavour tag the neutral D mesons in different experimental environments are discussed and illustrative examples are given. The identification of one or more final states that can unambiguously be used to determine the flavour of a neutral meson decaying to a CP eigenstate of interest is at the basis of the flavour tagging. As previously noted, the tag assignment is probabilistic and it has an associated probability to be wrong. This probability, denoted by ω, is called the mistag probability and it is an essential quantity to determine how good a decay channel is to perform a flavour tag. An important quantity related to the mistag probability is the previously defined *dilution*. When the dilution is close to one, then the chosen decay channel is a good channel to perform the flavour tag. Correlated D mesons are produced in electron-positron colliders running at the centre of mass energy of the $\Psi(3770)$. The flavour tag may be accomplished by considering semi-leptonic decays of one D meson via the process $D \to K^{(*)\pm}l^{\mp}\nu_l$:

the D^0 is associated with a l^+ in the final state, the $\overline{D}^0$ is associated with a l^- Fig. 2.9 (sometime this is referred to as opposite side tagging). In this process the flavour is unambiguously assigned and the mistag probability ω is essentially zero. One may also consider using hadronically tagged events,

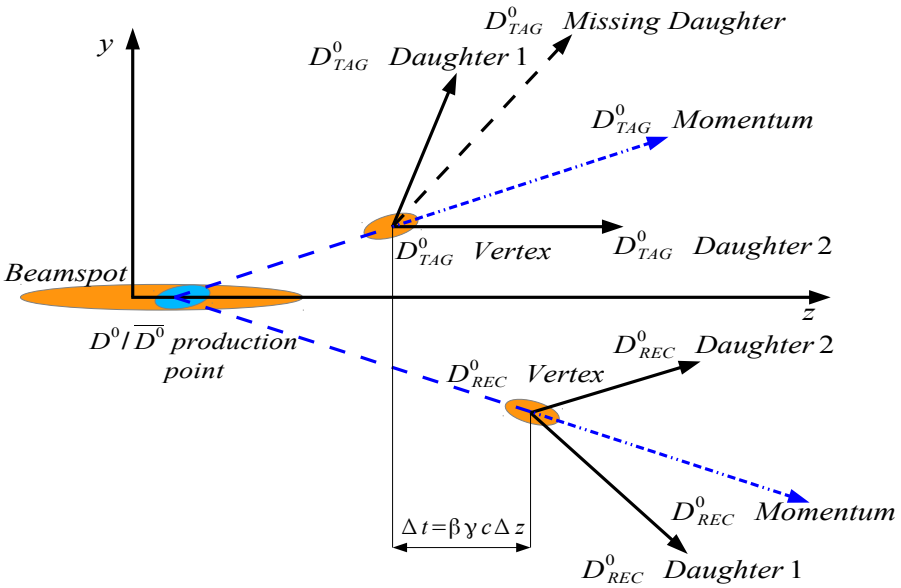

Figure 2.9: An example of a semi-leptonic tagged event with one D meson decaying into a CP eigenstate decay, and the other decaying into a semileptonic tag decay performed at *charm threshold*.

for example $D^0 \to K^-X$ (K^+X), where X is anything, which corresponds to 54% (3%) of all D^0 meson decays from which one would expect $\omega \simeq 0.03$, and that the asymmetry in particle identification of K^+ and K^- in the detector will naturally lead to a small, but non-zero value of $\Delta\omega$. The non-zero value of $\Delta\omega$ is a consequence of the difference in the interaction cross section with the detector of K^+ and K^-, in fact by looking at the quark content of the two mesons, $(s, \bar{u})$ for K^- and $(u, \bar{s})$ for K^+, one can see that the $\bar{u}$ quark from the K^- will tend to annihilate with a u quark of a proton/neutron when passing through the detector material. Additional to the different interaction cross section, there is the problem of quantum correlation, which means

that the tag probability contains an interference term involving a priori unknown parameters [28]. Based on Ref. [29] one expects that there would be approximately 4.8 million kaon tagged $D^0 \to \pi^+\pi^-$ events in $1.0\,\mathrm{ab}^{-1}$ of data collected at the charm threshold. The flavour tag of un-correlated D^0 mesons can be accomplished in two different ways. The first, common to both hadronic collider environments and B factories, consists in the identification of a low momentum pion (slow pion, $\pi_s^{\pm}$), plus the decay products of the D^0 meson. The processes in which neutral D mesons are produced are $D^{*+} \to D^0\pi^+$ and $D^{*-} \to \overline{D}^0\pi^-$, and in this way the assignment is physically unambiguous: if the neutral D meson is produced in association with a π_s^+ then the flavour of the neutral D meson is D^0, vice-versa if it is produced in association with a π_s^- then the flavour is $\overline{D}^0$ (sometimes this is referred to as same side tag). A second possibility is the identification of D^0 mesons coming from the semileptonic decays of a $b-$hadron such as the processes $B \to D^0 X\mu^-\nu_\mu$ and $B \to \overline{D}^0 X\mu^-\overline{\nu}_\mu$, and also in this case the assignment is unambiguous. If the neutral D meson is produced in association with a μ_s^+ then the flavour of the neutral D meson is $\overline{D}^0$, vice-versa if it is produced in association with a μ_s^- then the flavour is D^0. Both the situations just described are depicted in Fig. 2.10.

2.7 Monte Carlo studies of a time-dependent analysis

As previously discussed, the decay $D^0 \to K^+K^-$ can be used to measure ϕ_{MIX}, the decay $D^0 \to \pi^+\pi^-$ can be used to measure $\phi_{MIX} - 2\beta_{c,eff}$, hence the difference between the two channels will provide a measurement of the angle $\beta_{c,eff}$. To evaluate the asymmetries, and estimate the precision on $\beta_{c,eff}$ that one might achieve in different experimental environments (Super$B$, LHCb, Belle II), I generated a set of one hundred Monte Carlo data samples per experiment according to the distributions given in Eqns. (2.37) and (2.38) for un-correlated D^0 mesons, and Eqns. (2.39) and (2.40) for correlated D^0 mesons, with the parameters involved (ΔM, $\Delta\Gamma$, Γ) calculated

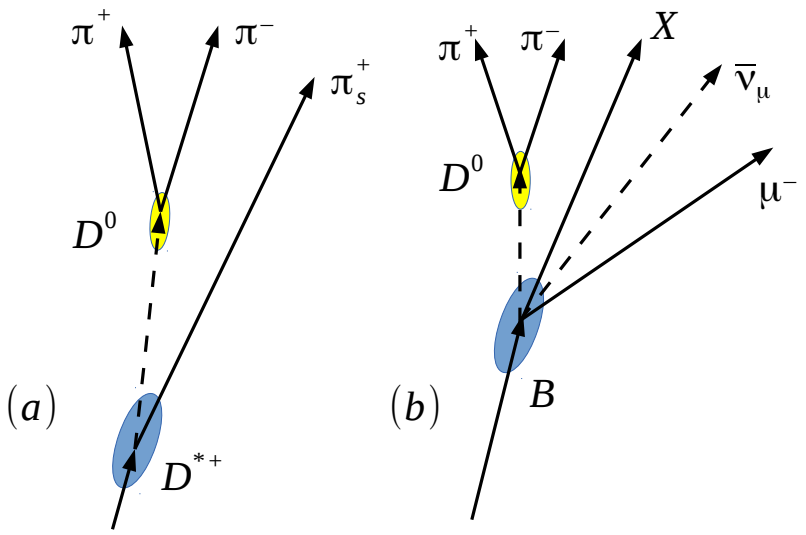

Figure 2.10: Examples of un-correlated neutral D meson flavour tagging. In (a) a tag performed through the identification of a low momentum pion with the D^0 decaying to $\pi^+\pi^-$, in (b) a $D^0 \to \pi^+\pi^-$ tagged in an hadronic collider is identified through the semileptonic decay of a b-hadron.

in Ref. [14] and ignoring t smearing or detector acceptance[6]; each data sample size is based on the expected number of tagged D^0 decays in each of the mentioned experiment. The asymmetries given in Eqns. (2.45) and (2.46) are calculated including the expected mistag probabilities, and a binned fit to the simulated data is performed. The distributions that are considered here have been expressed as function of $|\lambda_f|$ and $arg(\lambda_f) \equiv \phi = \phi_{MIX} - 2\phi_{CP}$, and the fit is performed keeping $|\lambda_f| = 1$ and allowing $arg(\lambda_f)$ to vary. The same results are obtained when $|\lambda_f|$ is also allowed to vary in the fit. It is important to mention that a measurement of $\lambda_f \neq 1$ in an experiment would be a signature of CP violation [11].

[6]These deficiencies are accounted for in the next chapters for the Super$B$ experiment, where a run at charm threshold ($\Psi(3770)$) was considered.

2.7.1 Summary on estimates of the number of events

In this section I present a summary of the number of events that were considered for the time-dependent analysis for each of the discussed experiments. The Super$B$ experiment, described in Chapter 3, was expected to collect 0.5 ab^{-1} with the possibility to consider a longer data taking period to obtain 1.0 ab^{-1} of data at the center-of-mass energy equivalent to that of the $\Psi(3770)$ (charm threshold). With 0.5 ab^{-1} of data one would expect to accumulate approximately 1.8×10^9 D mesons pairs. The CLEO-c experiment when studying $D^0 \to \pi^+\pi^-$ candidates semileptonically tagged has achieved an efficiency of 50% with a data sample of 281 pb^{-1} [29]. Preliminary studies have shown that it is reasonable at Super$B$ to assume a similar efficiency, hence one would expect to record 4.90×10^5 (2.4×10^6) $D^0 \to \pi^+\pi^-$ and 1.38×10^6 (0.68×10^7) $D^0 \to K^+K^-$ semileptonically (Kaon) tagged events[7]. At the $\Upsilon(4S)$ one would expect that efficiencies similar to those achieved at *BABAR* will be achieved at Super$B$ and Belle II. With 384 fb^{-1} of data collected at the $\Upsilon(4S)$ *BABAR* recorded 30679 D^* tagged $D^0 \to \pi^+\pi^-$ [30], from this we estimate that 6.60×10^6 (1.86×10^7) $D^0 \to \pi^+\pi^-$ ($D^0 \to K^+K^-$) D^* tagged events can be reconstructed with a data sample of 75 ab^{-1} at Super$B$, and that 4.40×10^6 (1.17×10^7) $D^0 \to \pi^+\pi^-$ ($D^0 \to K^+K^-$) D^* tagged events can be reconstructed with a data sample of 50 ab^{-1} at Belle II assuming similar performance with respect to Super$B$. We have estimated that LHCb will collect 4.9×10^6 D^* tagged $D^0 \to \pi^+\pi^-$ decays in $5\,\text{fb}^{-1}$ of data and 0.7×10^6 D^* tagged $D^0 \to \pi^+\pi^-$ decays, based on the $0.62\,\text{fb}^{-1}$ of data shown in [17].

2.7.2 Super$B$ at the $\Upsilon(4S)$

The Super$B$ Collaboration was expected to start taking data in 2017 [31] [32] [33] [34], and the integrated luminosity that would have been achieved with the full program was expected to be $75\,\text{ab}^{-1}$. With this luminosity one would expect to reconstruct 6.6×10^6 tagged $D^0 \to \pi^+\pi^-$ events in a data sample

[7] In this thesis only the semileptonic decay $D^0 \to K^-e^+\nu_e$ was considered to perform tagging, so that one would expect to collect a third of the events discussed here.

of $75\,\mathrm{ab}^{-1}$ with a purity of 98% [11][8]. The results of the numerical time-dependent CP analysis are shown in Fig. 2.11. The asymmetry parameters

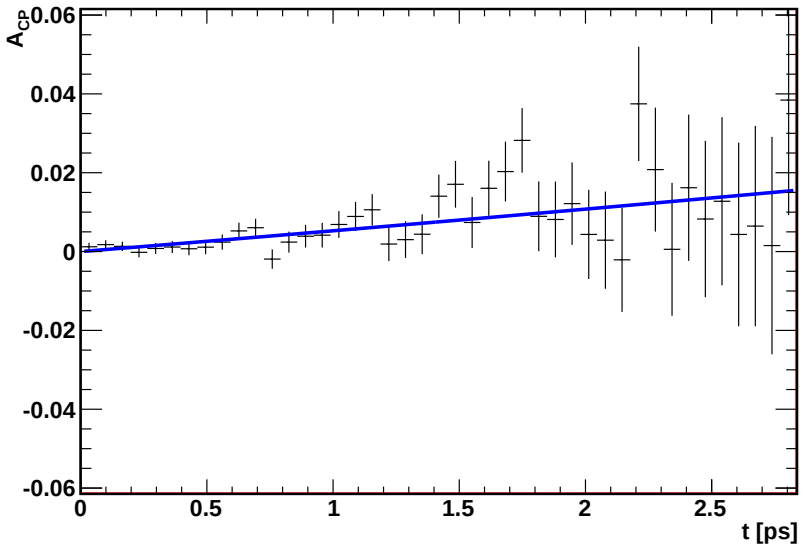

Figure 2.11: The time-dependent CP asymmetry expected for $D^0 \to \pi^+\pi^-$ decays in a $75\,\mathrm{ab}^{-1}$ sample of data at the $\Upsilon(4S)$.

determined here have a precision of $\sigma_{arg(\lambda_{\pi\pi})} = \sigma_{\phi_{\pi\pi}} = 2.2^o$. The same procedure when applied to the $D^0 \to K^+K^-$ channel to measure $\sigma_{arg(\lambda_{KK})} = \sigma_{\phi_{KK}}$, for which one would expect to reconstruct 1.8×10^7 events, leads to a statistical precision of $\sigma_{\phi_{KK}} = 1.6^o$. When the results from $D^0 \to K^+K^-$ and $D^0 \to \pi^+\pi^-$ are combined one obtains a statistical precision $\sigma_{\beta_{c,eff}} = 1.3^\circ$ on $\beta_{c,eff}$.

2.7.3 Super$B$ at the $\Psi(3770)$

The Super$B$ Collaboration was planning to have a dedicated run at the center of mass energy of the $\Psi(3770)$ resonance, to collect an integrated luminosity of $1.0\,\mathrm{ab}^{-1}$. With this luminosity one would expect to record 979000

[8]This work was motivated by the prospect of an asymmetric energy charm threshold run at Super$B$, but also looked at other possibilities. The Super$B$ project however, was cancelled at the end of 2012.

$D^0 \to \pi^+\pi^-$ reconstructed events, when the full set of semi-leptonic decays $K^{(*)}\ell\nu_\ell$ $\ell = e, \mu$ is used to tag the flavor of D^0 mesons (with negligible mistag probability). The results of the numerical analysis are shown in Fig. 2.12. The phase $\phi_{\pi\pi}$ could be measured with a precision of $\sigma_{\phi_{\pi\pi}} = 5.7^o$. One

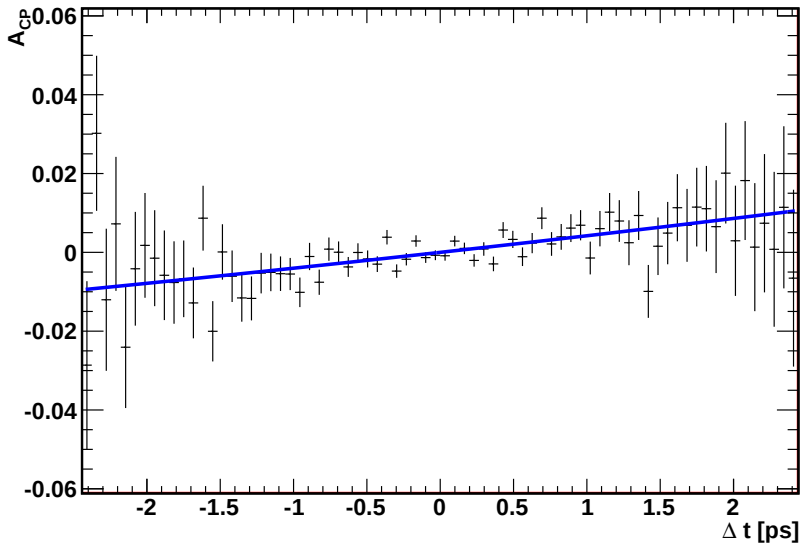

Figure 2.12: The time-dependent CP asymmetry expected for $D^0 \to \pi^+\pi^-$ decays in $1\,\mathrm{ab}^{-1}$ sample of data at the $\Psi(3770)$.

may also consider using hadronically tagged events, for example $D^0 \to K^-X$ (K^+X), where X is anything, which corresponds to 54% (3%) of all D^0 meson decays from which one would expect $\omega \simeq 0.03$, and that the asymmetry in particle identification of K^+ and K^- in the detector will naturally lead to a small, but non-zero value of $\Delta\omega$. We expect that there would be approximately 4.8 million kaon tagged $D^0 \to \pi^+\pi^-$ events in $1.0\,\mathrm{ab}^{-1}$ at charm threshold. Using these data alone, one would be able to measure $\phi_{\pi\pi}$ to a statistical precision of 2.7°. Hence if one combines the results from semi-leptonic and kaon tagged events, a statistical precision $\sigma_{\phi_{\pi\pi}} \sim 1.4°$ is achievable.

2.7.4 LHCb

Another possible scenario is that of measuring time-dependent asymmetries from uncorrelated D mesons produced in a hadronic environment, in particular at the LHCb experiment. Here dilution and background effects are expected to be larger than those at an e^+e^- machine, but the data are already available and it would be interesting to perform the time-dependent analysis, especially after the recent results on time integrated CP violation in Refs. [18] [19]. As already mentioned, a measurement of $|\lambda_f| \neq 1$ will signify CP violation. Given that the measurement of λ_f is likely expected to be dominated by uncertainties, especially in ω and $\Delta\omega$, it is not clear what the ultimate precision obtained from LHCb will be. The best way to ascertain this would be to perform the measurement on the existing data set. We have estimated that LHCb will collect 4.9×10^6 D^* tagged $D^0 \to \pi^+\pi^-$ decays in $5\,\text{fb}^{-1}$ of data, based on the $0.62\,\text{fb}^{-1}$ of data shown in [17], and we consider also the outcome of a measurement for $1.1\,\text{fb}^{-1}$ (equivalent to 0.7×10^6 D^* tagged $D^0 \to \pi^+\pi^-$ decays) already available after the 2011 LHC run. In [11] we estimate a purity of $\simeq 90\%$ and $\omega \simeq 6\%$ which results in the asymmetry obtained in Fig. 2.13 for $5\,\text{fb}^{-1}$ of data. This fit is translated into a potential measurement of the phase $\phi_{\pi\pi}$ with a statistical precision of 3.0° with $5.0\,\text{fb}^{-1}$ of data. With $1.1\,\text{fb}^{-1}$ of data I estimate that LHCb may be able to reach a statistical precision of 8° on $\phi_{\pi\pi}$.

2.7.5 Belle II

The last scenario considered here is that of Belle II with $50\,\text{ab}^{-1}$ of data collected at the center of mass energy of the $\Upsilon(4S)$, where Belle II indicates the planned upgrade of the Belle experiment [35]. We have considered the same efficiency and mistag probability as for the Super$B$ experiment (as discussed in 2.7.2), and one would expect that 4.4×10^6 D^* tagged $D^0 \to \pi^+\pi^-$ will be collected. The resulting asymmetry is shown in Fig. 2.14, and the statistical precision on $\phi_{\pi\pi}$ obtained for this scenario is estimated to be 2.8°.

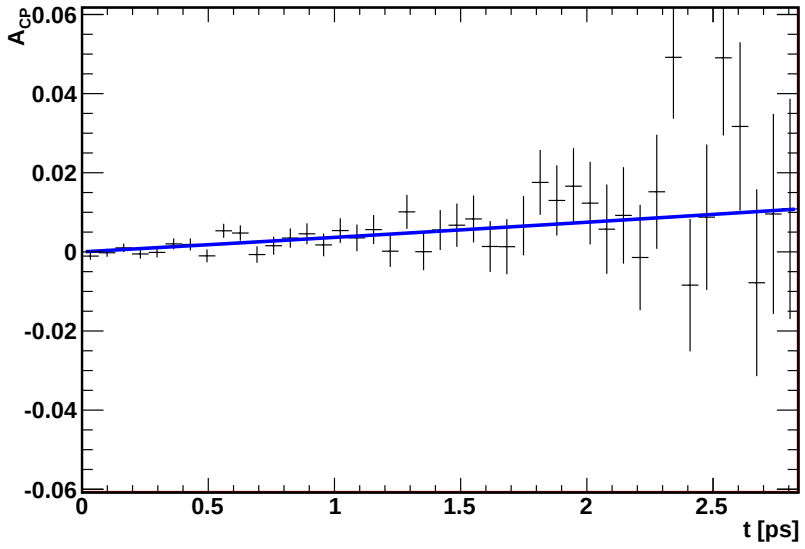

Figure 2.13: The time-dependent CP asymmetry expected for $D^0 \to \pi^+\pi^-$ decays in a $5\,\text{fb}^{-1}$ sample of data at LHCb.

2.8 Time-dependent sensitivity studies

A summary of all our results is presented in this section. I first show the results regarding the sensitivities achievable when measuring $\beta_{c,eff}$, ϕ_{MIX} and ϕ_{CP}, then I will show the results regarding the achievable sensitivity to x together with a preliminary systematic uncertainties study which considers the systematic effect due to the present limited knowledge of y.

2.8.1 Sensitivity to $\beta_{c,eff}$, ϕ_{MIX} and ϕ_{CP}

As said previously, we considered only leading order (tree) amplitudes for the decays we are studying, and a summary of the possible sensitivities that the different experiments could achieve when measuring the mixing and the weak phase under this assumption are given here. To first order the decay $D^0 \to K^+K^-$ measures the mixing phase, therefore one can consider $\phi_{KK} = arg(\lambda_{KK}) = \phi_{MIX}$ and use a time-dependent analysis to measure it to a precision of $\approx 1.3^o - 1.6^o$ as shown in Tab. (2.3). However, it has to be noted

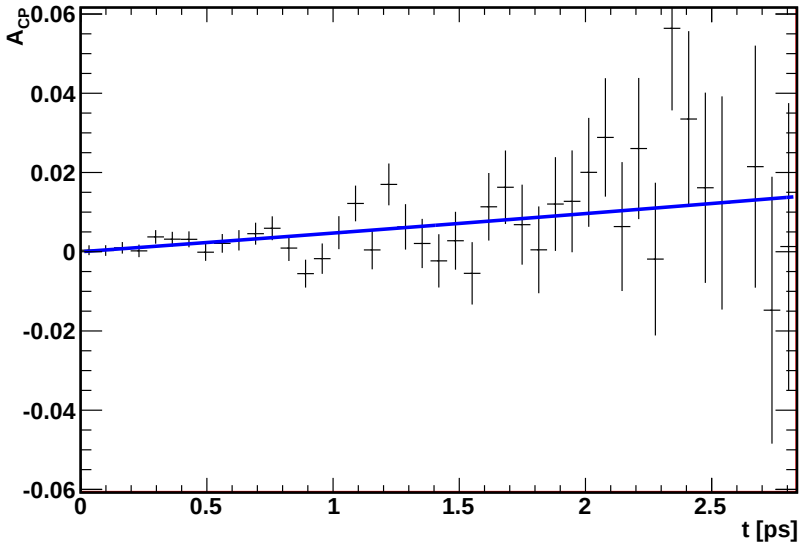

Figure 2.14: The time-dependent CP asymmetry expected for $D^0 \to \pi^+\pi^-$ decays in a $50\,\mathrm{ab}^{-1}$ sample of data at the $\Upsilon(4S)$.

Table 2.3: Summary of expected uncertainties from $1\,\mathrm{ab}^{-1}$ of data at charm threshold, $75\,\mathrm{ab}^{-1}$ of data at the $\Upsilon(4S)$, $5\,\mathrm{fb}^{-1}$ of data from LHCb, and $50\,\mathrm{ab}^{-1}$ of data at the $\Upsilon(4S)$ at Belle II. The column marked SL corresponds to semi-leptonic tagged events, and the column SL+K to semi-leptonic and kaon tagged events at charm threshold. The last row shows the precision in $\beta_{c,eff}$ expected from a simultaneous fit to $\pi\pi$ and KK where we assume that, for KK, the decay is dominated by a tree amplitude.

Parameter	Super$B$			LHCb	Belle II
	$\Psi(3770)$	$\Psi(3770)$	$\Upsilon(4S)$		
	SL	SL+K	$\pi_s^\pm$	$\pi_s^\pm$	$\pi_s^\pm$
$\sigma_{\phi_{\pi\pi}} = \sigma_{arg(\lambda_{\pi\pi})}$	5.7°	2.4°	2.2°	3.0°	2.8°
$\sigma_{\phi_{KK}} = \sigma_{arg(\lambda_{KK})}$	3.5°	1.4°	1.3°	1.6°	1.7°
$\sigma_{\beta_{c,eff}}$	3.3°	1.4°	1.3°	1.7°	1.6°

that while at Super$B$ a higher precision will be reached when considering the $\Upsilon(4S)$ run that should have taken five years, the run at charm threshold would require just a few months.

2.8.2 Sensitivity to x

We consider the same data sample discussed in the previous sections for $D^0 \to \pi^+\pi^-$ and $D^0 \to K^+K^-$. While we find that results from the time-dependent analysis are not sensitive to the parameter y, and that with 1.0 ab^{-1} of data collected at charm threshold at Super$B$ it will be possible to improve the currently known precision on x by a factor of two with respect to the most recent HFAG values [9]. The precisions that could be reached are shown in Table 2.4, where it is clear that a time-dependent analysis may provide an improvement on the current precision in the determination of x.

2.8.3 Systematic uncertainties

The knowledge of the parameters x and y which define mixing is limited by their relative uncertainties. Since the analysis discussed here is not sensitive to the parameter y, we considered the most recent results from HFAG [9] and evaluate the effect of varying the parameter $\Delta\Gamma = 2y\Gamma$ by $\pm 1\sigma$. This is the systematic uncertainty due to the limited precision in y. The value of the uncertainty in the parameter y is 0.013% and it is given in [9]. The resulting systematic uncertainty on ϕ_{KK}, $\phi_{\pi\pi}$, and $\beta_{c,eff}$ coming from the uncertainties on y is shown in Table 2.5.

2.8.4 Combined results for Super$B$

Table 2.6 shows the combined sensitivities obtained when considering 75 ab^{-1} of data collected at the $\Upsilon(4S)$ and 1 ab^{-1} of data collected at the $\psi(3770)$ at the Super$B$ experiment, where both statistical and studied and the systematic uncertainty from y. It is clear from Table 2.6 that the systematic uncertainty studied so far will not play a dominant role in the determination of $\phi_{\pi\pi}$, ϕ_{KK} and $\beta_{c,eff}$. Here the reader should note that these estimates are based on numerical studies only and do not take into account the resolution

Table 2.4: Estimates of the sensitivity on x for all the experimental scenarios discussed and their projected luminosities for the decays $D^0 \to \pi^+\pi^-$ and $D^0 \to K^+K^-$ and $\phi = \phi_{MIX} - 2\beta_{c,eff}$. SL corresponds to semi-leptonic tagged events, and SL+K corresponds to semi-leptonic and kaon tagged events at charm threshold.

Experiment/HFAG	$\sigma_x(\phi = \pm 10^o)$	$\sigma_x(\phi = \pm 20^o)$
Super$B$ [$\Upsilon(4S)$]		
$D^0 \to \pi^+\pi^-$	0.12%	0.06%
$D^0 \to K^+K^-$	0.07%	0.04%
Super$B$ [$\Psi(3770)$]		
$D^0 \to \pi^+\pi^-(SL)$	0.30%	0.15%
$D^0 \to \pi^+\pi^-(SL+K)$	0.13%	0.06%
$D^0 \to K^+K^-(SL)$	0.19%	0.10%
$D^0 \to K^+K^-(SL+K)$	0.08%	0.04%
LHCb		
$D^0 \to \pi^+\pi^-$ (1.1 fb^{-1})	0.40%	0.20%
$D^0 \to K^+K^-$ (1.1 fb^{-1})	0.20%	0.11%
$D^0 \to \pi^+\pi^-$ (5.0 fb^{-1})	0.15%	0.08%
$D^0 \to K^+K^-$ (5.0 fb^{-1})	0.08%	0.04%
Belle II		
$D^0 \to \pi^+\pi^-$	0.14%	0.07%
$D^0 \to K^+K^-$	0.09%	0.04%
HFAG	0.20%	

function that will provide a deeper understanding of the experimental limits when performing such a measurement.

Table 2.5: Summary of expected systematic uncertainties due to the limited knowledge of the parameter y from $1\,\mathrm{ab}^{-1}$ of data at charm threshold and $75\,\mathrm{ab}^{-1}$ of data at the $\Upsilon(4S)$. The column marked SL corresponds to semi-leptonic tagged events, and the column SL+K corresponds to semi-leptonic and kaon tagged events at charm threshold while $\pi_s^{\pm}$ refers to the slow pion tag at the $\Upsilon(4S)$.

Parameter	$\Psi(3770)$ SL	$\Psi(3770)$ SL+K	$\Upsilon(4S)$ $\pi_s^{\pm}$
$\sigma_{\phi_{\pi\pi}}(sys.)$	0.5°	0.2°	0.05°
$\sigma_{\phi_{KK}}(sys.)$	0.2°	0.1°	0.02°
$\sigma_{\beta_{c,eff}}(sys.)$	0.27°	0.11°	0.03°

Table 2.6: Combined sensitivities at Super$B$.

Parameter	Statistical sensitivity	Systematic sensitivity
σ_x $(D^0 \to \pi^+\pi^-)$	0.09%	-
σ_x $(D^0 \to K^+K^-)$	0.05%	-
$\sigma_{\phi_{\pi\pi}}$	1.62^o	0.05^o
$\sigma_{\phi_{KK}}$	0.95^o	0.02^o
$\sigma_{\beta_{c,eff}}$	0.95^o	0.03^o

Chapter 3

A super flavour factory experiment

3.1 The Super$B$ experiment at Cabibbo Lab

Super$B$ was an international collaboration aimed at the construction of a very high luminosity ($10^{36} cm^{-2} s^{-1}$ at the $\Upsilon(4S)$ resonance and $10^{35} cm^{-2} s^{-1}$ at the $\Psi(3770)$ resonance) asymmetric energy e^+e^- flavour factory [36] at the Tor Vergata University site in Rome, where the Cabibbo Laboratory was recently founded. Many of the components were to be reused from the PEP-II collider at SLAC in order to save construction costs [36]. The site where the facility was going to be built is shown in Fig. 3.1 [37]. The high luminosity of the Super$B$ experiment represented one of the main goals of the collaboration, and the Super$B$ experiment consisted of three main components that are the injection system, the collider and the detector, these will be described in the following sections. The expected high luminosity would allow one to perform precision tests of the SM via the study of those processes that in the SM are rare and suppressed, in the hope that deviations coming from new physics may be manifest. This approach is complementary to the route taken by the Large Hadron Collider (LHC) experiments. At the LHC the hope is to directly produce new particles at high energy.

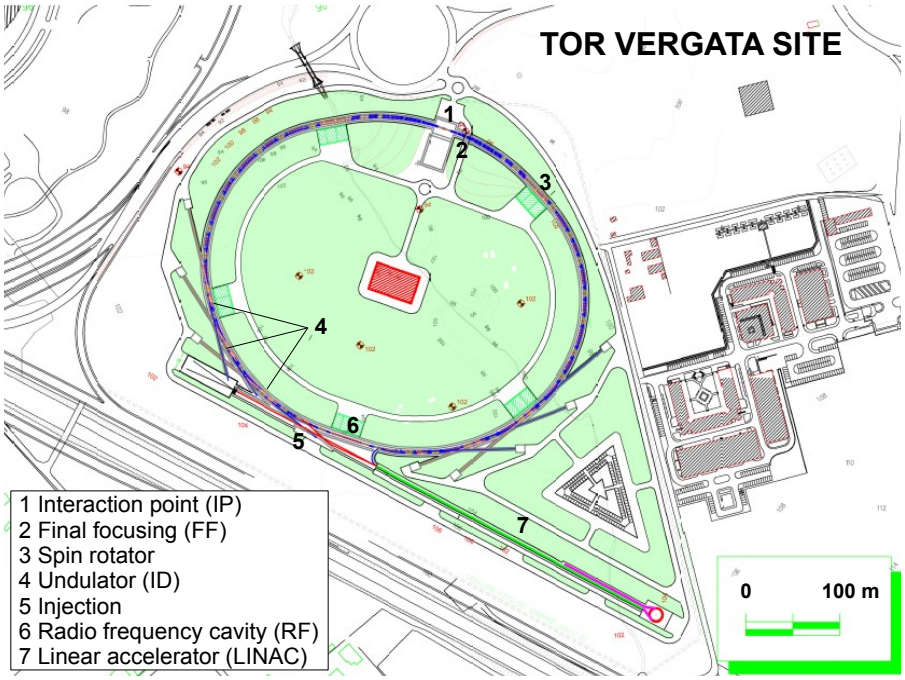

Figure 3.1: View of a proposed layout of the Super$B$ site at the Tor Vergata Campus.

3.2 The injection system and the collider

The injection system design consists of a polarised electron gun, a positron production system, linac sections for the $e^{\pm}$, a damping ring system, and transfer lines connecting these to the main collider rings. At full energy the electrons and positrons were to be injected at 4.2 and 6.7 GeV, respectively [39]. The presented design for the Super$B$ accelerator was based on a total number of 162 *bending* dipole magnets, of which 144 will be located in the arc of the ring, 16 in the final focus region, and 2 are considered for soft bending. A total of 417 $focusing$ quadrupole magnets is considered in the design. Of this 417 quadrupole magnets, 213 should have been located in the arcs and the rest used for final focusing, wigglers, and for the straight section. 230 sextupole magnets of which 4 should have been located in the final focus region were considered in the design. A detailed list of the accelerator parameters may be found in [33] [36].

3.2.1 Crab waist

In an e^+e^- collider the luminosity, L, is given by

$$L = \frac{N^+N^-}{4\pi\sigma_y\sqrt{(\sigma_z \tan\theta/2)^2 + \sigma_x^2}} f_c, \tag{3.1}$$

where f_c is the collision frequency per bunch, $N^{+(-)}$ is the number of positrons (electrons), σ is the beam size in the horizontal (x), vertical (y) and longitudinal (z) directions, θ is the crossing angle of the beams at the interaction point (IP) (the interaction region along with some machine parameters is shown in Fig. 3.2) and $\sigma_{x,y} = \sqrt{\beta_{x,y}\epsilon_{x,y}}$ with β expressing the β-function (in cm) at the collision point, and ϵ representing the area of the emittance. High

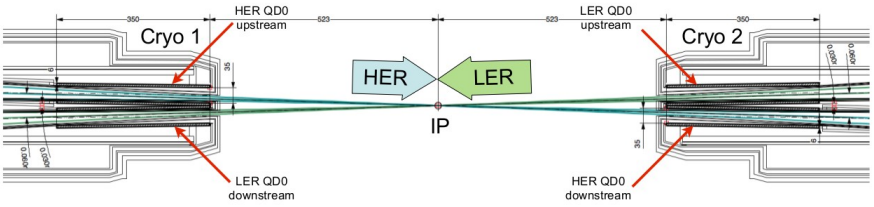

Parameter	SuperB		PEP-II		KEKB		CESR
	HER(e^+)	LER(e^-)	HER(e^-)	LER(e^+)	HER(e^-)	LER(e^+)	
Luminosity ($10^{33}\,\mathrm{cm}^{-2}\mathrm{s}^{-1}$)	1000		12		17		1.2
Circumference (m)	1200		2200		3014		768
Energy (GeV)	6.7	4.18	8.97	3.12	8.0	3.5	5.29
Lorentz $\beta\gamma$ factor	0.238		0.553		0.426		—
Beam current (mA)	1900	2440	1875	2990	1330	1650	370
Particle per bunch ($\times 10^{10}$)	5.1	6.6	5.0	7.9	6.0	7.5	12
h/v emittance (nm / pm)	2.0/5.0	2.5/6.2	73/ 1000	36/ 1000	24/ 600	18/ 600	400/ 4500
h/v $\beta^\star$ (mm)	26/0.26	32/0.21	740/11	210/10	560/6.5	590/5.9	450/21
h/v beam size @ IP (μm/ nm)	7.2/36	8.9/36	147/5000		116/1900	103/1900	420/ 4000

Figure 3.2: View of the Super$B$ interaction region (top) and main machine parameters compared to other experiments (bottom).

luminosity may be achieved using high currents or small emittances.
The general expression for the luminosity can be written as

$$L = f_{coll}\frac{N^+N^-}{4\pi\sigma_y\sigma_x} R_l, \tag{3.2}$$

where f_{coll} represents the collision frequency, $\sigma_{x,y}$ are the rms beam sizes (horizontal and vertical), and R_l is a reduction factor. The option chosen by the Super$B$ Collaboration to increase the luminosity was based on the *crab waist* (CW) scheme for collisions. The Piwinski angle ϕ is defined as

$$\phi = \frac{\sigma_z}{\sigma_x} tan\frac{\theta}{2} \approx \frac{\sigma_z}{\sigma_x}\theta/2, \tag{3.3}$$

and for collision under a crossing angle θ the luminosity L and the horizontal and vertical tune shifts (ξ_x, ξ_y) scale as

$$L \propto \frac{N\xi_y}{\beta_y}, \tag{3.4}$$

$$\xi_y \propto \frac{N\sqrt{\beta_y}}{\sigma_x\sqrt{1+\phi^2}} \approx \frac{2N\sqrt{\beta_y}}{\sigma_z\theta}, \tag{3.5}$$

$$\xi_x \propto \frac{N}{\sigma_x^2(1+\phi^2)} \approx \frac{4N}{(\sigma_z\theta)^2}. \tag{3.6}$$

Flat beams with small horizontal crossing angle ($\theta << 1$) and large Piwinski angle ($\phi >> 1$) are considered here. A large value of the Piwinski angle is obtained by decreasing the horizontal beam size and increasing the crossing angle and as result the luminosity increases: this is the basic idea of the CW scheme and it is obtained by putting one *crab* sextupole magnet before and one after the IP. A simulation of the effect of the crab sextupoles on the beams at the IP is shown in Fig. 3.3. One can see in Fig. 3.3 the effect of using the CW scheme as the transverse profile of interacting bunches are matched at the IP with CW on, and poorly matched when the CW scheme is not used.

3.3 The Detector

The concept for the Super$B$ detector, shown in Fig. 3.4, is derived from the *BABAR* detector with some modifications due to the fact that the machine should have operated at a luminosity which is hundred times larger [31] [32] [36]. A number of components will be reused from *BABAR*, this is the case for example of the quartz bars of the Detector of Internally Reflected Cherenkov light (DIRC) and the barrel of the Electromagnetic Calorimeter (EMC). The

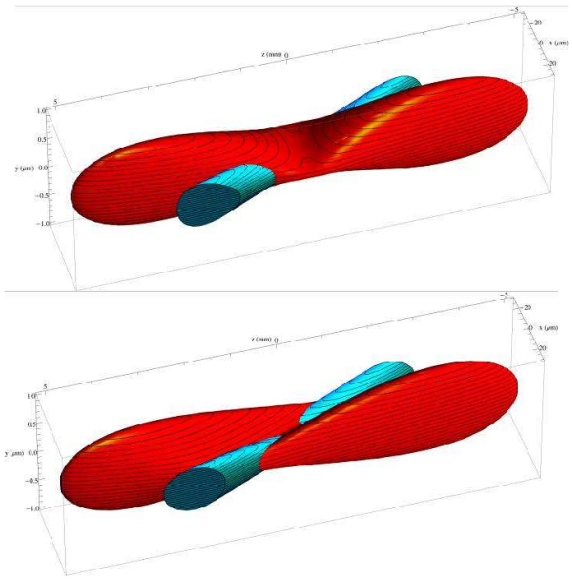

Figure 3.3: (top) Simulation of the beam crossing at the IP with crab sextupoles off and (bottom) with crab sextupole on.

BABAR Silicon Vertex Tracker could not have operated at the Super$B$ luminosity, and its occupancy would have resulted in an inefficient track reconstruction, and for these reasons it was going to be replaced by a new one with an improved design, and with an additional detection layer (Layer 0) at a small radius, mounted off of the beam pipe[1]. Additional absorbers should have also be mounted off of the Instrumented Flux-Return (IFR) [32] [36] [39].

[1]The main difference here is that *BABAR* and Super$B$ would have operated with different boost configurations, and the boost at Super$B$ was to be about one half of that for *BABAR*. As a result the resolution of the vertex detector had to be improved in order to compensate for the reduction in boost.

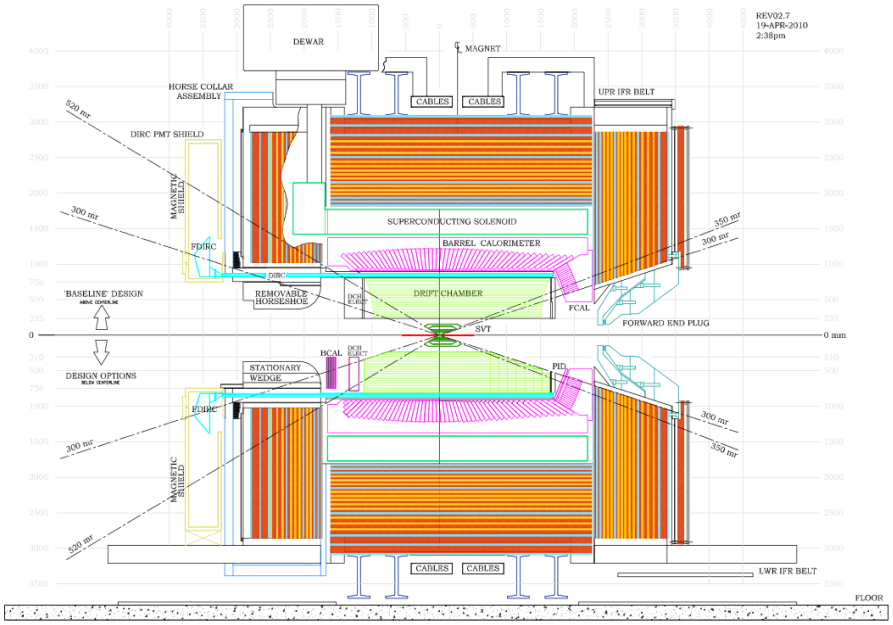

Figure 3.4: Schematic view of the Super$B$ detector.

3.3.1 Silicon vertex tracker (SVT)

The silicon vertex detector represents the most important detector component when performing studies of time-dependent CP violation, since it provides information about the trajectories of charged particles passing through the detector and it allows one to reconstruct the decay vertices of unstable particles. A silicon detector in general, consists of doped wafers of silicon cut from a crystal in which pixels or strips have been implanted. For a doped silicon sensor, when a charged particle passes through it electrons are created, the electric field across a reversed biased p-n junction induces a current, which is integrated and processed by readout electronics. The beam pipe should have had a radius of $\approx$ 1cm and the Super$B$ SVT should have consisted of a six layers of double sided silicon strip detectors surrounding the pipe with a radius from 1.2 to 20 cm. For the Layer closest to beam line, Layer 0, several additional possibilities with respect to the silicon strips were studied. These were based on silicon pixel sensors, and the option involving

monolithic active pixel sensors will be discussed in more detail in Chapter 6. A schematic section of the SVT is shown in Fig. 3.5 [38] [39]. The acceptance

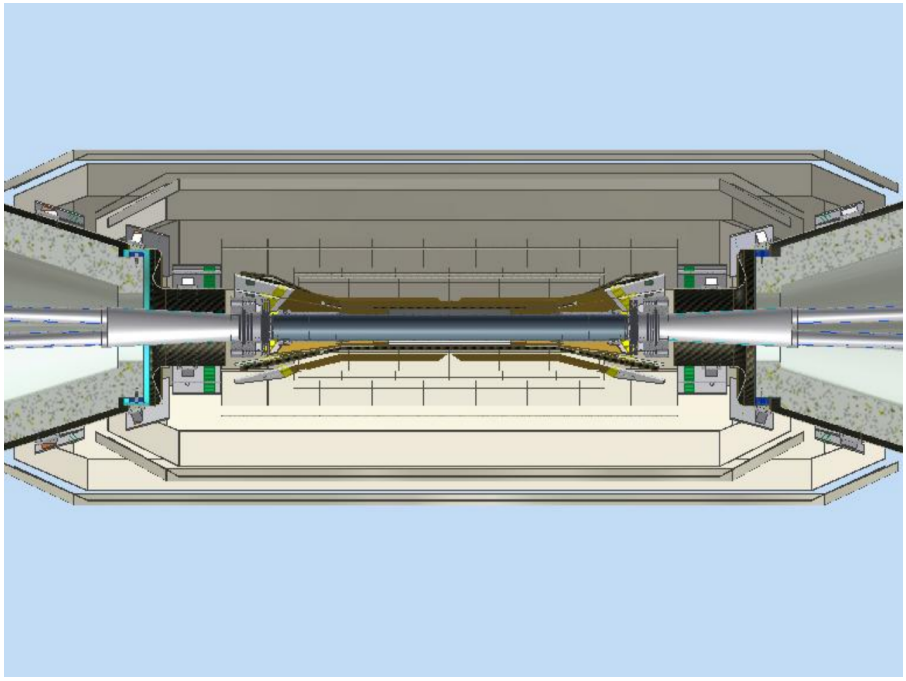

Figure 3.5: Schematic view of the SVT at Super$B$ with Layer 0 in the middle and all the other layers are built up around this.

of the planned SVT was expected to be 300 mrad in the backward/forward directions equivalent to a solid angle coverage of $\approx 95\%$ [32]. Low momentum charged tracks (< 100 MeV) are fully reconstructed inside the SVT, high momentum charged particles deposit energy in the SVT before exiting from it, and the deposits of energy in the SVT are reconstructed as tracks. At the Super$B$ experiment, being at an asymmetric collider, the center-of-mass system would have had a boost along the z-direction (with respect to the laboratory reference frame) due to the asymmetric energies of the colliding beams. This boost plays a very important role in the determination of the precision which one might achieve when evaluating the position of the decay vertex of a given particle ($B^0, D^0, \ldots$) and consequently on the measurement of Δt required for time-dependent studies. The main reason for adding an extra layer to the SVT (Layer 0) with respect to the *BABAR* design was due to

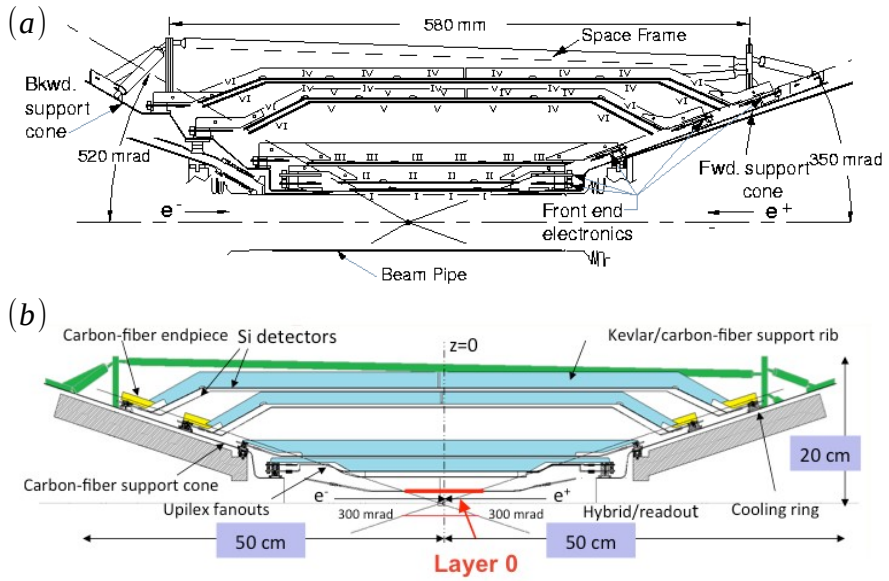

Figure 3.6: Schematic view of the *BABAR* SVT (a) and the Super$B$ SVT (b) with the Layer 0 highlighted.

the fact that the Super$B$ experiment would have had a smaller boost with respect to the one in *BABAR*, as previously said, that needed to be compensated for. The precision on Δt at the $\Upsilon(4S)$ varies from $\approx$ 1ps for a boost factor ($\beta\gamma$) of 0.1 to $\approx$ 0.25 ps for $\beta\gamma = 0.56$. With $\beta\gamma \approx 0.56$ at *BABAR* a precision of 0.6 ps was achieved. A comparison between the decay vertex resolution achieved by *BABAR* and the one that was expected at Super$B$ with a lower boost but with the additional layer 0 is shown in Fig. 3.8 [39], where one can see that even with a smaller boost the Super$B$ experiment would have obtained a better performance than *BABAR*. When looking for time-dependent CP violation in un-correlated D^0 decays, one has to measure the proper time of the D^0, and this is "limited" by the knowledge of its 3-dimensional flight length $\overrightarrow{L}$ and on its momentum $\overrightarrow{p}$ as shown in Eq. 3.7

$$t = \frac{\overrightarrow{L}\,\widehat{p} M_{D^0}}{\overrightarrow{p}}, \tag{3.7}$$

Quantity	Layer 0	Layer 1	Layer 2	Layer 3	Layer 4a	Layer 4b	Layer 5a	Layer 5b
Radius (mm)	15.6	33	40	59	120	124	140	144
Wafers/Module	1	2	4	4	6	6	8	8
Modules/Layer	8	6	6	6	8	8	9	9
Silicon Area (cm^2)	127	554	787	1655	2459	2548	3502	3610
Overlap in ϕ (%)	2.0	2.4	1.8	1.8	4.0	4.0	2.0	2.0
Readout pitch (μm):								
ϕ (u for Layer 0)	54	50	55	100	82–100		82–100	
z (v for Layer 0)	54	100	100	110	210		210	
Floating Strips:								
ϕ (u for Layer 0)	—	—	—	1	1		1	
z (v for Layer 0)	—	1	1	1	1		1	
Intrinsic Resolution (μm):								
ϕ (u for Layer 0)	10	10	10	15	15		15	
z (v for Layer 0)	10	14	14	15	25		25	
Readout Section								
ROS/Module	4	4	4	4	4		4	
ICs/ROS (ϕ-z)	6-6	7-7	7-7	6-10	4-5		4-5	
Readout Channels	24576	21504	21504	24576	36864		41472	
Strip Length Half Module (mm):								
ϕ (u for Layer 0)	20	110	130	190	293	303	369	380
z (v for Layer 0)	20	40	48	70	51–103	103–154	103–154	103–154
Fraction of z-side readout channels with Pairing/Ganging:								
None		77%	55%	65%	4%			
Pairing ×2		23%	45%	35%				
Ganging ×2					73%	74%	25%	16%
Gang.×2 + Pair.×2					23%	24%	41%	43%
Ganging ×3						2%	34%	41%

Figure 3.7: Main parameters of the SVT.

where $\widehat{p}$ and M_{D^0} are the average momentum and the mass of the D^0. A good resolution on $\overrightarrow{L}$ depends on the resolution of the SVT, while a good resolution on the momentum depends on the drift chamber (described in the next paragraph). Results of fast simulation (FastSim) studies regarding the proper time resolution achievable at Super$B$ compared to *BABAR* data, and *BABAR* fast and full simulations are shown in Fig. 3.9 [39]. In the next chapter I will show the sensitivity on Δt that one might have achieved at the Super$B$ experiment when collecting data at the charm threshold with a boost factor $\beta\gamma = 0.28$ (in Appendix C results of simulation for $\beta\gamma = 0.9$ are given). One has to consider that this study for D^0 mesons was not performed in the past due to the fact that the Super$B$ experiment would have been the first experiment running at the charm threshold with asymmetric beam energies.

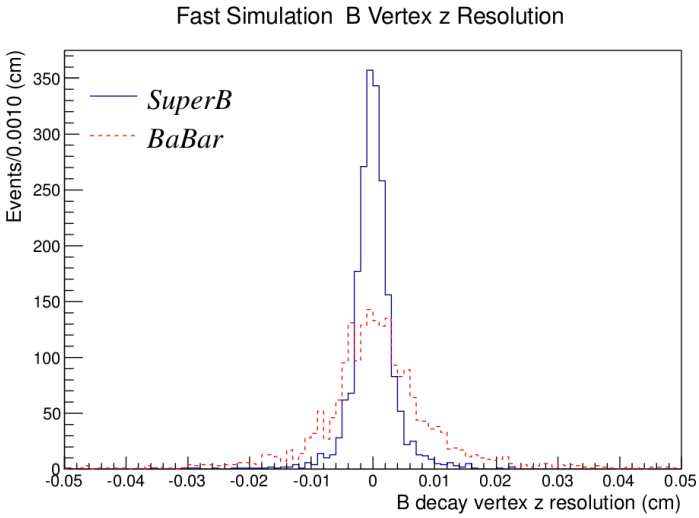

Figure 3.8: Comparison between *BABAR* and Super$B$ on the resolution on the B^0 decay vertex.

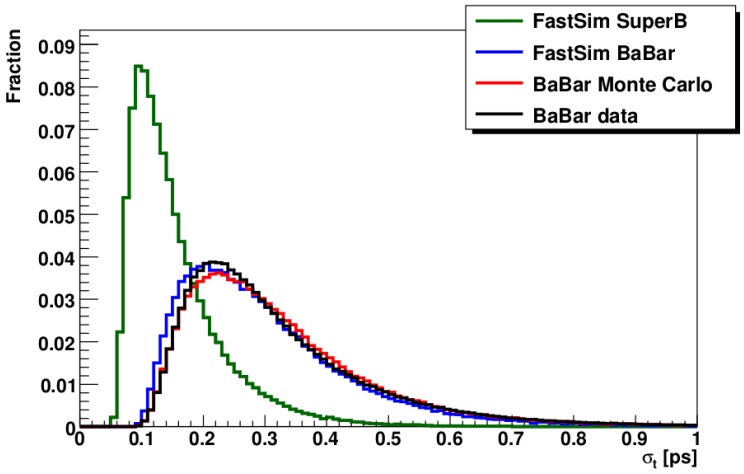

Figure 3.9: Comparison between *BABAR* and Super$B$ on the proper time resolution of uncorrelated D^0 mesons.

3.3.2 Drift Chamber (DCh)

The *drift chamber* (DCh) is a gaseous detector and its purpose is to identify charged particles and to measure their momenta. To understand how the DCh works, we first introduce the concept of a wire chamber. A wire chamber is filled with a carefully chosen gas and contains a large set of wires divided into two categories: The field wires and the sense wires. The *BABAR* DCh was filled with a gas mixture of $80\%He - 20\%IC_4H_{10}$, while for the Super$B$ experiment three possibilities have been studied: $80\%He - 20\%IC_4H_{10}$, $90\%He - 10\%IC_4H_{10}$, $80\%He - 20\%CH_4$ [39]. The *field wires* are fixed to the two edges of the chamber and they are, for instance, parallel to the axis of the chamber (the chamber often has a cylindrical symmetry) and being held at a voltage near ground they are the cathodes the system. A possible geometry for the DCh is shown in Fig. 3.10 [32] [39]. The *sense wires* are held at

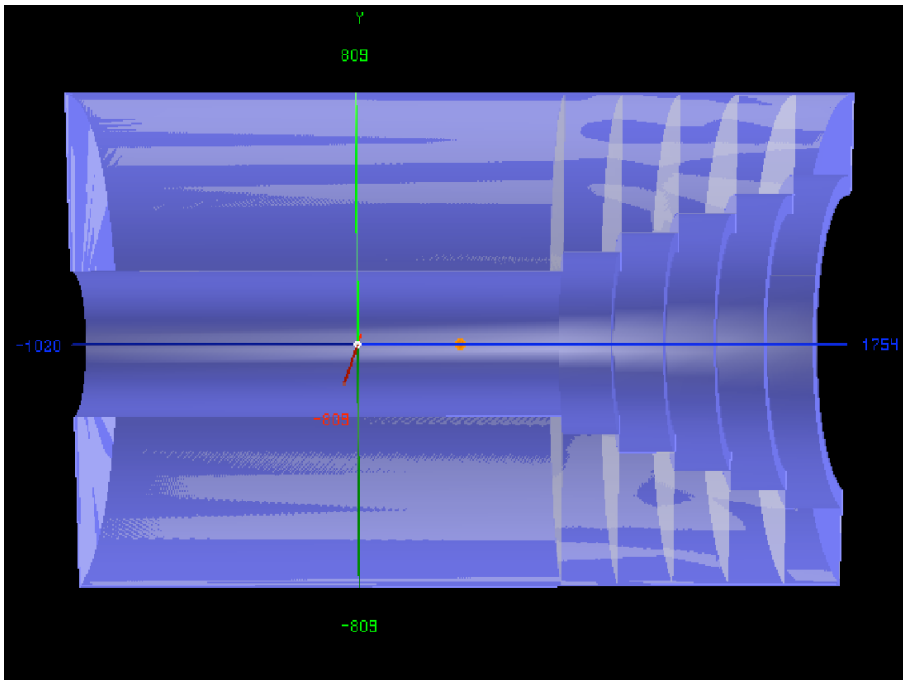

Figure 3.10: GEANT 4 simulation of one possible geometry of the DCh at Super$B$.

an high voltage equivalent to the operating potential and are used for the de-

tection of the electrons coming from ionized atoms. Once a charged particle enters the detector, it will ionize the atoms of the gas and the electrons from the ionized atoms will $drift$ to the sense wires due to the attractive field. The electric field strength will determine the drift velocity of the electrons. When the electrons reach the sense wires, they will produce an electric pulse. By measuring the timing of these electric pulses one can determine the distance of the origin of the electrons from the wire. The chamber is put in a well known magnetic field, so that the curvature of the trajectory of the particles due to the Lorentz force can be determined and, hence, their momenta can be measured. Due to the fact that the Super$B$ Collaboration was planning the reconstruction of both inclusive and exclusive final states, as for *BABAR*, with a high efficiency, a maximal solid angle coverage and highly efficient reconstruction of tracks with a minimum transverse momentum $p_\perp$ as low as 100 MeV/c is required, also considering that a good momentum resolution is very important for time-dependent analyses (see Eq. 3.7). A comparison of the transverse momentum resolution for the proposed DCh geometry for three different gas mixtures is shown in Fig. 3.11 [39].

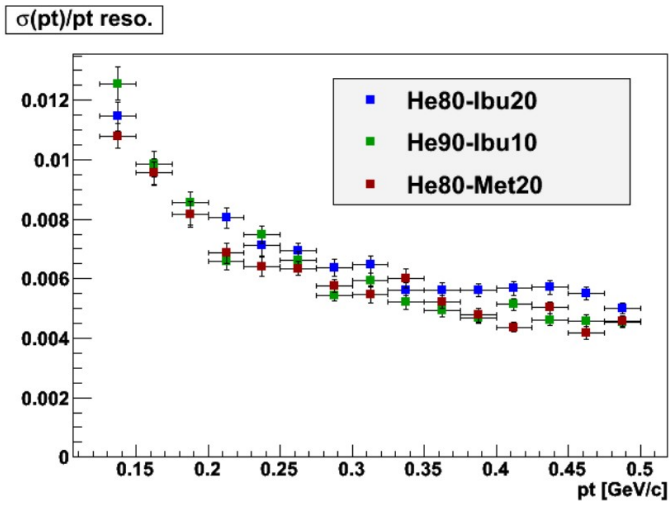

Figure 3.11: Transverse momentum resolution of the DCh at Super$B$, comparing three different gas mixtures.

3.3.3 Detector of internally reflected Cherenkov light (DIRC)

The DIRC shown in Fig. 3.12 [31], is an essential component for charged particle identification (PID). Leptons and low momentum hadrons may be identified by considering the information coming from the EMC and/or the IFR, but to distinguish between high momentum kaons and pions one requires more information. For these particles an additional detector component is required. The aim of the DIRC is to reconstruct the particle mass using Cherenkov radiation generated by a charged particle passing through the quartz crystals that are mounted inside the *bar boxes* and distributed around the DIRC structure. When a charged particle travels through the

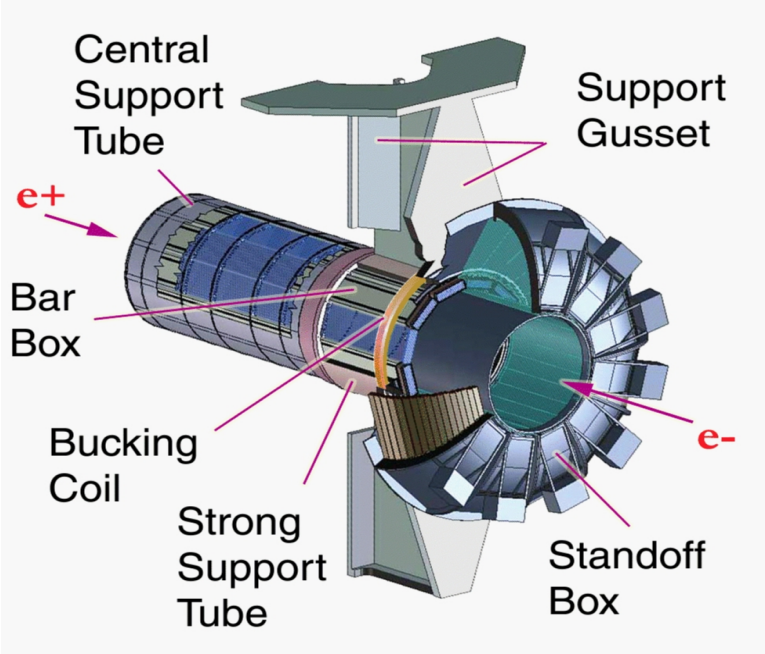

Figure 3.12: Schematic view of the DIRC from *BABAR*.

quartz with a speed higher than the speed of light in the quartz, it will produce Cherenkov radiation, and due to total internal reflections this radiation propagates through the quartz bar and reaches the photon detectors positioned at the end of the quartz bar at an angle α. By combining the

measurement of α with the track angle and momentum measured in the drift chamber, one can determine the particle mass. In *BABAR*, which has a pure water stand off box (SOB) that serves as a region of the detector where Cherenkov rings spread out, one surface of the SOB is instrumented with photomultipliers (PMTs) that will measure the angle at which the light hits the sensor. The Cherenkov radiation is produced at a typical angle θ, called Cherenkov angle, given by

$$\cos\theta = \frac{1}{n\beta}, \tag{3.8}$$

where $\beta = v/c$ is the ratio between the particle velocity and the speed of light and n is the refractive index of the crystal, and by combining the information on the angle at which the radiation is produced (from the Cherenkov ring) with the track momentum measured in the DCh, it is possible to measure the mass of the particle. The Super$B$ concept would have used a fused silica block instrumented with silicon photodiodes instead of a water filled SOB to reduce susceptibility to neutron backgrounds in the detector. The estimated K-π separation for various configurations of the Super$B$ DIRC (FDIRC) is shown in Fig. 3.13 [39]. It is important to mention here that the (F)DIRC was designed for the $\Upsilon(4S)$ run of the Super$B$ experiment, where particles carry higher momenta, while running at the charm threshold ($\Psi(3770)$ for example) the FDIRC would not be necessary, and particle identification can be obtained by studying and combining the energy deposit dE/dx in the SVT and in the DCh.

3.3.4 Electromagnetic calorimeter (EMC)

The purpose of the EMC is to measure with high precision both the position and energy of photons and electrons (positrons) and it represents a very important component in the discriminations between electrons (or positrons) and other charged particles. The EMC consists of one barrel and one endcap, covering 94.1% of 4π solid angle (acceptance). A schematic cross-section of the *BABAR* EMC and the information related to the acceptance in Super$B$ are shown in Fig. 3.14 and the support structure for the barrel is shown in Fig. 3.15 [39]. The barrel consists of 48 CsI(Tl) crystal rings surrounding

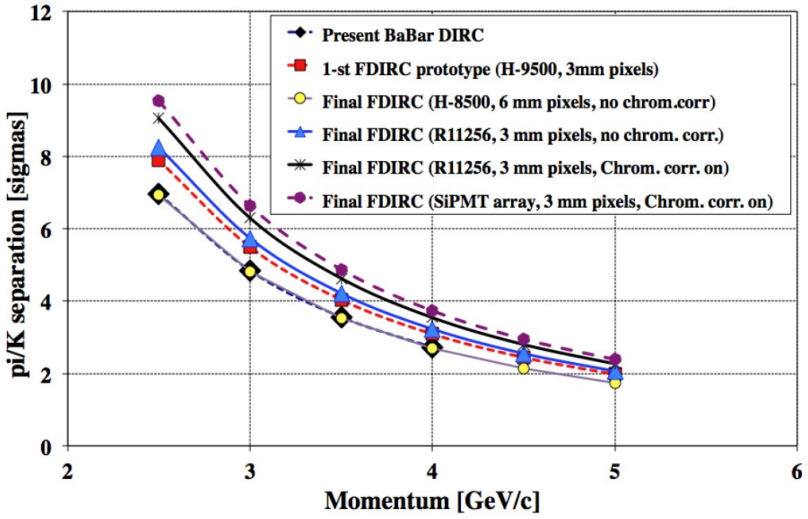

Figure 3.13: K-π separation expected at Super$B$ for various DIRC configuration as function of the particles momenta.

the beam-direction, each one of these rings contains 120 crystals, for a total of 5760 crystals. The proposed endcap, consists of a total of 4500 Lutetium-Yttrium-Orthosilicate (LYSO) Cerium-doped crystals, arranged in 4 concentric groups, Fig. 3.16 [32] [39]. When a particle (charged particle or photon) interacts with a crystal it will produce an electromagnetic shower that in the case of electrons, positrons, and photons is typically fully absorbed by the crystal itself while other particles such as pions or kaons would just deposit a fraction of their energy (typically of the order of 10% with respect to the initial energy). The acceptance of 94.1% of 4π is due to the need for support structures, electric cables, cooling pipes, and space for beam passage. As described in Section 2.6, I will consider semileptonic decays of the D^0 meson and the EMC will be needed for the identification and energy measurement of electrons. For the semileptonic decays involving electrons one has the

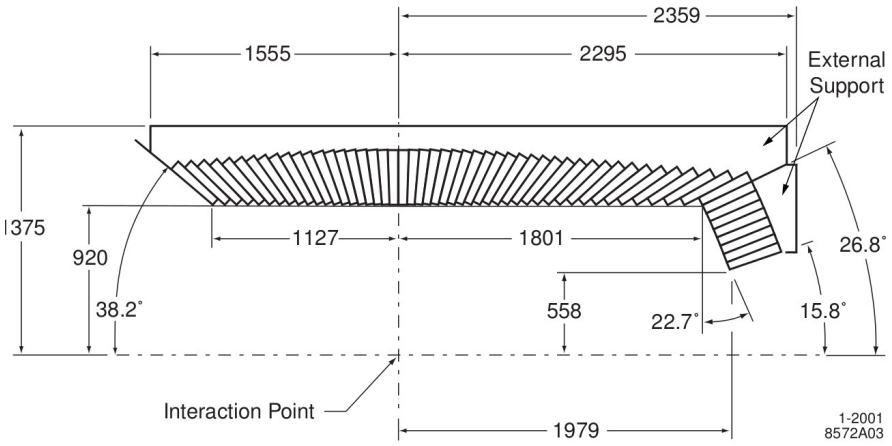

Calorimeter	$\cos\theta$ (lab)		$\cos\theta$ (CM)		Ω (CM)(%)
	minimum	maximum	minimum	maximum	
Backward	-0.98	-0.88	-0.99	-0.93	2.9
Barrel	-0.79	0.89	-0.87	0.81	84
Forward	0.89	0.97	0.81	0.94	6.8

Figure 3.14: (top) Half longitudinal cross-section of the *BABAR* EMC showing the arrangement of the 48 barrel and 8 endcap crystal rings, showing that the detector is axially symmetric around the z-axis with dimensions expressed in mm and (bottom) main coverage parameters.

following branching ratios [14]

$$BR(D^0 \to K^- e^+ \nu_e) = (3.55 \pm 0.05)\%, \tag{3.9}$$

and

$$BR(D^0 \to K^*(892)^- e^+ \nu_e) = (2.16 \pm 0.16)\%. \tag{3.10}$$

Due to the fact that in a semileptonic decay the electron (positron) is produced in association with an antineutrino (neutrino), a good energy resolution of the EMC is needed when reconstructing the D^0 ($\overline{D}^0$) meson. An empirical formula to measure the energy resolution is given by

$$\frac{\sigma(E)}{E} = \frac{a}{E^{1/4} GeV} \oplus b\%. \tag{3.11}$$

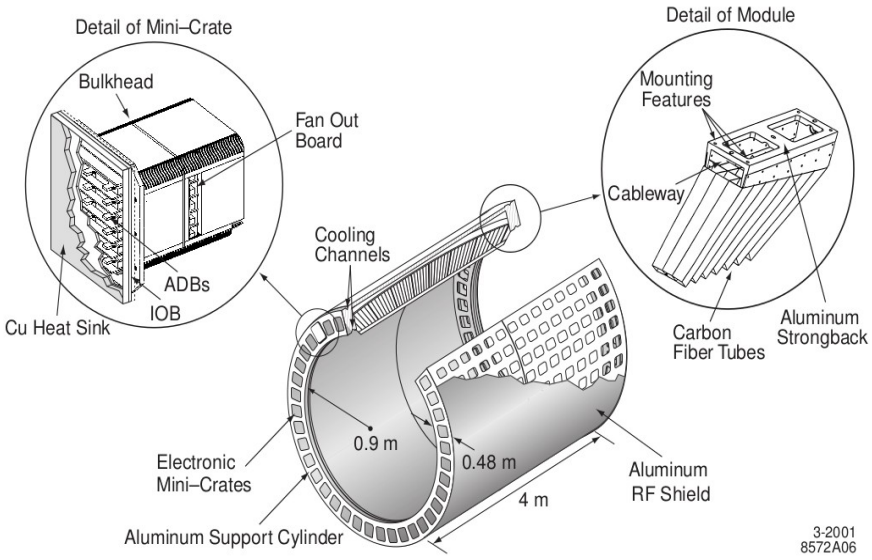

Figure 3.15: EMC barrel support structure Super$B$.

where E and $\sigma(E)$ refers to the energy and the energy resolution (rms) of a photon, both expressed in GeV and a and b, defined as the stochastic term and the noise term, are to be determined experimentally, and the symbol $\oplus$ indicates that the sum is a quadratic sum. The *BABAR* EMC performance in terms of the energy resolution of the crystals for a given energy E expressed in GeV can be parametrised as shown in Eq. 3.12 and in Eq. 3.13

$$\frac{\sigma(E)}{E} = \frac{(2.32 \pm 0.3)\%}{E^{1/4}} \oplus (1.85 \pm 0.12)\%, \tag{3.12}$$

$$\sigma_\theta = \sigma_\phi = \frac{(3.87 \pm 0.07)mrad}{E^{1/4}} \oplus (0.0 \pm 0.4)\%. \tag{3.13}$$

As an illustration of the performance of such an EMC, using a multi-hadron set of data collected in 2001, the *BABAR* Collaboration has measured the π^0 and η mass in their two-photon decays as follow

$$M_{\pi^0 \to \gamma\gamma} = M_{\gamma\gamma}(134.9 \pm 6.5)MeV/c^2, \tag{3.14}$$

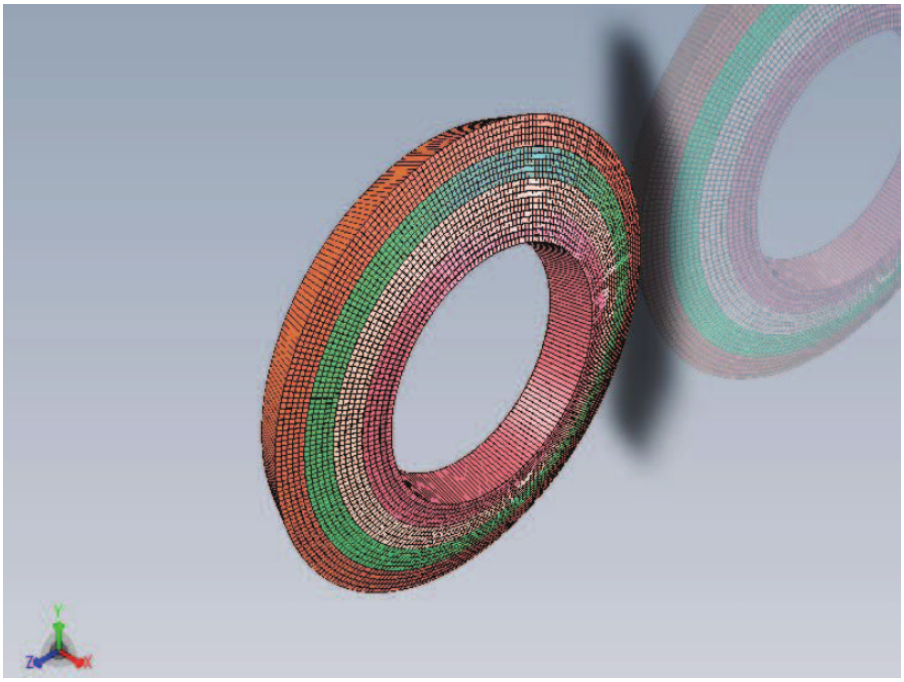

Figure 3.16: GEANT 4 simulation of the EMC endcap at Super$B$.

$$M_{\eta\to\gamma\gamma} = M_{\gamma\gamma}(547.0 \pm 15.5) MeV/c^2, \tag{3.15}$$

In agreement with Eq. 3.12. The Super$B$ experiment would have re-used the *BABAR* barrel, so it was expected to reach the same energy resolution, however the proposed endcap consisting of LYSO crystals might have reached a better precision.

3.3.5 Instrumented flux return (IFR)

The aim of the IFR detector is to identify muons and long lived neutral kaons (i.e. K_L), and neutrons. In the proposed design it should have consisted of 92 cm thick iron yokes (which forms the so-called magnet return yoke) interleaved with eight or nine active layers of highly segmented scintillators. Particle detection is based on the scintillation of the material due to the passage of the particles. A schematic view of the IFR is shown in Fig. 3.17 [39], while in Fig. 3.18 a schematic view of a cross section of the IFR where in blue-gray one sees scintillator layers (nine layers) and in red the iron layers

are shown. The IFR represents another important component of the detector

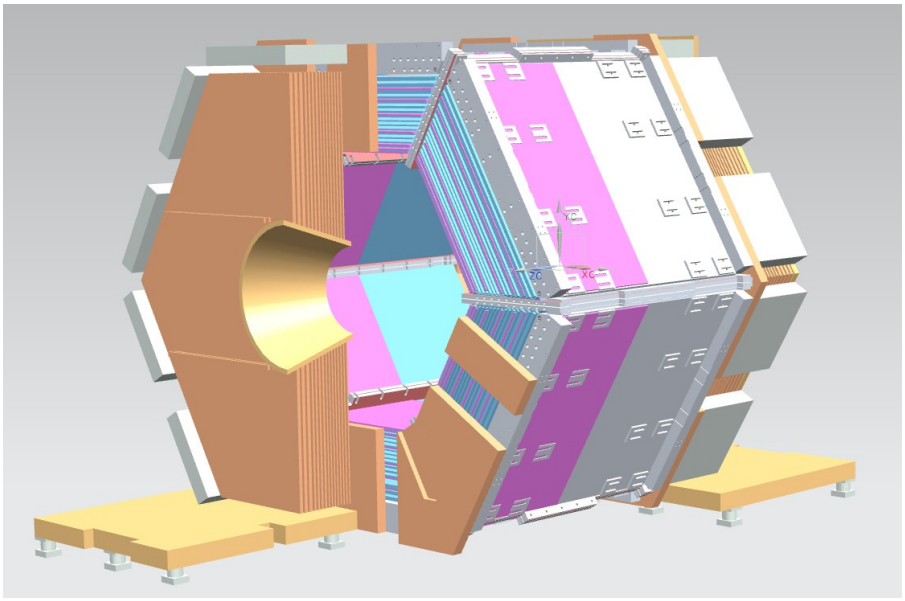

Figure 3.17: GEANT 4 simulation for the IFR at Super$B$ with only half of the forward door region shown.

when looking for time-dependent CP violation in charm. In particular, as shown in Fig. 2.9, the flavour tagging of D^0 mesons at the charm the threshold can be performed using semileptonic decays with a total branching ratios of 5.22% given that [14]

$$BR(D^0 \to K^- \mu^+ \nu_{mu}) = (3.31 \pm 0.13)\%, \tag{3.16}$$

and

$$BR(D^0 \to K^*(892)^- \mu^+ \nu_{mu}) = (1.91 \pm 0.24)\%. \tag{3.17}$$

Also when looking for CP violation in B mesons, the decay channels into final states with muons are important, particularly for the decay $B^0 \to J/\psi K^0$ where $J/\psi \to \mu^+\mu^-$ has a branching ratio $BR(J/\psi \to \mu^+\mu^-) = (5.93 \pm 0.06)\%$ [14]. Synergy between the EMC capability to identify electronic semileptonic tags and IFR capability for the muonic modes in an essential part of the measurement philosophy outlined in this thesis.

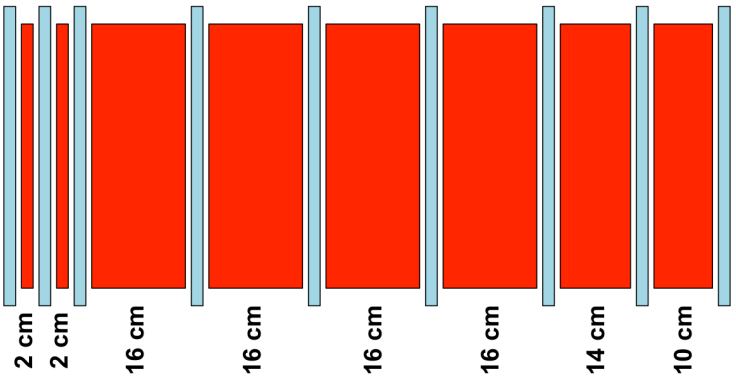

Figure 3.18: Schematic view of the 9 IFR scintillator layers (blue-gray) intervealed by the iron yokes (red) at Super$B$.

3.3.6 Detector Solenoid

The *solenoid* magnet is designed to provide a strong axial magnetic field of 1.5 Tesla (T) in the interaction region inside the detector as shown in Fig. 3.19 with main parameters shown in Fig. 3.20, necessary to have a good momentum resolution from the DCh when the experiment run at the $\Upsilon(4S)$ cms energy, while a lower magnetic field (*i.e.* 1.0 T) would be sufficient when considering a charm threshold run. The beams collide at a crossing angle which is not zero and the magnetic field generated by the solenoid needs to be corrected for by the final beam focussing magnets in order to preserve the small luminous region profile at the interaction point [33] [39]. The intensity of the magnetic field can be changed and a possibility of 1 T magnetic field for the charm threshold run was being investigated. After cancellation of the Super$B$ a formal discussion about the possibility to consider the 1 T solenoid option for a high luminosity τ-*charm* factory took place, but due to the current financial situation in Italy subsequent study of this option was halted.

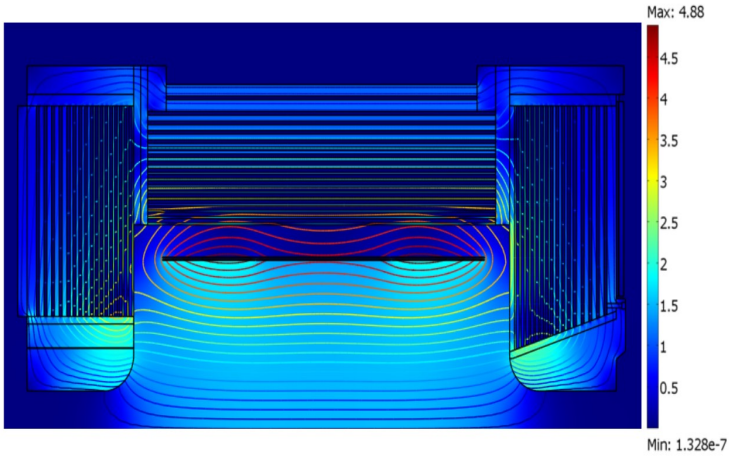

Figure 3.19: Simulation of the generated magnetic field from the (top-half) 1.5 T solenoid at Super$B$.

Central Induction	1.5 T
Conductor peak field	2.3 T
Winding structure	2 layers graded current density
Uniformity in the tracking region	± 3%
Winding axial length	3512 mm at R.T.
Winding mean radius	1530 mm at R.T.
Operating current	4596 A
Inductance	2.57 H
Stored Energy	27 MJ
Total turns	1067
Total length of conductor	10300 m

Figure 3.20: Super$B$ solenoid main parameters.

Chapter 4

Simulation Software at Super$B$

The simulation software for the Super$B$ experiment has two main goals: the optimization of the detector geometry and physics studies. Due to the similarities between the *BABAR* and the Super$B$ experiments, the Super$B$ Collaboration has decided to adapt and use FastSim, a fast simulation (event simulation which is significantly faster (about 100 - 1000 times) than a detailed GEANT-based simulation[1]) software developed for the *BABAR* Collaboration, based on an *Object Oriented* programming paradigm implemented using C++. This simulation software has been developed within the *BABAR* experiment framework until when, in 2009, it became available as a standalone tool.

4.1 FastSim framework

The FastSim software is a modular framework controlled using Tcl (Tool Command Language) whose basic element is the *package*. A package is a set of classes needed to solve a set of similar problems, and there are tens of available packages to cover the most typical problems encountered in a given measurement. The set of all the available packages validated at a given time is called a *release*. At the base of any executable analysis are the *modules* consisting of a package class. One can combine different

[1] A detailed GEANT based simulation is also available, but has not been used for this thesis, as that was impractical given the required computing resources

modules to obtain a *sequence*. Sequences and modules are combined in a *path*, defined as a complete sequence starting with an input module and ending with an output module. Inside each module it is possible to introduce a filter, allowing one to select only particular set of events. The role of the framework here is to allow communication between different modules from the input to the output. After production via the physics generator (PYTHIA), particles are described in terms of their "truth" parameters (the true MC values generated): production point, initial momentum, and their species. When a particle is propagated through the detector, it will lose energy, change direction and may ultimately stop, due to the interactions with the detector material. These effects have been considered by modelling the particle's path in the detector as a "piecewise" trajectory. A helical segment is assigned to a charged particle moving inside the magnetic field volume ($\overrightarrow{B} \neq 0$), neutral particles and charged particles outside the magnetic volume (so outside the fringe field and outside the solenoid) are represented by segments of straight line. At every point where a particle interacts with the detector element, its position and momentum are recorded. Not all the particle-detector interactions are modelled with the FastSim framework because this would require a large CPU time. A good compromise between performance and accuracy can be achieved when only a limited number of interaction processes are modelled (categories). The categories considered are the following: *normal* charged particle *interactions* (energy loss, direction scattering), *EM interactions* (pair production, Compton scattering, showering, ...), *Hadronic interactions* (nuclear scattering, showering, ...).

4.2 FastSim pre-selection

Samples of events at the charm threshold have been generated using the FastSim programme. I consider the following decay chains:

$$e^+e^- \to \Psi(3770) \to (D^0)(\overline{D}^0) \to (K^+K^-)(K^+e^-\overline{\nu}_e), \tag{4.1}$$

$$e^+e^- \to \Psi(3770) \to (D^0)(\overline{D}^0) \to (K^-e^+\nu_e)(K^+K^-), \tag{4.2}$$

$$e^+e^- \to \Psi(3770) \to (D^0)(\overline{D}^0) \to (\pi^+\pi^-)(K^+e^-\overline{\nu}_e), \tag{4.3}$$

$$e^+e^- \to \Psi(3770) \to (D^0)(\overline{D}^0) \to (K^-e^+\nu_e)(\pi^+\pi^-), \tag{4.4}$$

because, as discussed in Chapter 2, these modes allow one to measure ϕ_{MIX} and can be used to constrain $\beta_{c,eff}$. Here the aim of the study is to use FastSim to estimate the effect of detector resolution on the proper time distribution (as shown in Chapter 3 when looking at Fig. 3.9). In the FastSim environment it is possible to select candidates on the basis of the criteria defined in so-called Standard Lists. Standard Lists are created during reconstruction and contain all the available information about particles. Lists and selection rules applied to the different decay channels are given in Table 4.1[2]. The requirement *GoodTracksLoose* (GTL) is used to select charged

Table 4.1: Selection constraints applied to generated Monte Carlo data samples at the charm threshold.

Constraints/Selectors	$D^0 \to K^-e^+\nu_e$	$D^0 \to \pi^+\pi^-$	$D^0 \to K^+K^-$
daughterListNames	GoodTracksLoose	ChargedTracks	GoodTracksLoose
daughterListNames	GoodTracksLoose	ChargedTracks	GoodTracksLoose
preFitSelectors	X	M_{pdg}±0.04 (GeV)	M_{pdg}±0.04 (GeV)
FitConstraints	Beam spot	Beam spot	Beam spot
FittingAlgorithm	TreeFitter	TreeFitter	TreeFitter
fillMC	True	True	True

tracks having a minimum transverse momentum of 0.1 GeV, at least twelve hits in the drift chamber, and which pass within 10 cm of the beamspot in z and 1.5 cm from the beamspot in the x-y plane. *ChargedTracks* selects candidates with non-zero charge and pion mass hypothesis assigned. Since the *preFitSelector* consists of a selection rule based on properties of a given particle, it is used to save CPU time. As a *preFitSelector* we have considered the mass and this has been applied only to the hadronic decay channel, due to the fact that in the semileptonic decay the missing neutrino does not allow one to properly reconstruct the D^0 mass. *FitConstraints* defines some additional constraints to apply to the reconstruction of a decay chain: both

[2]The same constraints shown for $D^0 \to K^-e^+\nu_e$ have been applied in the charged conjugate final states $\overline{D}^0 \to K^+e^-\overline{\nu}_e$.

the D^0 mesons have been required to originate from the beamspot. The full decay chain has been reconstructed and fitted with a χ^2 algorithm depending on the particles' decay vertices, momenta and flight length, called $TreeFitter$ [40]. Data are then written to a ROOT file which contains also the MC truth information.

4.3 Analysis general procedure

In this section I describe the general procedure used to reconstruct the signal of interest and to study the proper time resolution using $D^0/\overline{D}^0 \to h^+h^-$ ($h = K, \pi$) and $D^0 \to K^-e^+\nu_e/\overline{D}^0 \to K^+e^-\overline{\nu}_e$.

4.3.1 Mass reconstruction

D^0 mesons are reconstructed by combining the four-momenta of their decay products. In particular the detected tracks are used to reconstruct the invariant mass with the two-body invariant mass formula:

$$M_{12} = \sqrt{m_0^{(1)2} + m_0^{(2)2} + 2\left(\frac{1}{c^4}E_1E_2 - \frac{1}{c^2}\overrightarrow{p_1}\overrightarrow{p_2}\right)}, \tag{4.5}$$

where $m_0^{(1)}$ and $m_0^{(2)}$ are the invariant masses of the two decay products of the D^0 ($\overline{D}^0$) meson, E_1 and E_2 their energy, and $\overrightarrow{p_1}$ and $\overrightarrow{p_2}$ their momenta. Reconstructed $\overline{D}^0$ meson decays like the processes $D^0(\overline{D}^0) \to \pi^+\pi^-$ or $D^0(\overline{D}^0) \to K^+K^-$ are fully reconstructed decays (as one can see in Fig. 4.1 where the invariant mass of the K^+K^- pairs shows a peaky structure with mean corresponding exactly to the expected D^0 mass). The reconstruction of the semi-leptonic tag side is complicated by the presence of the neutrino, due to the fact that it escapes the detector: for this reason when trying to reconstruct the invariant mass of the $K^{-(+)}e^{+(-)}$ pairs one would obtain a beta decay spectrum of the D^0 meson as shown in Fig. 4.2. Considering the fact that the energy of the collisions at the interaction point is known, one can use this information to reconstruct, on an event-by-event basis, the missing energy and the missing momentum of the neutrino (subtracting the energy and momentum of the reconstructed $\Psi(3770)$ from the total energy

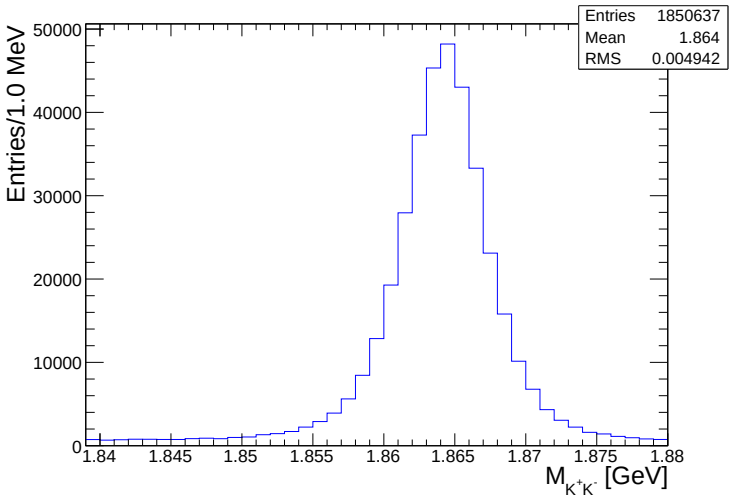

Figure 4.1: Invariant mass $M_{K^+K^-}$ for $D^0 \to K^+K^-$.

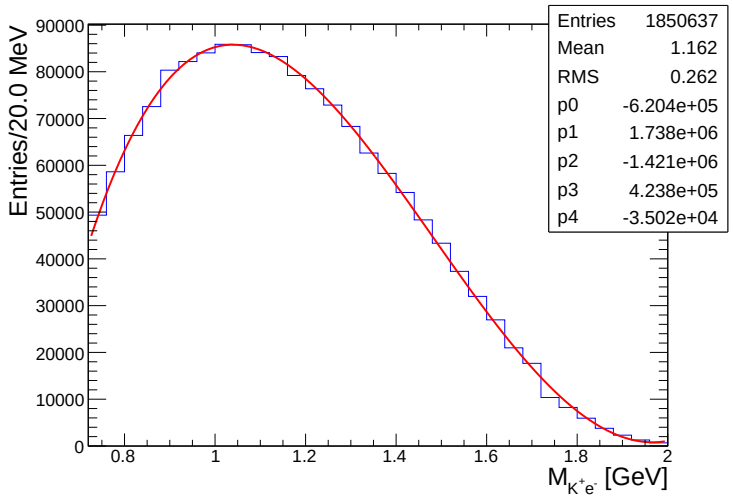

Figure 4.2: Invariant mass M_{Ke} for $\overline{D}^0 \to K^+e^-\overline{\nu}_e$ fitted with a 4^{th} order polynomial function.

at the interaction point) as shown in Eq. (4.6) and in Eq. (4.7)

$$E_{miss} = E_B - E_{tr}, \tag{4.6}$$

$$\overrightarrow{P}_{miss} = \overrightarrow{P}_B - \overrightarrow{P}_{tr}, \tag{4.7}$$

where E_B and P_B are the total energy and momentum of the beams at the interaction point, and E_{tr} and P_{tr} are the measured energy and momentum of the detected tracks. This information is then used to evaluate the neutrino missing mass as a consistency check of the signal reconstruction: it has to be a distribution peaked at zero, see Fig. 4.3. Figure 4.4 shows the effect of adding

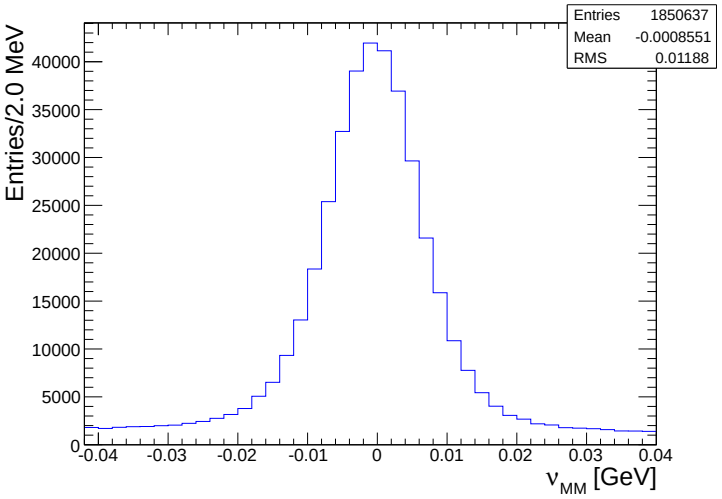

Figure 4.3: Missing mass of the $\overline{\nu}_e$.

the missing energy to the invariant mass of the semileptonically decayed D^0 used for tagging (SLT), where a peaking structure with mean corresponding to the expected mass of the D^0 meson is observed. The resulting four-momenta associated with the D^0 mesons are then combined to obtain the $\Psi(3770)$ mass which is shown in Fig. 4.5.

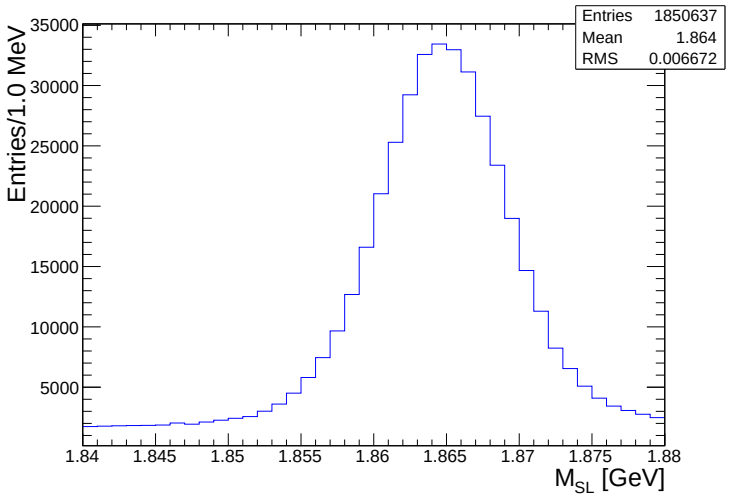

Figure 4.4: D^0 meson invariant mass evaluated using the Ke system combined with the information on the missing energy in the decay $\overline{D}^0 \to K^+e^-\overline{\nu}_e$.

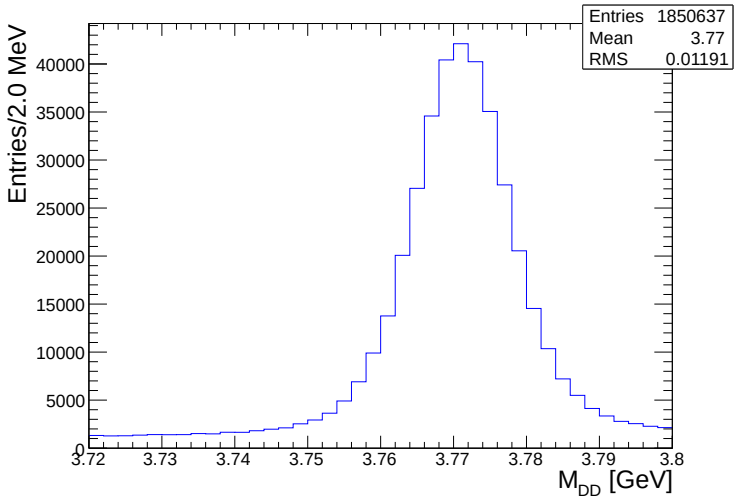

Figure 4.5: $\Psi(3770)$ invariant mass evaluated by combining the four momenta of the reconstructed $D^0/\overline{D}^0$ mesons, taking into account the missing energy associated with the semileptonically decayed $\overline{D}^0$ mesons used for tagging (SLT).

4.3.2 Vertex and Δt resolution

The resolution on the decay vertex position (only z direction, due to the boost) was calculated as a difference between the reconstructed vertex and the MC generated vertex, $\Delta z = z_{rec}^{TAG,CP} - z_{true}^{TAG,CP}$, and it is shown in Fig. 4.6 for the CP side of an event. The resolution on Δz is evaluated as a difference between the resolution on the fully reconstructed CP side z-vertex and the resolution on the z-vertex evaluated for the tag side. Since it is possible to use the approximation: $\Delta t \approx \Delta z / \beta\gamma c$, one can then obtain the resolution on Δt, the resolution on Δt is shown in Fig. 4.7. Before obtaining a final

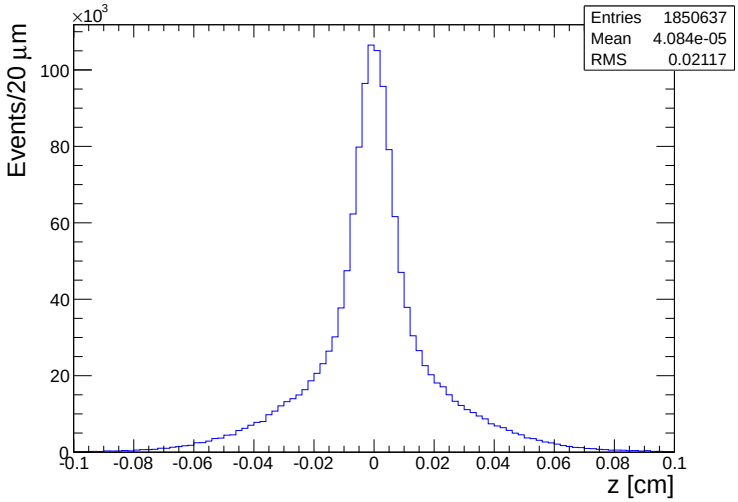

Figure 4.6: Resolution on the z-coordinate of the decay vertex of the CP side D^0 mesons.

distribution for the observed resolution one needs to require some constraints. The first one, expressing the *goodness* of the vertex reconstruction, is the χ^2 of the vertex, the second quantity, $\sigma_{\Delta t}$ is an additional variable that has to be evaluated on an event-by-event basis and that shows the error on the Δt distribution itself.

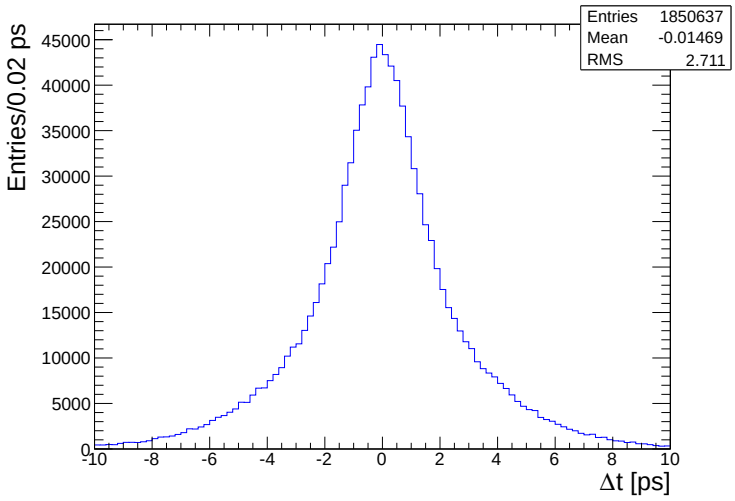

Figure 4.7: Resolution on the quantity Δt.

4.3.3 Selection Criteria

Two very good kinematic variables to reject mis-reconstructed events are the beam constrained mass (M_{BC}) and ΔE, defined as:

$$M_{BC} = \sqrt{E_{1/2}^2/c^4 - \overrightarrow{p}_D^{\,2}/c^2}, \tag{4.8}$$

and

$$\Delta E = E_D - E_{1/2}, \tag{4.9}$$

where $E_{1/2}$ represents half of the total beam energy in the center of mass system, E_D and and $\overrightarrow{p}_D$ are the total energy and momentum of the D^0 candidate evaluated in the centre-of-mass reference frame. A correlation plot of the two variables M_{BC} and ΔE is shown in Fig. 4.8. For correctly reconstructed D^0 mesons one would expect to observe an M_{BC} distribution with a peak at a mass equivalent to that of a D^0 meson and a ΔE distribution with mean at zero. I have used M_{BC} and ΔE as the main parameters to reject mis-reconstructed events selecting the appropriate 2-d region from Fig. 4.8 for each of the studied decays. Another quantity I used to reject mis-reconstructed events is the χ^2 vertex that defines the χ^2 value for the

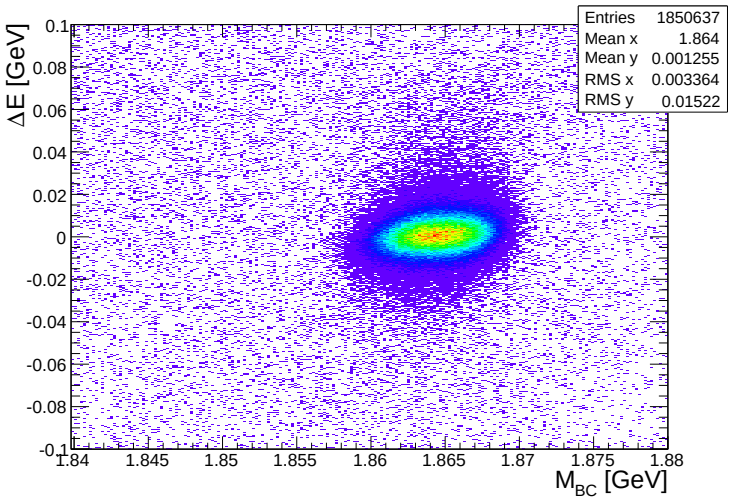

Figure 4.8: Correlation plot for M_{BC} and ΔE.

reconstructed vertexes: this requirement ensures that particles have to originate from the same vertex. The vertex χ^2 distribution is shown in Fig. 4.9. Two additional quantities to be studied are the parameters $\sigma_{\Delta t}$ evaluated in ps on an event-by-event basis and shown in Fig. 4.10, and the quantity $\delta t = \Delta t - \Delta t_{true}$[3], where the rms of δt is also called rms of the residual and is evaluated in ps. The correlation between Δt and $\sigma_{\Delta t}$ is shown in Fig. 4.11.

4.4 Δt resolution

One can make a rough initial estimate of the sensitivity of a time-dependent analysis using a Gaussian resolution function with a mean of zero and an rms corresponding to the width of the Δt distribution obtained from simulation, however a full analysis would require one to parametrise the resolution function either considering the individual effects contributing to it, or by allowing sufficient flexibility in the distribution to accommodate those effects.

[3]The quantity δt being defined as the difference on an event-by-event basis between the observed Δt and the true generated Δt_{true} is clearly only accessible in Monte Carlo studies

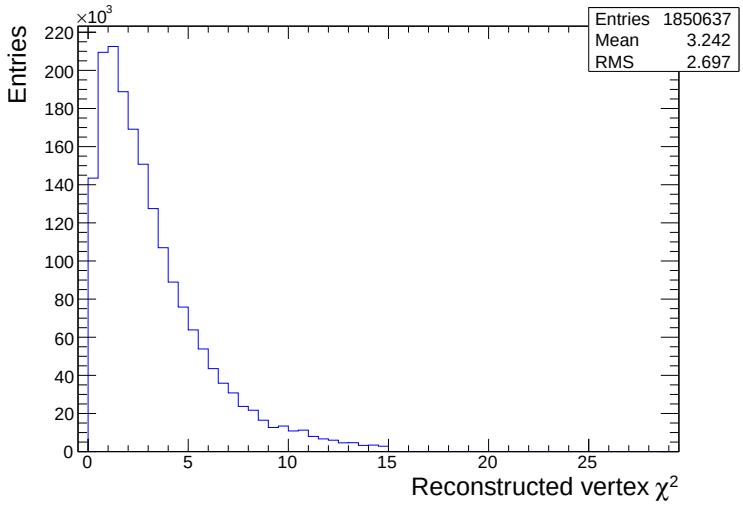

Figure 4.9: χ^2 distribution for the reconstructed vertex.

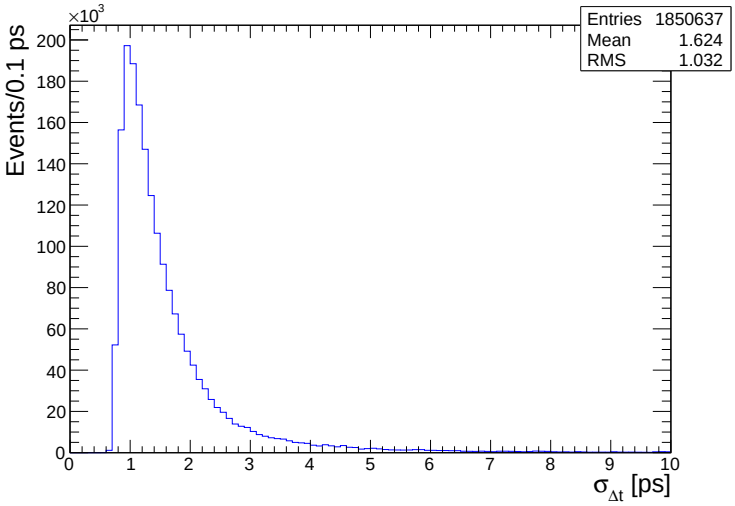

Figure 4.10: Uncertainty on Δt evaluated on an event-by-event basis, $\sigma_{\Delta t}$.

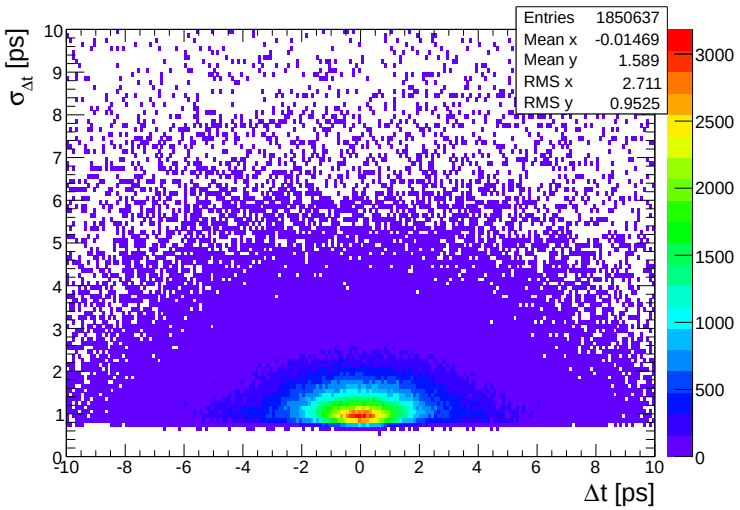

Figure 4.11: Correlation plot for Δt with respect to $\sigma_{\Delta t}$.

I performed a check on the rms and mean values of the δt distribution as a function of $\sigma_{\Delta t}$. These are shown in Fig. 4.12 and in Fig. 4.13, respectively. The linear correlation observed in the first few D^0 meson lifetimes between the δt rms and $\sigma_{\Delta t}$ is a general behaviour observed in all the decay chains under study. In particular, as shown in Fig. 4.12, the linear correlation between the two parameters observed in the region for $\sigma_{\Delta t} < 1.7 ps$ indicates that $\sigma_{\Delta t}$ represents a good parameter to measure the time resolution, however this quantity has to be corrected by appropriate scaling factors. The behaviour in the region $\sigma_{\Delta t} > 1.7$ ps is not completely understood and might influence the results shown thereafter. Finally we evaluated the possibility that the results may be biased. In order to do this, the mean of $\delta t = \Delta t - \Delta t_{true}$ (mean of residual evaluated in ps) was considered and the correlation between this parameter and $\sigma_{\Delta t}$ studied. The result is shown in Fig. 4.13, where one can see there is no significant bias on δt as a function of the per event error (the fit shown is done using a first order polynomial function $P_0(ps) = 0.003 \pm 0.002$, which is consistent with zero within 1.5 standard deviations).

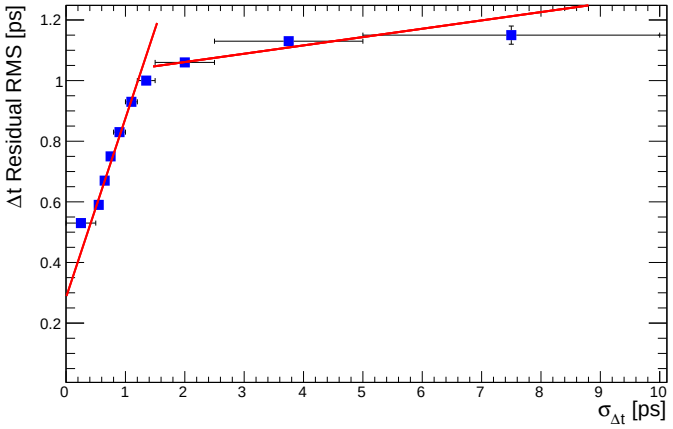

Figure 4.12: δt distribution rms as a function of the estimated event-by-event uncertainty on Δt.

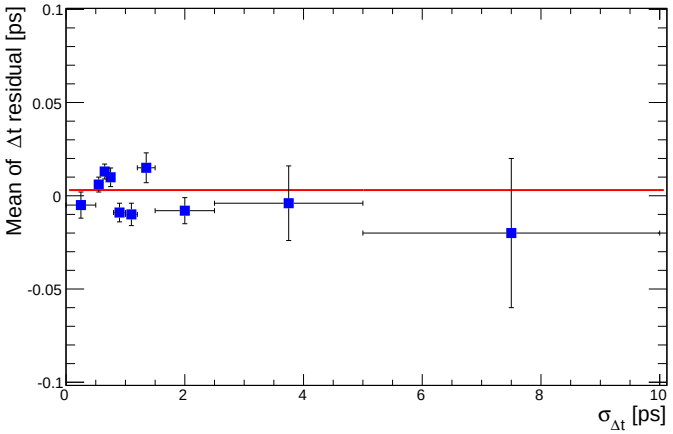

Figure 4.13: Mean of the δt distribution as a function of the estimated event-by-event uncertainty on Δt.

4.5 RooFit study of the resolution function

Detection effects, due to the finite resolution of the detector itself when reconstructing signals and vertices in particular, need to be accounted for in a time-dependent analysis. This parametrisation is done in terms of a resolution function obtained via the sum of two Gaussian functions, the *core* and the *tail* Gaussian, which account for all the events in the Δt distribution[4]. I have considered the following function for the resolution:

$$R(\delta t, \sigma_{\Delta t}) = f_c G_c(\delta t, \sigma_{\Delta t}) + (1 - f_c) G_t(\delta t, \sigma_{\Delta t}), \tag{4.10}$$

where f_c represents the core signal fraction, G_c the core Gaussian function which describes the event with $\sigma_{\Delta t} < 1.7$ ps and G_t and σ_t refers to the Gaussian function used to describe the tail of the Δt distribution that is the events with $\sigma_{\Delta t} > 1.7$ ps. The factor of $\sigma_{\Delta t}$ is common to both Gaussians and appears multiplied by a dimensionless scale factor $S_{c,t}$. This is justified by the linear relationship observed in Figure 4.12 between $\sigma_{\Delta t}$ and the RMS value of the Δt residual for low values of the per-event error and follows the logic underpinning the equivalent resolution function used for time-dependent B meson analyses on BaBar; see for example Eq. (22) as given in [41] and Eq. (6) as given in [42]. If one defines f_c (f_t) the core (tail) signal fraction, S_c (S_t) a scaling factor, and μ_c (μ_t) the mean of core (tail) Gaussian function, then Eq. (4.10) can be written as

$$R(\delta t, \sigma_{\Delta t}) = \frac{1}{\sqrt{2}\pi} \left[\frac{f_c}{S_c \sigma_{\Delta t}} e^{-\frac{(\delta_t - \mu_c \sigma_{\Delta t})^2}{2(S_c \sigma_{\Delta t})^2}} + \frac{1 - f_c}{S_t \sigma_{\Delta t}} e^{-\frac{(\delta_t - \mu_t \sigma_{\Delta t})^2}{2(S_t \sigma_{\Delta t})^2}} \right]. \tag{4.11}$$

The resolution function given in Eq. (4.11) has been adopted as a RooFit model, and a Monte Carlo study based on the expected yields at Super$B$ to

[4]The *BABAR* Collaboration, when performing time-dependent tests of CP violation in B mesons, has considered a third *outlier* Gaussian components in the resolution function to account for the $\approx 1\%$ of events at large Δt (width fixed at 8 *ps*). This represents a possibility also for D^0 decays, however due to the smaller lifetime of a D^0 meson when compared to that of a B^0 meson and looking at the time distribution of events I noticed that all the events can be accounted for by using only two Gaussian functions, this decision not only allows one to account for all the events with a simpler description of the resolution function, but more importantly it allows one to perform a more efficient analysis in terms of required CPU.

validate the model and extract the expected sensitivity on $\phi_{KK} = arg(\lambda_f(D^0 \to K^+K^-))$ and $\phi_{\pi\pi} = arg(\lambda_f(D^0 \to \pi^+\pi^-))$ performed; the results of these studies are presented in the next chapter.

Chapter 5

Time-dependent study

5.1 Decays to flavour eigenstates h^+h^- ($h = K, \pi$)

The full decay chains

$$e^+e^- \to \Psi(3770) \to (D^0)(\overline{D}^0) \to (K^+K^-)(K^+e^-\overline{\nu}_e)$$

and

$$e^+e^- \to \Psi(3770) \to (\overline{D}^0)(D^0) \to (\pi^+\pi^-)(K^-e^+\nu_e)$$

have been studied following the strategy described in the previous chapter and the obtained distributions of the discriminating variables together with a RooFit study of the resolution function and the obtained sensitivity on $arg(\lambda_f)$ are given in this chapter. The charged conjugate decay chains

$$e^+e^- \to \Psi(3770) \to (D^0)(\overline{D}^0) \to (K^-e^+\nu_e)(K^+K^-)$$

and

$$e^+e^- \to \Psi(3770) \to (\overline{D}^0)(D^0) \to (K^+e^+\nu_e)(\pi^+\pi^-)$$

have also been studied following the same procedure and the obtained distributions of the discriminating variables together with a RooFit study of the resolution function and the obtained sensitivity on $arg(\lambda_f)$ will be given in Appendix A and Appendix B, respectively. I generated 500000 events for the decay chain involving the $D^0 \to K^+K^-$ decay, and 200000 events for the decay chain containing the $\overline{D}^0 \to \pi^+\pi^-$ decay assuming a boost factor $\beta\gamma = 0.28$. In the Super$B$ framework, with an instantaneous luminosity $L = 10^{35} cm^{-2}s^{-1}$ when running at the charm threshold ($L = 10^{36} cm^{-2}s^{-1}$ when running at the $\Upsilon(4S)$), the generated data samples would correspond to an integrated luminosity of 609 fb^{-1} for $D^0 \to K^+K^-$ and 632.9 fb^{-1} for $\overline{D}^0 \to \pi^+\pi^-$ when using the semileptonic $D^0(\overline{D}^0) \to K^{-(+)}e^{+(-)}\nu_e(\overline{\nu}_e)$ for tagging. Such an integrated luminosity was expected to be collected in a few months. Here I only consider the $Ke\nu$ tagged decays, and not the semileptonic decays with a muon in the final state or K^* tagged events, so when comparing the number of generated events presented here with the more general case discussed in Sec. 2.7 there is a factor of 3.09 difference in the rates expected naively between the assumed yields at the start of the thesis to the sub-modes that are studied here. For mis-reconstructed event rejection I applied the selection criteria shown in Tab. 5.1 and Tab. 5.2 for the $D^0 \to K^+K^-(\overline{D}^0 \to K^+e^-\overline{\nu}_e)$ and $\overline{D}^0 \to \pi^+\pi^-(D^0 \to K^-e^+\nu_e)$ chains, respectively. It is very important here to notice that the analysed data samples are background-free, due to the fact that I have simulated only the decay chains of interest with fast simulation. A natural step forward for this analysis, including the study of the sensitivity to $arg[\lambda_f]$, would require an effort to generate data with full simulation and generating not only the two (four) decay chains of interest but to generate a data sample which contains all the decays of the $\Psi(3770)$ resonance plus all the promptly produced D^0 mesons from e^+e^- collisions. It should be noted however that the decay chains of interest have been cleanly isolated by the CLEO experiment [29], so inclusion of backgrounds in this study are expected to be a second order effect.

Distributions of discriminating variables after applying the selection criteria given in Tab. 5.1 and in Tab. 5.2 are shown in Fig. 5.1 for $D^0 \to K^+K^-(\overline{D}^0 \to K^+e^-\overline{\nu}_e)$ and in Fig. 5.2 for $\overline{D}^0 \to \pi^+\pi^-(D^0 \to K^-e^+\nu_e)$, where the obtained masses for D^0, $\overline{D}^0$ and $\Psi(3770)$, and the resolutions on Δt and Δz have been

Table 5.1: Allowed values for ΔE, M_{BC}, $\sigma_{\Delta t}$ and χ^2 for the decay chain $e^+e^- \to \Psi(3770) \to (D^0)(\overline{D}^0) \to (K^+K^-)(K^-e^+\nu_e)$.

Parameter	min.	max.
ΔE [GeV]	-0.01	0.01
M_{BC} [GeV]	1.8605	1868
$\sigma_{\Delta t}$ [ps]	-	10.0
χ^2	-	15

Table 5.2: Allowed values for ΔE, M_{BC}, $\sigma_{\Delta t}$ and χ^2 for the decay chain $e^+e^- \to \Psi(3770) \to (\overline{D}^0)(D^0) \to (\pi^+\pi^-)(K^-e^+\nu_e)$.

Parameter	min.	max.
ΔE [GeV]	-0.01	0.008
M_{BC} [GeV]	1.862	1867
$\sigma_{\Delta t}$ [ps]	-	10.0
χ^2	-	15

fitted with a central Gaussian function plus a secondary function as shown in Tab. 5.3 and Tab. 5.4, where $Gaus_1$ and $Gaus_2$ refer to the central and secondary Gaussian functions used in the fit, respectively, and pol_1 refers to a 1^{st} order polynomial function.

After selection criteria have been applied I have been able to reconstruct 105927 $\overline{D}^0 \to \pi^+\pi^-$ and 269246 $D^0 \to K^+K^-$ events, equivalent to an efficiency $\epsilon_{\pi^+\pi^-} = 52.9\%$ for $\overline{D}^0 \to \pi^+\pi^-$ and $\epsilon_{KK} = 53.8\%$ for $D^0 \to K^+K^-$. Additional information with respect to that shown in Fig. 5.1 is required to evaluate the Δt resolution function and to use this to constrain $\phi = arg[\lambda_f]$. This is contained in the correlation plot between Δt and $\sigma_{\Delta t}$ discussed in the previous chapter (see Fig.4.11). Figure 5.3 shows the correlation plots between Δt and $\sigma_{\Delta t}$ after the selection criteria given in Tab. 5.1 and in Tab. 5.2 have been applied to (left) $e^+e^- \to Psi(3770) \to (D^0)(\overline{D}^0) \to (K^+K^-)(K^+e^-\overline{\nu}_e)$ and to (right) $e^+e^- \to \Psi(3770) \to (\overline{D}^0)(D^0) \to (\pi^+\pi^-)$

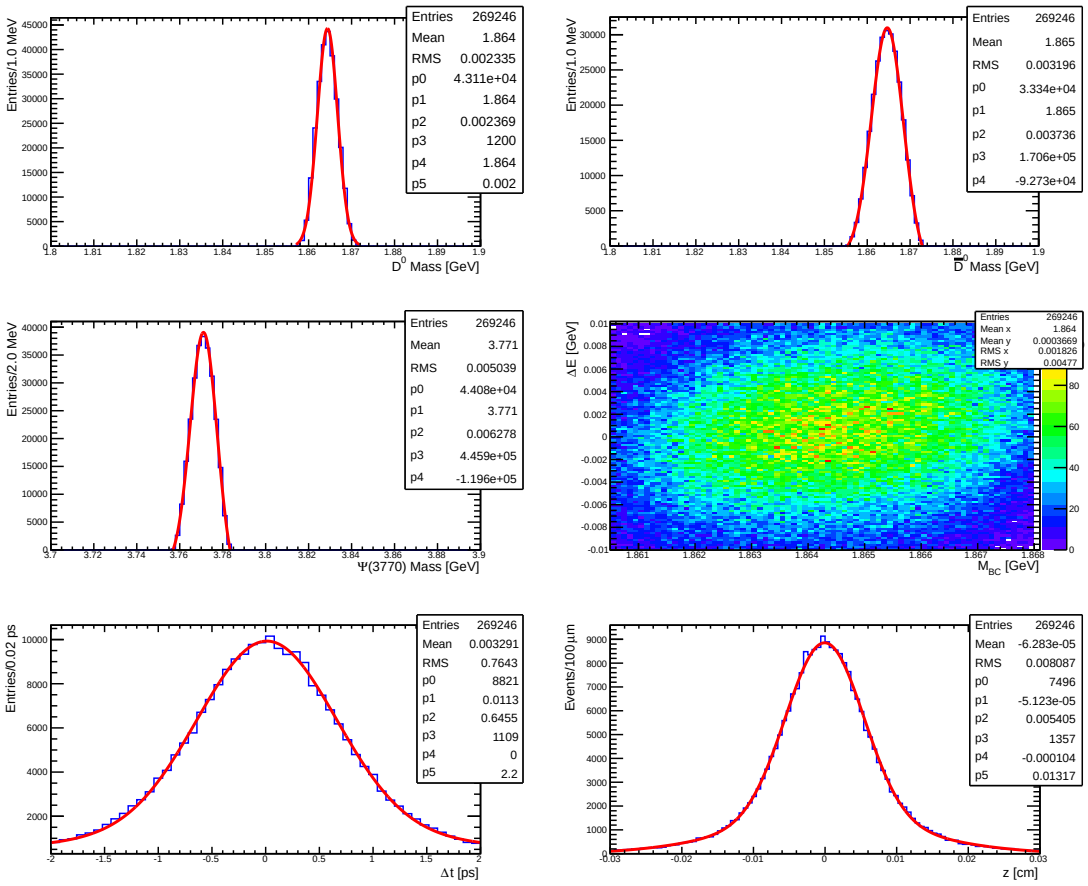

Figure 5.1: Final distributions obtained after selection criteria have been applied to the 500000 generated events $e^+e^- \to \Psi(3770) \to (D^0)(\overline{D}^0) \to (K^+K^-)(K^+e^-\overline{\nu}_e)$. D^0 mass (top left), $\overline{D}^0$ mass (top left), $\Psi(3770)$ Mass (centre left), ΔE vs. M_{BC} correlation plot (centre right), Δt distribution (bottom left), Δz distribution (bottom right).

$(K^-e^+\nu_e)$, respectively.

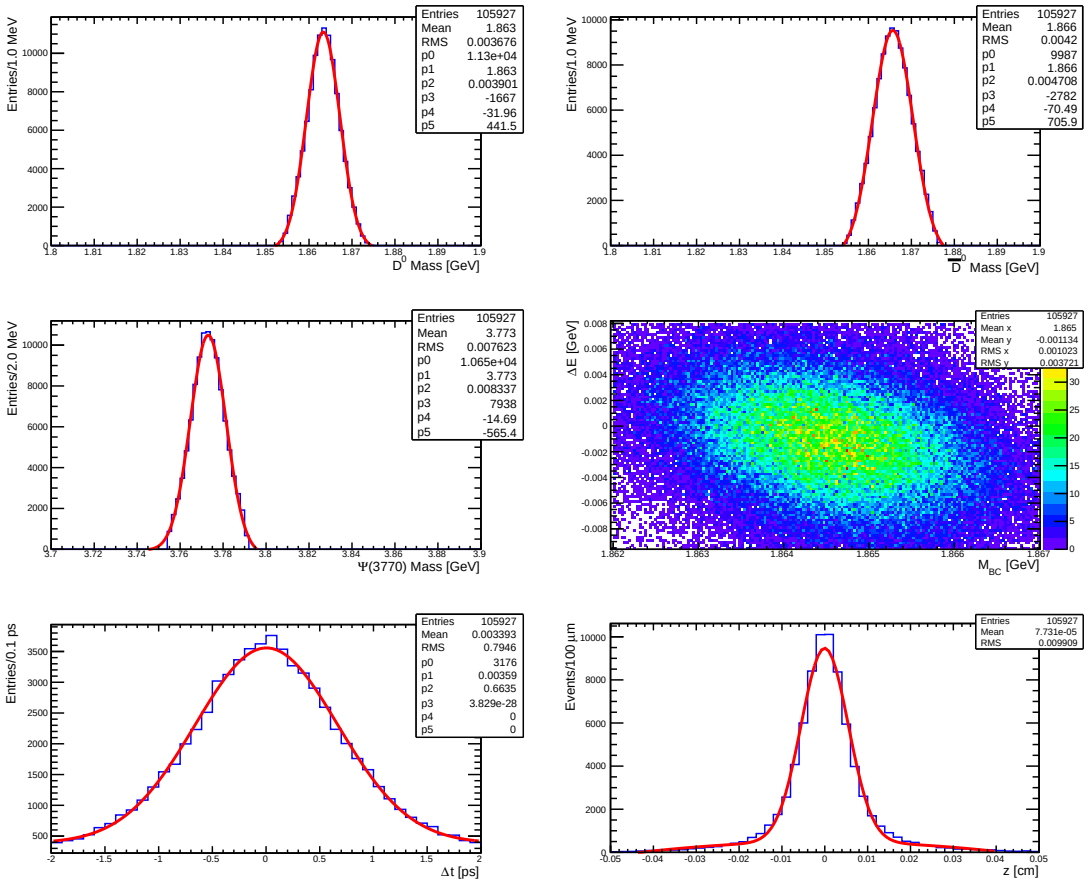

Figure 5.2: Final distributions obtained after selection criteria have been applied to the 200000 generated events $e^+e^- \to \Psi(3770) \to (\overline{D}^0)(D^0) \to (\pi^+\pi^-)(K^-e^+\nu_e)$. $\overline{D}^0$ mass (top left), D^0 mass (top left), $\Psi(3770)$ Mass (centre left), ΔE vs. M_{BC} correlation plot (centre right), Δt distribution (bottom left), Δz distribution (bottom right).

Table 5.3: Values of the mean (μ), standard deviation (σ) and the fraction of events in the core Gaussian function f_c extracted from the fit to the obtained mass distribution for D^0, $\overline{D}^0$ and $\Psi(3770)$, and for the obtained Δt and Δz distribution in the decay chain $e^+e^- \to \Psi(3770) \to (D^0)(\overline{D}^0) \to (K^+K^-)(K^-e^+\nu_e)$ after the selection criteria shown in Tab. 5.1 have been applied. $Gaus_1$ and $Gaus_2$ represent a central and a secondary Gaussian function and pol_1 is a 1^{st} order polynomial function.

Variable	Functions	$Gaus_1$	f_c
D^0 Mass	$Gaus_1$+$Gaus_2$	$\mu = 1.864$ GeV, $\sigma = 0.0024$ GeV	0.81
$\overline{D}^0$ Mass	$Gaus_1$+pol_1	$\mu = 1.865$ GeV, $\sigma = 0.0037$ GeV	-
$\Psi(3770)$ Mass	$Gaus_1$+pol_1	$\mu = 3.771$ GeV, $\sigma = 0.0063$ GeV	-
Δt	$Gaus_1$+$Gaus_2$	$\mu = 0.01$ ps, $\sigma = 0.065$ ps	0.86
Δz	$Gaus_1$+$Gaus_2$	$\mu = 0.5$ μm, $\sigma = 54.0$ μm	0.87

Table 5.4: Values of the mean (μ) and standard deviation (σ) extracted from the fit to the obtained mass distribution for D^0, $\overline{D}^0$ and $\Psi(3770)$, and for the obtained Δt and Δz distribution in the decay chain $e^+e^- \to \Psi(3770) \to (\overline{D}^0)(D^0) \to (\pi^+\pi^-)(K^-e^+\nu_e)$ after the selection criteria shown in Tab. 5.2 have been applied. $Gaus_1$ and $Gaus_2$ represent a central and a secondary Gaussian function and pol_1 is a 1^{st} order polynomial function.

Variable	Functions	$Gaus_1$	f_c
D^0 Mass	$Gaus_1$+pol_1	$\mu = 1.866$ GeV, $\sigma = 0.0042$ GeV	-
$\overline{D}^0$ Mass	$Gaus_1$	$\mu = 1.8635$ GeV, $\sigma = 0.0036$ GeV	-
$\Psi(3770)$ Mass	$Gaus_1$+pol_1	$\mu = 3.773\ GeV$, $\sigma = 0.0083$ GeV	-
Δt	$Gaus_1$+$Gaus_2$	$\mu = 0.0$ ps, $\sigma = 0.063$ ps	0.87
Δz	$Gaus_1$+$Gaus_2$	$\mu = 0.0$ μm, $\sigma = 46.0$ μm	0.89

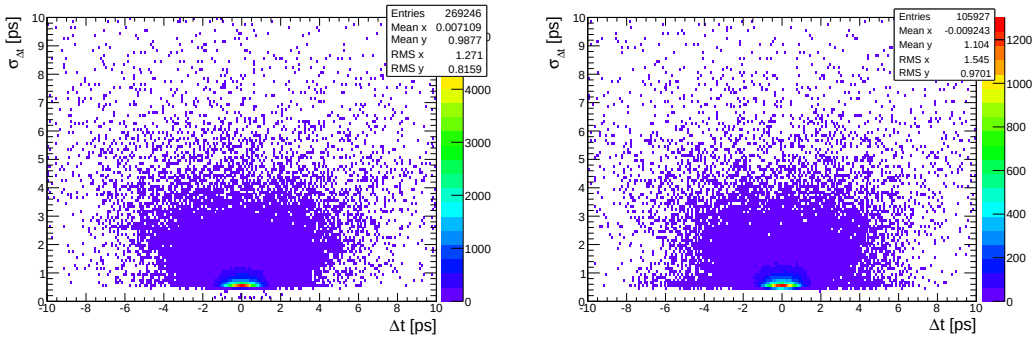

Figure 5.3: Correlation plots for Δt and $\sigma_{\Delta t}$ after the selection criteria given in Tab. 5.1 and in Tab. 5.2 have been applied to the decay chains (left) $e^+e^- \to \Psi(3770) \to (D^0)(\overline{D}^0) \to (K^+K^-)(K^+e^-\overline{\nu}_e)$, and (right) $e^+e^- \to \Psi(3770) \to (\overline{D}^0)(D^0) \to (\pi^+\pi^-)(K^-e^+\nu_e)$.

5.2 Toy studies: constraints on $\phi = arg[\lambda_f]$

As described in the previous chapter, I performed a RooFit study of the resolution function. The resolution function obtained by the sum of two Gaussian functions, one to include the core of the signal and one for the tail events as described in Sec. 4.5, is shown in Fig. 5.4 for $e^+e^- \to \Psi(3770) \to (D^0)(\overline{D}^0) \to (K^+K^-)(K^+e^-\overline{\nu}_e)$ and in Fig. 5.5 for $e^+e^- \to \Psi(3770) \to (\overline{D}^0)(D^0) \to (\pi^+\pi^-)(K^-e^+\nu_e)$.

The RooFit study, performed in two subsequent steps, is performed as follows. In the first step, the resolution function parameters are determined from the resolution probability density function (rPDF), a sample of 200 Monte Carlo "toys" (or simulated experiments) is generated according to the obtained rPDF and for each of the parameters involved in the rPDF I study the distributions of the mean value, the associated distribution of the error(s), and I study the distribution of the pulls of the errors. The study of the distribution of the pulls of the errors is adopted in Monte Carlo studies to test the reliability of the fit in terms of extracting the correct resolution function parameters; this distribution, defined as $\Delta_{pull} = (x_f - x_g)/\sigma$ where x_f represents the value of the parameter x extracted from the fit, x_g is the generated value of the parameter x and σ is the uncertainty on x_f extracted from the fit. Δ_{pull} contains very important information about the nature of the errors observed, in fact one would expect the Δ_{pull} distribution to be a Gaussian distribution with mean at zero and standard deviation equal to one if the fit can extract an unbiased estimate of x, and reproduce the uncertainty on x correctly. If the mean of Δ_{pull} is different from zero then the measurement is biased, if the standard deviation of Δ_{pull} is larger than one then the errors are underestimated, and if the standard deviation of Δ_{pull} is smaller than one then the errors are overestimated.

The second step consists of a maximum likelihood fit to the time-dependence according to Eq. (2.46), and shown in Fig. 2.6 including the resolution effects of the detector, described by the resolution function rPDF. This is obtained by fitting the function obtained by the convolution of the expected (true) time distribution for $D^0(\overline{D}^0) \to h^+h^-$ with $h = K, \pi$ decays as given in Eq. (2.46) with the obtained resolution function as given in Eq. (4.11). The

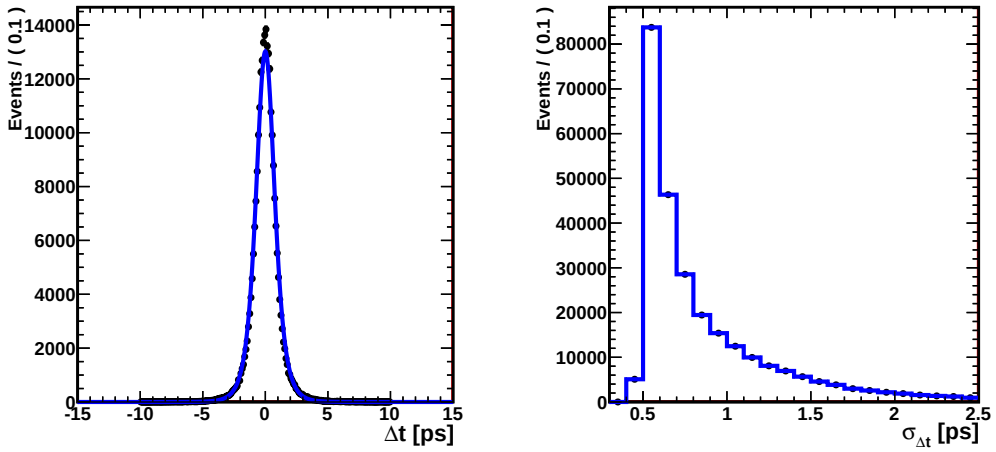

Figure 5.4: Δt resolution function for $e^+e^- \to D^0 \to K^+K^-(\overline{D}^0 \to K^+e^-\overline{\nu}_e)$ (left) and the error on Δt evaluated on an event-by-event basis, $\sigma_{\Delta t}$ (right).

values of parameters involved in Eq. (2.46) (ΔM, $\Delta\Gamma$, Γ) are fixed to the most up to date values as reported in [14] and the maximum likelihood fit can then performed in terms of $|\lambda_f|$ and $\phi = arg[\lambda_f]$. According to the results shown in Ref. [9], the value of $|\lambda_f|$ is consistent with one within one standard deviation, so I fixed its value to one in the fit, reducing computing time. Finally the maximum likelihood fit is performed in order to extract $\phi = arg[\lambda_f]$.

Central values of the various parameters involved in the fit to the resolution function are shown together with their corresponding errors and with the distribution of the pulls of the errors in Figs. 5.6-5.10 for $e^+e^- \to Psi(3770) \to (D^0)(\overline{D}^0) \to (K^+K^-)(K^+e^-\overline{\nu}_e)$ and in Figs. 5.11-5.15 for $e^+e^- \to \Psi(3770) \to (\overline{D}^0)(D^0) \to (\pi^+\pi^-)(K^-e^+\nu_e)$, respectively. A consistency check of the maximum likelihood fit was obtained performing a null test on the CP asymmetry by fitting a control sample for which no CP violation is expected (*i.e.* semileptonic D^0 decays) confirming the consistency of the model.

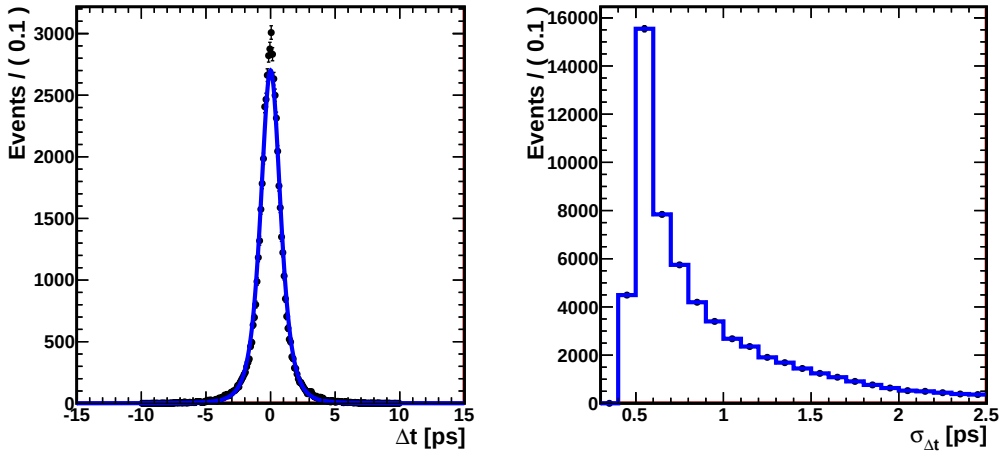

Figure 5.5: Δt resolution function for $e^+e^- \to \Psi(3770) \to (\overline{D}^0)(D^0) \to (\pi^+\pi^-)(K^-e^+\nu_e)$ (left) and the error on Δt evaluated on an event-by-event basis, $\sigma_{\Delta t}$ (right).

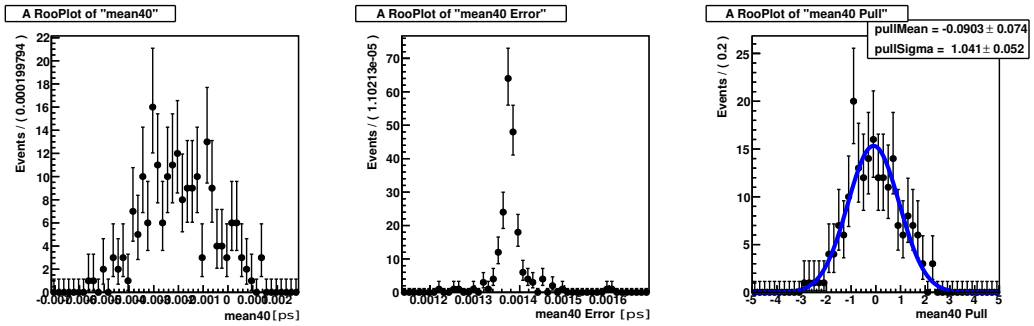

Figure 5.6: Fitted mean of the core Gaussian function (left), error on the mean (centre), and the pulls of the errors (right) for $e^+e^- \to \Psi(3770) \to (\overline{D}^0)(D^0) \to (K^+e^-\overline{\nu}_e)(K^+K^-)$.

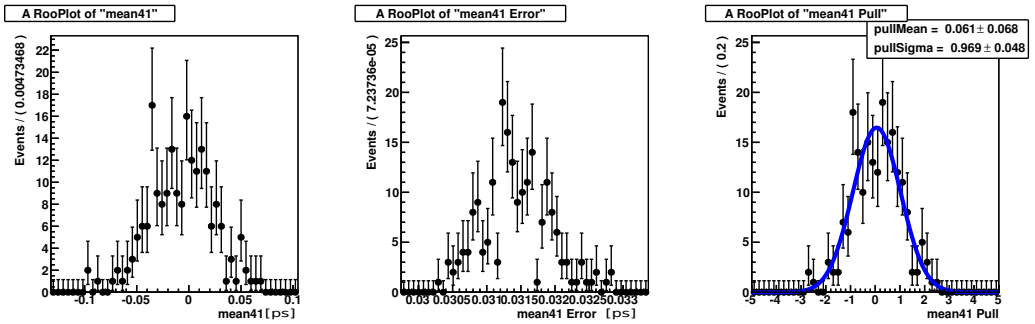

Figure 5.7: Fitted mean of the tail Gaussian function (left), error on the mean (centre), and the pulls of the errors (right) for $e^+e^- \to \Psi(3770) \to (\overline{D}^0)(D^0) \to (K^+e^-\overline{\nu}_e)(K^+K^-)$.

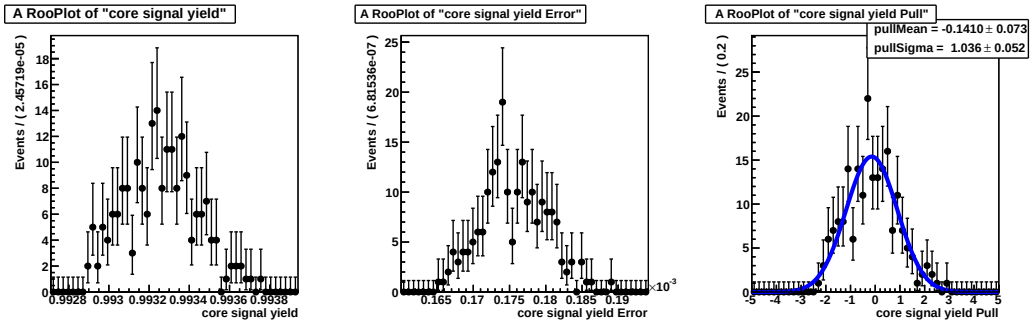

Figure 5.8: Fitted core signal fraction (left), error (centre), and the pulls of the errors (right) for $e^+e^- \to \Psi(3770) \to (\overline{D}^0)(D^0) \to (K^+e^-\overline{\nu}_e)\ (K^+K^-)$.

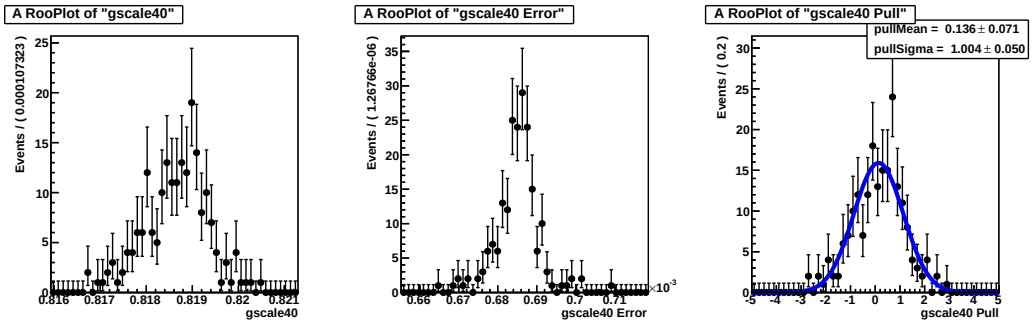

Figure 5.9: Fitted scale factor of the core Gaussian function (left), error (centre), and the pulls of the errors (right) for $e^+e^- \to \Psi(3770) \to (\overline{D}^0)(D^0) \to (K^+e^-\overline{\nu}_e)(K^+K^-)$.

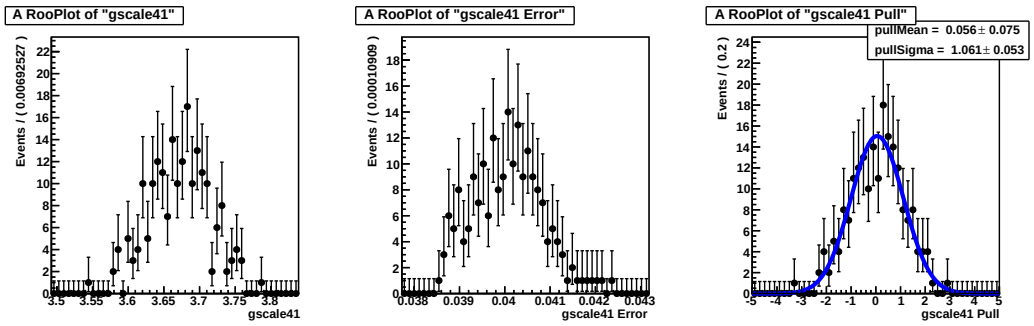

Figure 5.10: Fitted scale factor of the tail Gaussian function (left), error (centre), and the pulls of the errors (right) for $e^+e^- \to \Psi(3770) \to (\overline{D}^0)(D^0) \to (K^+e^-\overline{\nu}_e)(K^+K^-)$.

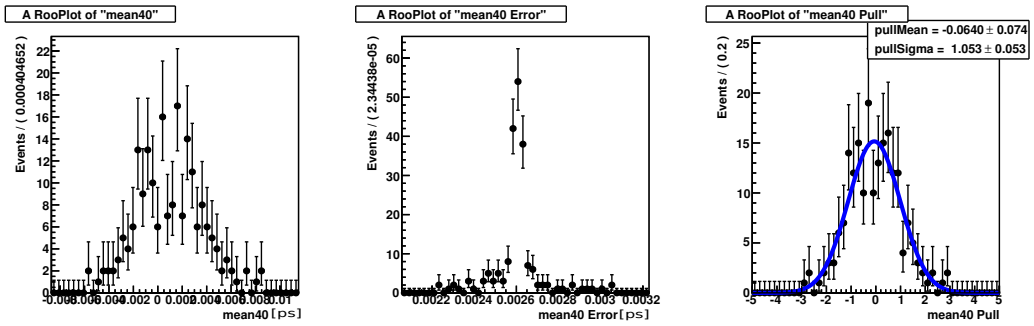

Figure 5.11: Fitted mean of the core Gaussian function (left), error on the mean (centre), and the pulls of the errors (right) for $e^+e^- \to \Psi(3770) \to (\overline{D}^0)(D^0) \to (\pi^+\pi^-)(K^-e^+\nu_e)$.

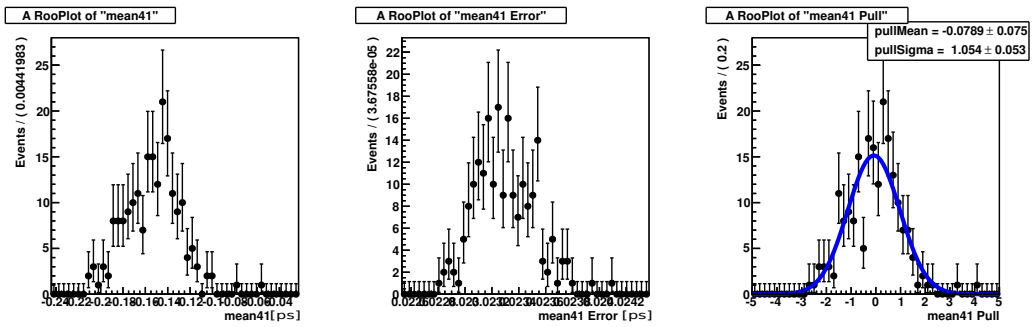

Figure 5.12: Fitted mean of the tail Gaussian function (left), error on the mean (centre), and the pulls of the errors (right) for $e^+e^- \to \Psi(3770) \to (\overline{D}^0)(D^0) \to (\pi^+\pi^-)(K^-e^+\nu_e)$.

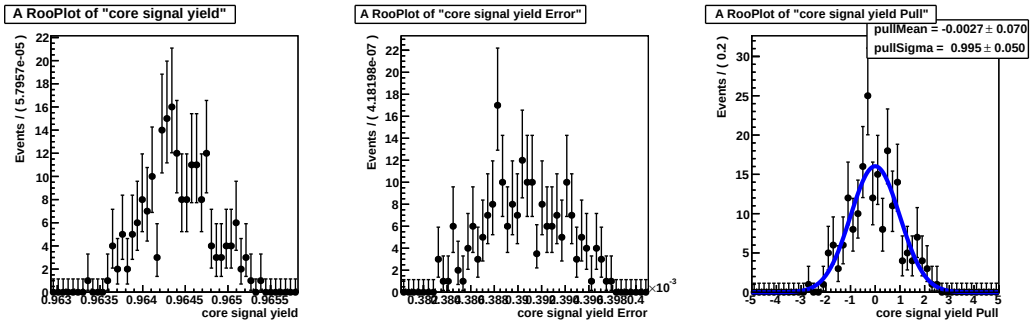

Figure 5.13: Fitted core signal fraction (left), error (centre), and the pulls of the errors (right) for $e^+e^- \to \Psi(3770) \to (\overline{D}^0)(D^0) \to (\pi^+\pi^-)\ (K^-e^+\nu_e)$.

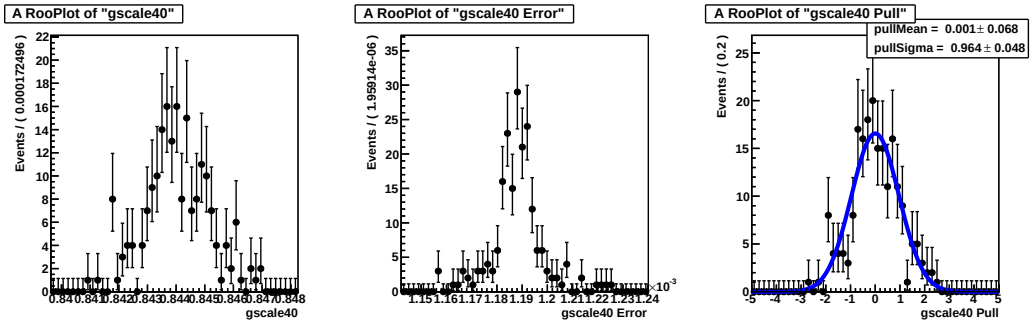

Figure 5.14: Fitted scale factor of the core Gaussian function (left), error (centre), and the pulls of the errors (right) for $e^+e^- \to \Psi(3770) \to (\overline{D}^0)(D^0) \to (\pi^+\pi^-)(K^-e^+\nu_e)$.

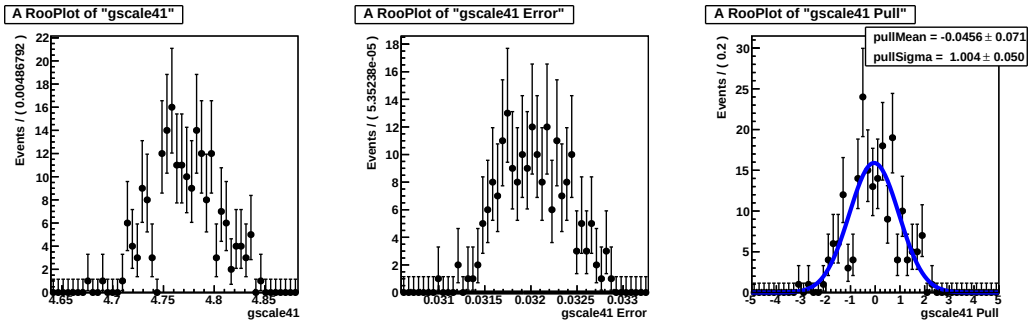

Figure 5.15: Fitted scale factor of the tail Gaussian function (left), error (centre), and the pulls of the errors (right) for $e^+e^- \to \Psi(3770) \to (\overline{D}^0)(D^0) \to (\pi^+\pi^-)(K^-e^+\nu_e)$.

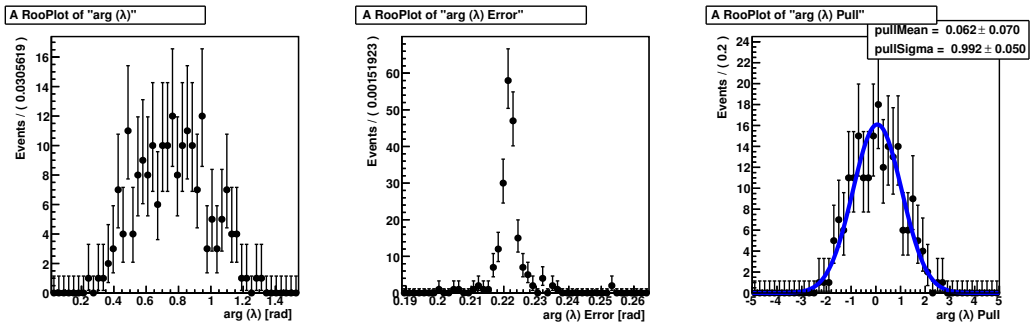

Figure 5.16: Fitted value of $\phi_{KK} = \phi_{MIX} = arg$[lambda] (left), error on ϕ_{MIX} (centre), pulls of the errors (right).

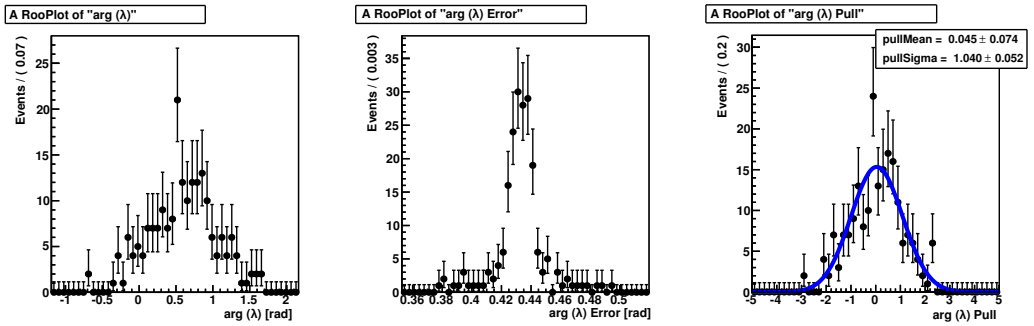

Figure 5.17: Fitted value of $\phi_{\pi\pi} = \phi_{MIX} + 2\beta_{c,eff} = arg$[lambda] (left), error on $\phi_{MIX} + 2\beta_{c,eff}$ (centre), pulls of the errors (right).

Fig. 5.16 and Fig. 5.17 show the results of the maximum likelihood fit on $\phi_{KK} = arg[\lambda_f(D^0 \to K^+K^-)] = \phi_{MIX}$ and $\phi_{\pi\pi} = arg[\lambda_f(D^0 \to \pi^+\pi^-)] = \phi_{MIX} + 2\beta_{c,eff}$ together with their errors and the pull distributions from the ensemble of toy Monte Carlo experiments, where the truth values $\phi_{KK} = 0.8$ rad and $\phi_{\pi\pi} = 0.7$ rad have been used. One can see that the sensitivity on $\phi_{KK} = \phi_{MIX}$ and on $\phi_{\pi\pi} = \phi_{MIX} + 2\beta_{c,eff}$ when 1 ab^{-1} of data is collected at the charm threshold with a boost factor $\beta\gamma = 0.28$ is $\sigma_{\phi_{KK}} = 0.22$ rad and $\sigma_{\phi_{\pi\pi}} = 0.42$ rad, respectively.

5.3 Constraints on $\beta_{c,eff}$

The results shown in the previous section for $\phi = arg[\lambda_f(D^0 \to K^+K^-)] = \phi_{MIX}$ and $\phi = arg[\lambda_f(D^0 \to \pi^+\pi^-)] = \phi_{MIX} + 2\beta_{c,eff}$ can be combined to obtain constraints on $\beta_{c,eff}$ as discussed in Sec. 2.5.3. As a result I estimate that the statistical uncertainty on $\beta_{c,eff}$ for this scenario is

$$\sigma_{\beta_{c,eff}} = 13.6^\circ. \tag{5.1}$$

Equation (5.1) has to be compared with the predicted sensitivity for 1 ab^{-1} of data collected at the charm threshold shown in Tab. 2.3, where a sensitivity of 3.3° on $\beta_{c,eff}$ was expected, highlighting the importance of accounting for detector resolution in this type of analysis. One should recall that the resolution on the vertex separation Δz, due also to the short lifetime of the D^0 mesons, depends upon the boost factor. The Super$B$ experiment is optimised for a boost factor $\beta\gamma = 0.28$ for the $\Upsilon(4S)$ programme. One can ask what would happen if a larger boost were to be used. As an example I have repeated this study for $\beta\gamma = 0.56, 0.9$, where the rms of the Δt distribution is smaller than the D^0 lifetime. This larger boost option have a slightly degraded signal efficiency, however the detector resolution is superior to that obtained for the low boost ($\beta\gamma = 0.28$) option. As shown in next sections the obtained final sensitivity on $arg[\lambda_f]$ for $D^0 \to \pi^+\pi^-$ is found to be of the order of 6.7° when $\beta\gamma = 0.9$. Hence one could achieve a precision of 3.4° for a high boost configuration with an integrated luminosity of $1ab^{-1}$. This is similar to the ideal precision attainable as outlined in Chapter 2.

5.3.1 Covariance matrices

To resolve the decay vertices of the D^0 and $\overline{D}^0$ decays and obtain a resolution on their separation which can enable one to perform time-dependent analyses, the boost factor plays a very important role as was shown in this thesis. In order to estimate the performance for different boost configurations, I have considered the two options $\beta\gamma = 0.28, 0.56, 0.9$ as previously discussed. For each of these machine configurations it is necessary to write a pair of covariance matrices which contain all relevant information on the parameters of electron and the positron beams. The beam energy and crossing angle for

the different boost configurations are listed in Table 5.5. The covariance

Table 5.5: Electron and positron beam energy and crossing angle α for the two different boost configurations $\beta\gamma = 0.28, 0.56, 0.9$ considered in this thesis.

Boost	E_{e^-} (GeV)	E_{e^+} (GeV)	α ($mrad$)
$\beta\gamma = 0.28$	-1.61	2.21	± 33
$\beta\gamma = 0.56$	-1.11	3.22	± 33
$\beta\gamma = 0.9$	-0.84	4.23	± 33

matrices corresponding to the information given in Table 5.5 are

$$C_{e^-,0.28} = \begin{pmatrix} 3.77852 \times 10^{-7} & 0 & -6.51824 \times 10^{-8} \\ 0 & 9.64944 \times 10^{-8} & 0 \\ -6.51824 \times 10^{-8} & 0 & 2.35021 \times 10^{-6} \end{pmatrix}, \quad (5.2)$$

$$C_{e^+,0.28} = \begin{pmatrix} 2.00695 \times 10^{-7} & 0 & 3.94762 \times 10^{-8} \\ 0 & 7.78116 \times 10^{-8} & 0 \\ 3.94762 \times 10^{-8} & 0 & 1.39521 \times 10^{-6} \end{pmatrix}, \quad (5.3)$$

$$C_{e^-,0.56} = \begin{pmatrix} 9.47141 \times 10^{-8} & 0 & 1.8622 \times 10^{-8} \\ 0 & 7.78116 \times 10^{-8} & 0 \\ 1.8622 \times 10^{-8} & 0 & 6.57875 \times 10^{-7} \end{pmatrix}, \quad (5.4)$$

$$C_{e^+,0.56} = \begin{pmatrix} 1.09252 \times 10^{-8} & 0 & -1.88425 \times 10^{-8} \\ 0 & 1.31509 \times 10^{-7} & 0 \\ -1.88425 \times 10^{-7} & 0 & 6.79226 \times 10^{-6} \end{pmatrix}, \quad (5.5)$$

$$C_{e^-,0.9} = \begin{pmatrix} 5.46843 \times 10^{-8} & 0 & 1.07516 \times 10^{-8} \\ 0 & 7.78116 \times 10^{-8} & 0 \\ 1.07516 \times 10^{-8} & 0 & 3.79832 \times 10^{-7} \end{pmatrix}, \quad (5.6)$$

$$C_{e^+,0.9} = \begin{pmatrix} 1.89227 \times 10^{-6} & 0 & -3.26355 \times 10^{-7} \\ 0 & 1.31509 \times 10^{-7} & 0 \\ -3.26355 \times 10^{-7} & 0 & 1.17643 \times 10^{-5} \end{pmatrix}. \quad (5.7)$$

5.4 Preliminary studies for highly asymmetric collisions

Results of a preliminary study of the reconstruction of masses and the resolution on the vertex and on Δt for the decay $D^0 \to K^+K^-$ and $\overline{D}^0 \to K^+e^-\overline{\nu}_e$ with a boost factor $\beta\gamma = 0.9$ are shown here. I have generated 10000 events for this preliminary study and applied selection criteria for rejecting misreconstructed events as shown in Tabs. 5.6 and 5.7. The results of the preliminary analysis are shown in Figs. 5.18 and 5.19, where an efficiency of 48.7% and 43.4% has been obtained when $\beta\gamma = 0.56$ and $\beta\gamma = 0.9$, respectively. It is easy to see from Figs. 5.18 and 5.19 (bottom left) that with these machine configurations (i.e. $\beta\gamma = 0.56, 0.9$), the resolution on Δt has improved with respected to the studied case with low boost ($\beta\gamma = 0.28$). In fact on comparing them one sees that the RMS value of the Δt distribution is 0.34 *ps* 0.23 *ps*, to be compared with the average RMS value in the range 0.76-0.80 *ps* obtained for $\beta\gamma = 0.28$ as shown in Fig. 5.20.

Table 5.6: Allowed range of values for ΔE, M_{BC}, $\sigma_{\Delta t}$ and χ^2 when $\beta\gamma = 0.56$.

Parameter	min.	max.
ΔE [GeV]	-0.018	0.02
M_{BC} [GeV]	1861	1868
χ^2	-	15

Table 5.7: Allowed range of values for ΔE, M_{BC}, $\sigma_{\Delta t}$ and χ^2 when $\beta\gamma = 0.9$.

Parameter	min.	max.
ΔE [GeV]	-0.02	0.02
M_{BC} [GeV]	1861	1868
χ^2	-	15

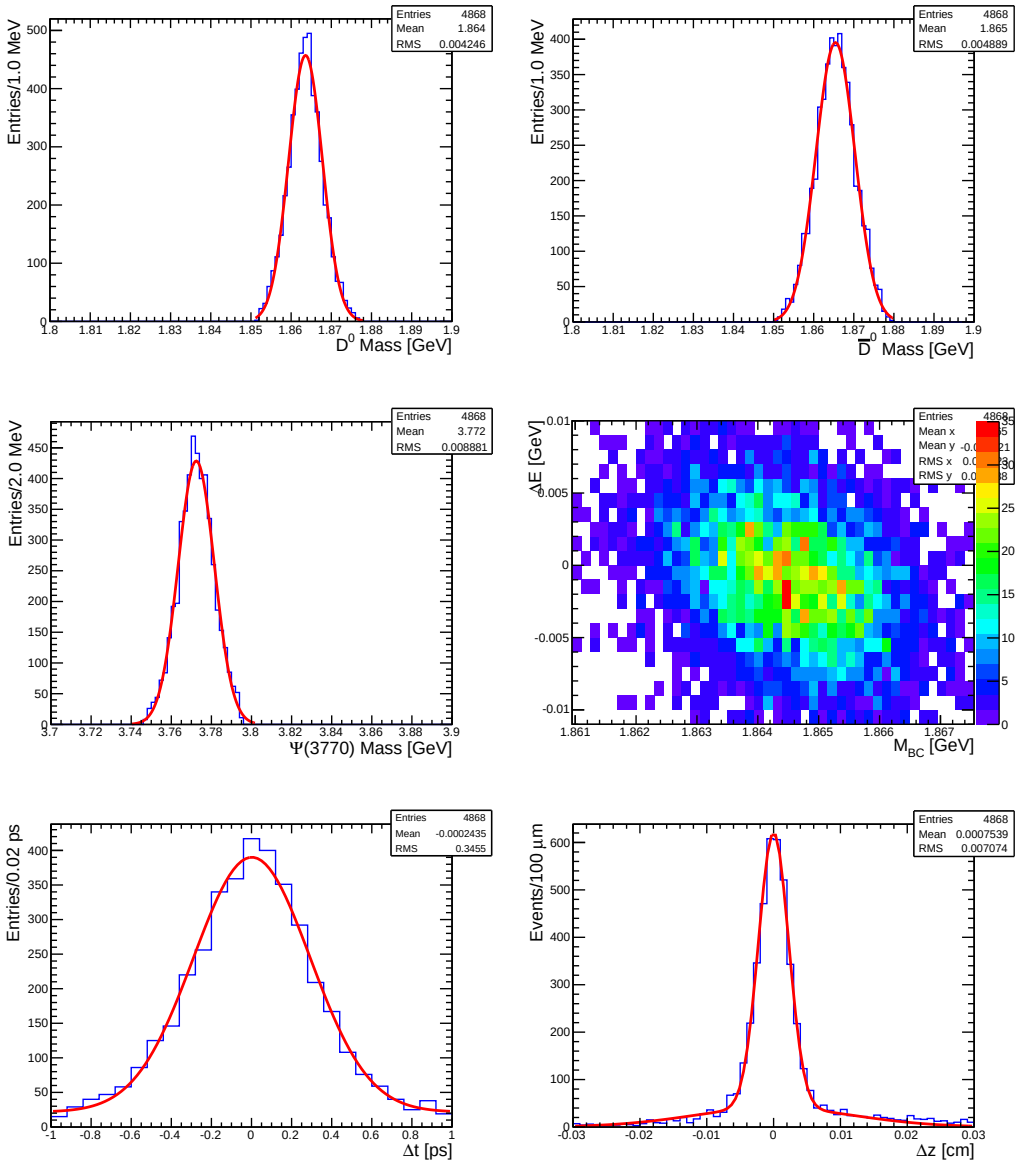

Figure 5.18: Final distributions obtained after selection criteria have been applied to the 10000 generated chains $e^+e^- \rightarrow \Psi(3770) \rightarrow (\overline{D}^0)(D^0) \rightarrow (\pi^+\pi^-)(K^-e^+\nu_e)$ when $\beta\gamma = 0.56$. $\overline{D}^0$ mass (top left), D^0 mass (top left), $\Psi(3770)$ Mass (centre left), ΔE vs. M_{BC} correlation plot (centre right), Δt distribution (bottom left), Δz distribution (bottom right).

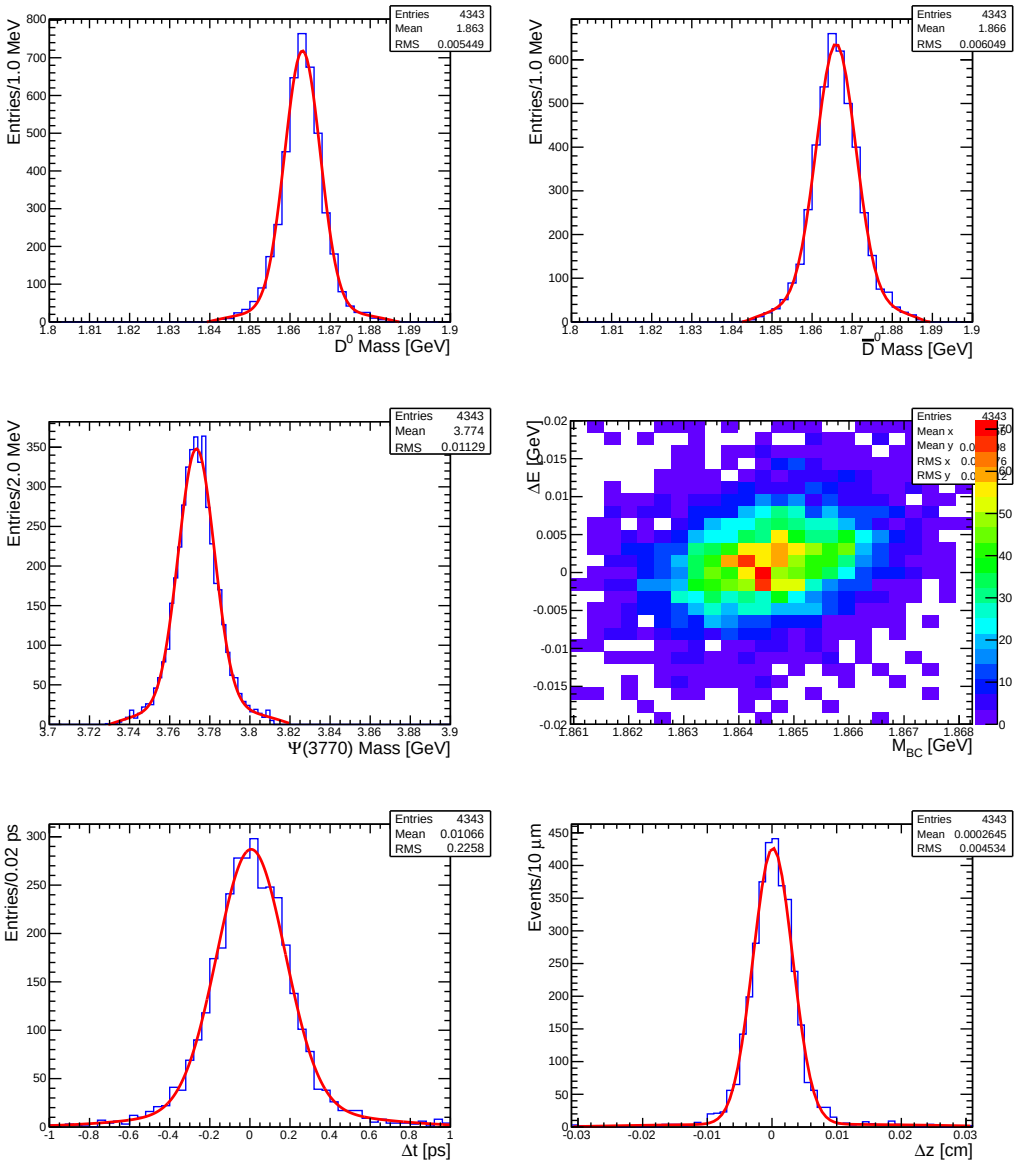

Figure 5.19: Final distributions obtained after selection criteria have been applied to the 10000 generated chains $e^+e^- \rightarrow \Psi(3770) \rightarrow (\overline{D}^0)(D^0) \rightarrow (\pi^+\pi^-)(K^-e^+\nu_e)$ when $\beta\gamma = 0.9$. $\overline{D}^0$ mass (top left), D^0 mass (top left), $\Psi(3770)$ Mass (centre left), ΔE vs. M_{BC} correlation plot (centre right), Δt distribution (bottom left), Δz distribution (bottom right).

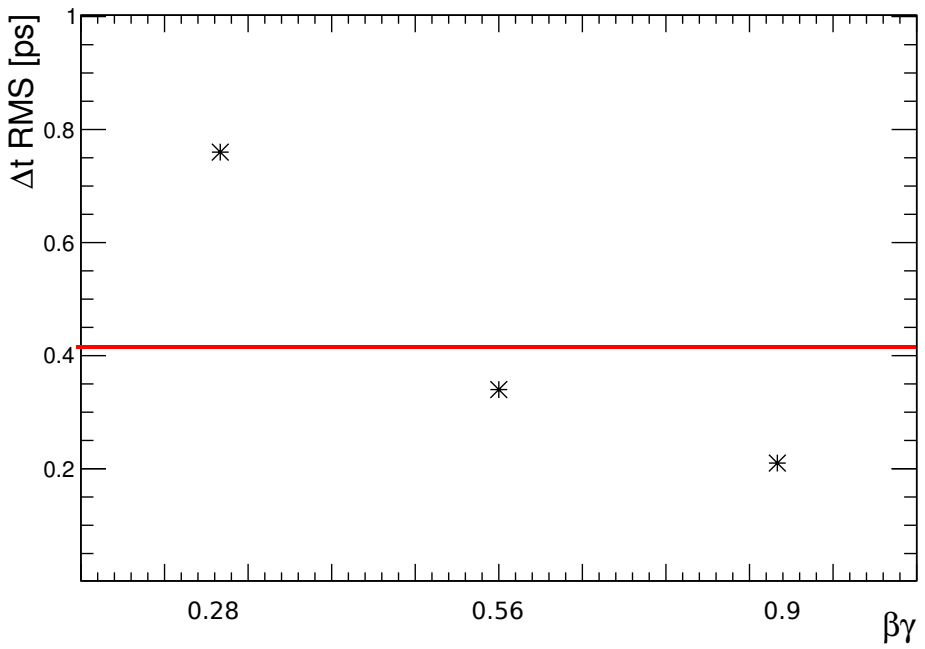

Figure 5.20: Values of the observed RMS of the Δt distribution as function of the boost. The red line represents the D^0 meson lifetime.

The low efficiency observed for the high boost configuration, $\epsilon = 43.4\%$, is due to the fact that more decay products goes through the beam-pipe. The same RooFit study previously discussed has been applied to these decay chains and Figs. 5.21 and 5.22 show the distributions of the central value, the errors, and the pulls of the errors for $\phi = arg[\lambda_f]$, showing a sensitivity on the latter $\sigma_\phi = 14.6°$ and $\sigma_\phi = 6.7°$, for $\beta\gamma = 0.56$ and $\beta\gamma = 0.9$, respectively. These results obtained for larger boost configurations have to be compared to those obtained when the nominal boost configuration was considered, as shown in Fig. 5.23, where one can see that while for $\beta\gamma = 0.56$ the results have largely improved, the ideal case to perform a time-dependent analysis with correlated D^0 mesons would be to build a machine a with a larger boost factor, typically $\beta\gamma = 0.9$. It is interesting to note that while for higher boost configurations than $\beta\gamma = 0.28$ one observes that the signal efficiencies decrease by a small amount, in the cases $\beta\gamma = 0.56$ and $\beta\gamma = 0.9$ the Δt

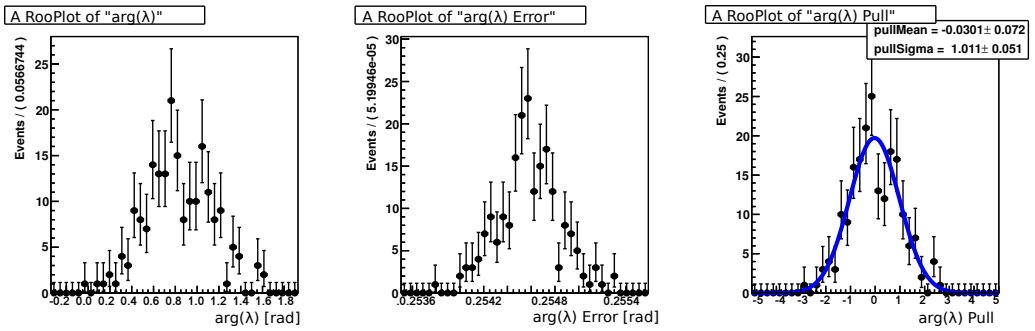

Figure 5.21: $\phi_{\pi\pi} = \phi_{MIX} + 2\beta_{c,eff}$ (left), error on $\phi_{MIX} + 2\beta_{c,eff}$ (centre), pulls of the errors (right) for $\beta\gamma = 0.56$.

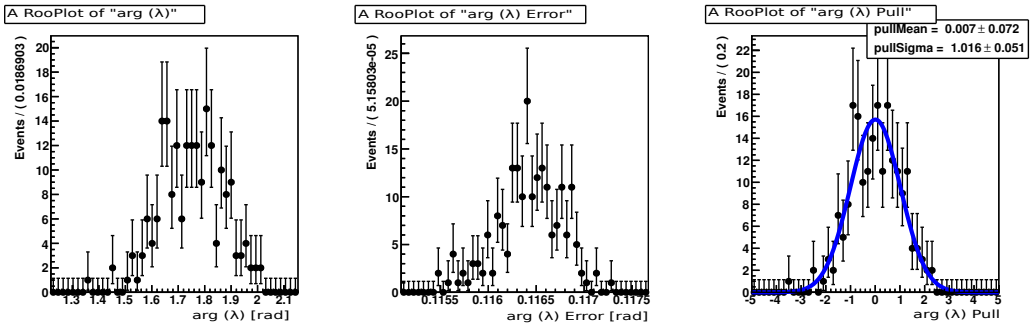

Figure 5.22: $\phi_{\pi\pi} = \phi_{MIX} + 2\beta_{c,eff}$ (left), error on $\phi_{MIX} + 2\beta_{c,eff}$ (centre), pulls of the errors (right) for $\beta\gamma = 0.9$.

resolution improves to values which are smaller than the lifetime of the D^0 meson, so overall the effect of improving the resolution function outweighs the losses due to the decreased signal efficiencies.

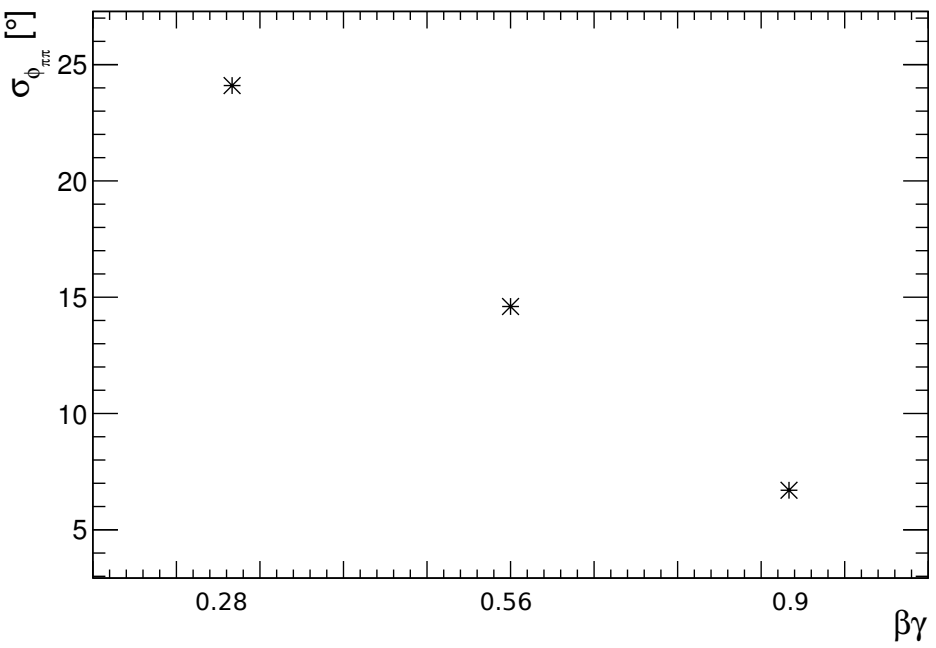

Figure 5.23: Values of the obtained precision on $\phi_{\pi\pi}$ as function of the boost.

5.5 A triple Gaussian fit to the resolution function

As discussed in the previous chapter the resolution function can be parametrised using three Gaussian functions as follow

$$R(\delta t, \sigma_{\Delta t}) = k \left[\frac{f_c}{S_c \sigma_{\Delta t}} e^{-\frac{(\delta_t - \mu_c \sigma_{\Delta t})^2}{2(S_c \sigma_{\Delta t})^2}} + \frac{1-f}{S_t \sigma_{\Delta t}} e^{-\frac{(\delta_t - \mu_t \sigma_{\Delta t})^2}{2(S_t \sigma_{\Delta t})^2}} + \frac{f_o}{\sigma_o} e^{-\frac{\delta t^2}{2\sigma_o^2}} \right], \quad (5.8)$$

where the quantities involved are the same as in Eq. (4.11), f_o represents the outlier Gaussian function (considered to include mis-reconstructed events) and $f = f_c - f_o$. A study of the resolution function using a triple Gaussian resolution function has been performed, this has shown that while the implementation of a third Gaussian will improve the quality of the fit this will be a second order effect on the parameter that one wants to extract (*i.e.* ϕ). As an example Fig. 5.24 and Fig. 5.25 show the resolution function obtained by the convolution of three Gaussian functions and the results of the RooFit study on $\phi_{\pi\pi} = arg[\lambda_f(D^0 \to \pi^+\pi^-)] = \phi_{MIX} + 2\beta_{c,eff}$, where a sensitivity on $\phi_{\pi\pi} = \phi_{MIX} + 2\beta_{c,eff}$ when 1 ab^{-1} of data is collected at the charm threshold with a boost factor $\beta\gamma = 0.28$ is $\sigma_{\phi_{\pi\pi}} = 23.8°$. On comparing this result to the one obtained previously when in the fit two Gaussian functions have been considered, one can sees that adding a third Gaussian in the fit will allow to better fit the data in region around $\Delta t = 0$ allowing a slightly smaller value of $\sigma_{\phi_{\pi\pi}}$.

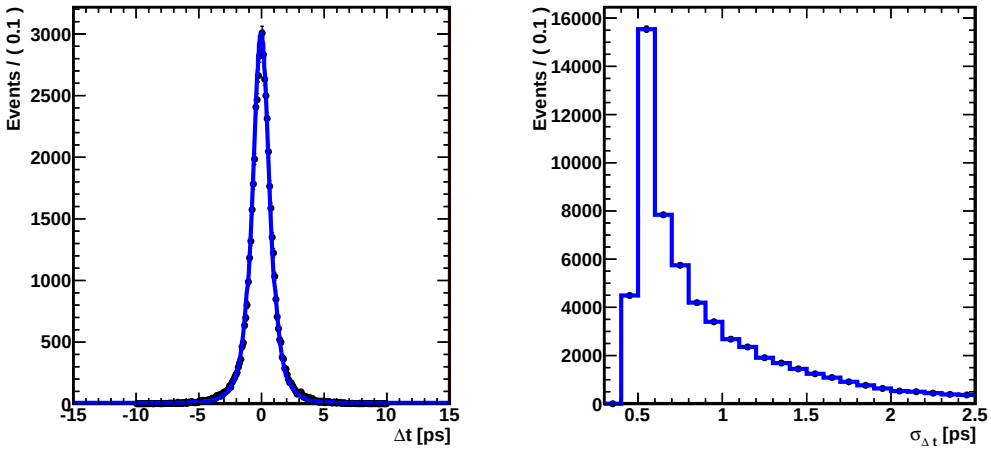

Figure 5.24: Δt resolution function for $e^+e^- \to \Psi(3770) \to (\overline{D}^0)(D^0) \to (\pi^+\pi^-)(K^-e^+\nu_e)$ (left) and the error on Δt evaluated on an event-by-event basis, $\sigma_{\Delta t}$ (right).

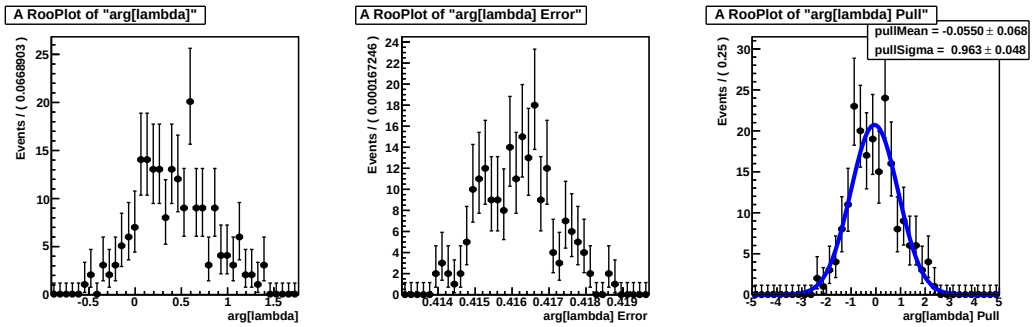

Figure 5.25: Fitted value of $\phi_{\pi\pi} = \phi_{MIX} + 2\beta_{c,eff} = arg$[lambda] (left), error on $\phi_{MIX} + 2\beta_{c,eff}$ (centre), pulls of the errors (right) when a three Gaussian resolution function is considered.

Chapter 6

Cherwell

ARACHNID is a Collaboration of scientists from University of Birmingham, University of Bristol, Daresbury Laboratory, Deutsches Elektronen-Synchrotron (DESY), Queen Mary University of London and Rutherford Appleton Laboratory aimed at studying the Cherwell sensor, a technology based on complementary metal oxide semiconductor (CMOS) monolithic active pixel sensors (MAPS), manufactured by TowerJazz Semiconductor Ltd. [43] with 0.18μm technology implementing a four transistor (4T) architecture. In this chapter I will present the main characteristics of the Cherwell sensor and will discuss the set up adopted for a test beam performed at CERN where six Cherwell sensors have been irradiated with pion beams delivered by the *super proton synchrotron* (SPS). Various ideas and proposals have been evaluated for the Super$B$ SVT and in particular for the Layer 0 as discussed previously in Sec. 3.3.1, for example using hybrid pixels [44] or striplets [45]. However, as described in the ARACHNID research proposal available in [46], there are many features of CMOS pixel sensors suggesting the possibility of their application as vertexing/tracking systems in particle detectors. The main features we identified are [46]

- high granularity with small pixel sizes;
- electronics can be integrated with the sensor thus avoiding high density connections or the complicated flip-chip technologies in hybrid pixel detector systems;

- use a variant of an industry standard process, leading to high yield;
- low cost due to their extensive use in industry;
- low cost also leads to the building of 'disposable' detectors which reduces maintenance costs;
- they do not use a lot of power;
- improved signal-to-noise;
- they are proving to have the radiation hardness needed.

It is interesting at this point to compare the mentioned technology features also with other possible detector technologies adopted in other experiments. AT Super$B$ there would be very stringent requirement on the properties and features of the Layer 0 of the SVT. Due to the high luminosity of the machine a radiation tolerance of the order of 2.5-3.5 Mrad/year is required for striplets-pixels. A comparison of the material budget in terms of the radiation length X_0, expected background rate and power dissipation for the Super$B$ Layer 0 for striplets and CMOS MAPS is shown in Tab. 6.1 [39][1]. in terms of radiation hardness a full calculation for the Cherwell sensor has not been performed yet, however it is reasonable to assume similar values to those obtained for the FORTIS sensor which are in the range 500-1000 krad, while striplets and hybrid pixels (ATLAS and CMS experiments at CERN use this kind of technology, and there is ongoing RD via the RD 50 Collaboration to seek out more radiation hard technologies for LHC use) are in the range between 5-60 Mrad [47]. Silicon drift detectors (SDDs) are the main part of the tracking system of the ALICE experiment with a radiation hardness of 250 krad and comparable material budget and readout rates to those from a CMOS MAPS. DEPFET sensors have similar properties to those of CMOS MAPS in terms of radiation hardness ($\simeq$ 1 Mrad) but with lower readout rates, but due to the fact that the DEPFET Collaboration was not involved in the Super$B$ experiment this sensor technology has not been

[1]The expected background level is calculated including with a $\times 5$ safety factor for striplets length of about 2 cm and 50 μm pitch and for pixels with a 50×50 μm^2 pixel area.

Table 6.1: Material budget, background, power dissipated, and efficiencies for different SVT Layer 0 technologies: striplets, CMOS MAPS and hybrid pixels.

	Striplets	CMOS MAPS	Hybrid Pixels
Sensor	0.21%	0.05 %	0.11-0.21%
FE-chip + bump bonding			0.14-0.19%
Multilayer bus or fanout	0.15%	0.15-0.30%	0.15-0.30%
Module Supp. + ground pl.	0.09%	0.15%	0.15%
Total Material Budget (X_0)	0.45%	0.35-0.50%	0.55-0.85%
Expected background	1 MHz/strip	25 kHz/pixel	5MHz/cm^2
Power dissipated	4mW/channel	30μW/channel	30μW/channel
Efficiency	(>)99.4%	(>)99.7%	(>)99.0%

considered. It should also be noted that DEPFET is not an industry standard, but a bespoke process resulting in sensors that are made in university laboratories. The yields were very low for early prototypes and this would not be a cost effective solution to build on for Super$B$ given the existing RD programmes that were being pursued by the UK and Italian groups with access to industry quality production of designs. HV-CMOS devices are going through a strong RD programme however direct and fair comparison with the technologies that were under consideration for Super$B$ is not possible as the HV-CMOS technology is still in the very early stages of development and complicated test chips have not been demonstrated yet, only simple structures have been investigated in detail. However this is a technology that is expected to start maturing over the next few years. Charge-coupled devices (CCDs) can be used as radiation detectors to provide the position of a particle passing through the detection array. When photons or charged particles passes through the surface of a CCD, the electrons in the silicon substrate are excited by the photoelectric effect and collected by an electrode allowing the total charge on each pixel to be registered and digitalized. The SLD vertex detector was based on CCD technology and the possibility to use CCD in

new experiments has been considered for the linear collider detector, again it is not possible to make direct comparisons of comparable chip designs as the operational requirements of a linear collider detector at a Higgs Factory is driven by the bunch structure, which is very different from the continuous mode of operation that was expected at a Super$B$ factory. All the detector technologies introduced here can also have a high granularity obtained by the 25×25 μm pixels, but for CMOS MAPS it could be possible to reach higher granularity through the implementation of sensor with with pixel size down to 1μm. In addition to this the Cherwell sensor has reached (and in some cases exceeded) its design performance, in particular an improved efficiency ($> 99.7\%$) has been obtained for all the various Cherwell sensor typologies. For these reasons we think that it is useful to test this technology and quantify in detail its capabilities.

6.1 Three and four transistor pixel architectures

The most common architecture for a CMOS pixel sensor is based on the so-called three-transistor architecture, or simply 3T architecture, consisting of a diode, a reset transistor, a source follower transistor and a row select transistor as shown in Fig. 6.1 (left). The 3T architecture works in a simple way, first the diode is reset by the reset transistor and then the charge deposited, due to the passage of an ionizing particle for example, is collected. An integration time is set during which any charge deposited in a pixel is collected by an n-well diode, and after this, the row select transistor is activated and the signal is read out. In the 4T architecture the diode is replaced by a pinned photodiode and two additional elements, the transfer gate (TX) and the floating diffusion node (FD), are added in the circuit as shown in Fig. 6.1 (right). An important characteristic of the pinned photodiode is that it is manufactured with an additional shallow p-type implant above the standard n-type diffusion on a p-type epitaxial layer, creating a p-n-p structure. Because of the p-n-p structure, when the floating diffusion is reset to a voltage above or equal to the pinning voltage and TX is turned on, the photodi-

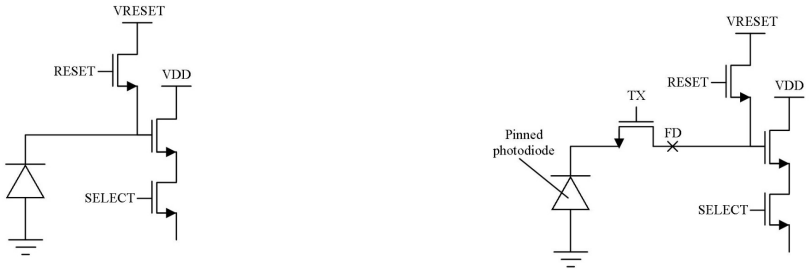

Figure 6.1: (left) 3T CMOS architecture and (right) 4T CMOS architecture [48].

ode becomes fully depleted, allowing for noiseless charge transfer. The main implication of adopting a 4T architecture with respect to a 3T architecture is that charge collection and readout are physically separated. First, separating charge collection and readout allows the sensor to operate with lower noise levels. Noise, in fact, derives mainly from resetting the reset transistor, but in the case of a 4T architecture, sampling the floating diffusion nodes before and after the transfer gate it is possible to remove the reset noise. Second, the sensitivity of the sensor to small charge collection (conversion gain) can be increased in the voltage domain. The voltage domain is given by $V = q/C$ where q is the charge and C the capacitance, so the capacitance of a 3T architecture is given by the capacitance of the diode, while in a 4T architecture the capacitance is given by that of the floating diffusion node and the geometry of this can be modified allowing for smaller levels of charge to be collected.

6.2 CMOS (IN)-MAPS

In order to understand how the CMOS (IN)-MAPS based technology works and how to improve it, one has to consider a few elements that are included in the electronics:
-An NMOS, or n-type metal-oxide-semiconductor, generally implements logic gates using n-type metal-oxide-semiconductor field effect transistors (MOS-

FETs).
-A PMOS, or p-type metal-oxide-semiconductor, implements logic gates by using p-channel MOSFETs and creates an inversion layer in an n-type transistor body.
-Charge collection in a MAPS is obtained through diffusion by using a n-well diode, limiting the in-pixel electronics to only NMOS transistors, as the n-well from the PMOS transistors would parasitically collect the signal charge and therefore lead to a low charge collection efficiency [49].
However, it is possible to isolate the n-wells of PMOS transistors from the epitaxial layer by using a standard bulk CMOS process, modified by adding a deep p-implant which shields the n-wells from the PMOS and therefore allows full CMOS capability in-pixel [49] [50]. The situation is illustrated in Fig. 6.2 [49], and the new technology has been called INMAPS, where "IN" stays for isolated n-wells, or intelligent [50]. Fig. 6.2 illustrates the effect

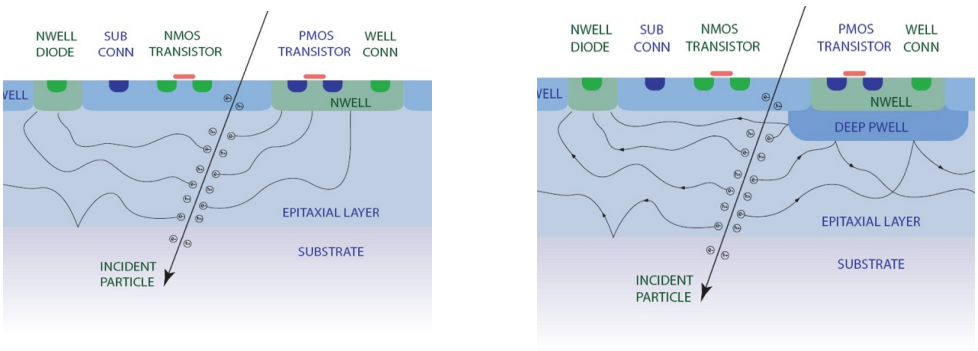

Figure 6.2: Standard CMOS (left), CMOS implants with a deep p-well to shield the PMOS n-well [49].

of a particle passing through a standard CMOS device (left) and through a CMOS (IN)-MAPS where a deep p-well has been implanted (INMAPS) to shield the PMOS n-well (right). One can see that in the second case the presence of the deep p-well shields the PMOS n-well and in turn enables full in-pixel processing capability [49]. The epitaxial layer suffers from radiation damage, and since the depletion width depends on the resistivity, a higher resistivity epitaxial layer on one hand is more radiation hard, on the other hand may allow for a faster charge collection [48]. To evaluate the perfor-

mance of the Cherwell, we tested six sensors during a test beam at CERN in November 2012, four of them with an epitaxial layer resistivity of 10-100 Ωcm (standard resistivity) and two with an epitaxial layer resistivity of 1-10 kΩcm (high resistivity).

6.2.1 The Cherwell sensor

Cherwell is a prototype CMOS (IN)-MAPS with two possible applications: calorimetry and vertexing/tracking. The sensor, shown in Fig. 6.3, is characterised by low costs (relative to traditional silicon sensor devices), low power requirements and a fully active area, and due to the different possible applications there are four divisions of pixels to readout, in addition to ancillary circuitry for processing and readout at the bottom edge of the sensor. The left side of the sensor is designed for calorimetry studies while the right side is designed for vertexing and tracking. Both sides are then divided in two regions, so that one has four different devices in one sensor. These divisions

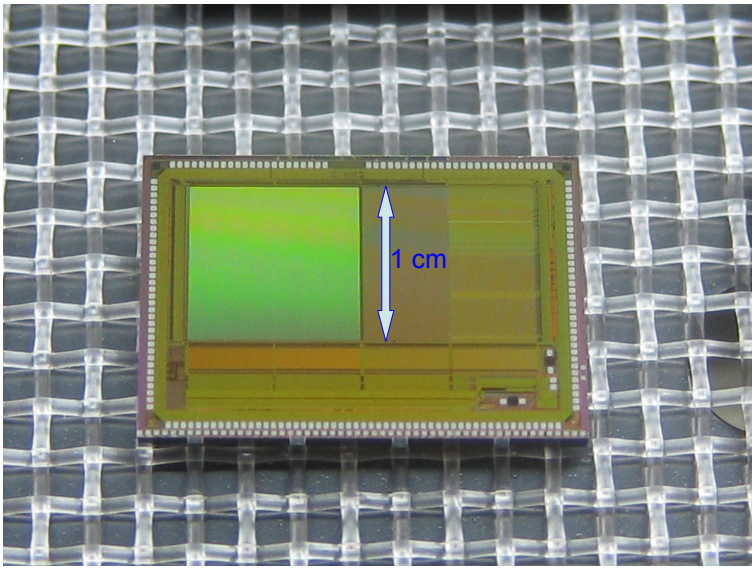

Figure 6.3: The UK Cherwell MAPS chip; we were working toward a design that could have been used for the Layer 0 of the Super$B$ SVT and ALICE tracker upgrade projects.

are as follows:

-the first from the left is a matrix of 96×48 25×25 μm pixels called **DECAL 25**, with an analogue-to-digital converter (ADC) per column at the end (bottom) of the column, and it is arranged such that four contiguous pixels can be ganged together to create a virtual $50 \times 50 \mu m$ pixel in order to study charge sharing in detail,
-the second is a matrix of 48×24 50×50 μm pixels called **DECAL 50**, with an ADC per column at end of the column,
-the third is a matrix of 96×48 25×25 μm pixels, called **reference pixels**, with an ADC per column at the end of each column for rolling shutter read-out (these pixels are the focus of results discussed here),
-and the last one is a matrix of 96×48 25×25 μm pixels, called **strixels**, with an ADC integrated in-pixel eliminating end-column electronics and increasing the total active area of the chip.
A new generation of vertex detector has to be designed to work in high rate environments as was the case for the SVT Layer0 at Super$B$ or as it is for ALICE or for the future ILC project. This technology needs to be validated in terms of radiation hardness, resolution and efficiency. The ALICE project is adopting the strixel functionality in its prototype design, following on from ARACHNID having verified the basic functionality of that concept. The next section discusses the 2012 Cherwell CERN test beam campaign.

6.3 Test beam at CERN

The Cherwell sensor has been tested through pion beam irradiation in the north area of CERN in the Prevessin site in November 2012. The pion beam in the experimental hall is delivered as follows: first a proton beam from the super proton synchrotron (SPS) is delivered in super-cycles consisting of two cycles that can be seen on the screen present in each control room and with a configuration that changes frequently. Each super-cycle is characterised by two top regions and two bottom regions indicated by the maximum and minimum values of the bending strength of the extraction magnets as shown in Fig. 6.4. When the bending strength at the extraction point is kept low there is no extraction, allowing protons to be accelerated or to be delivered to other experiments (i.e. LHC). When the beam is extracted from the SPS

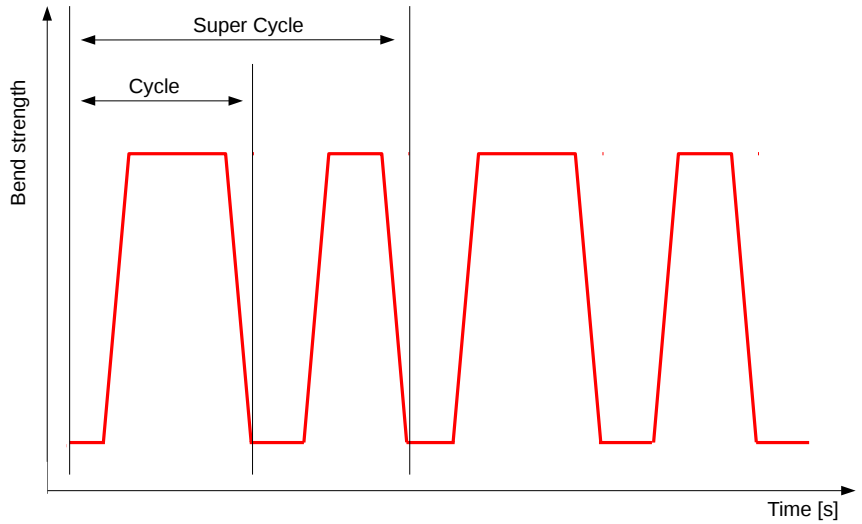

Figure 6.4: Schematic representation of cycles and super-cycles at the SPS expressed as the bending strength at the extraction point as function of time and characterised by a top region during which the extraction takes place.

to reach the secondary areas, protons in the primary area have a central energy of 450 GeV in the primary beam area and the beam reaches the secondary beam areas with a reduced energy of 120 GeV after impinging on primary targets to create pions as shown in Fig. 6.5. The beam intensity in the secondary areas is controlled through the use of collimators, in particular the momentum defining C3 collimator (the number indicating the position in the beam line) controls and defines the beam profile. The momentum spread $\Delta p/p$ during test beam operation is approximately 0.5%, which is obtained through a particular configuration of the collimator opening (10 mm) [51]. For the Cherwell test beam we were allocated the H6B area shown in Fig. 6.6 from the 7^{th} to the 14^{th} of November 2012, and the control room associated to this area was the HNA-457 control room. Due to SPS maintenance and to flooding problems during the period dedicated to our test beam, we were able to collect data for 2.5 days. Beam properties are controlled by using the

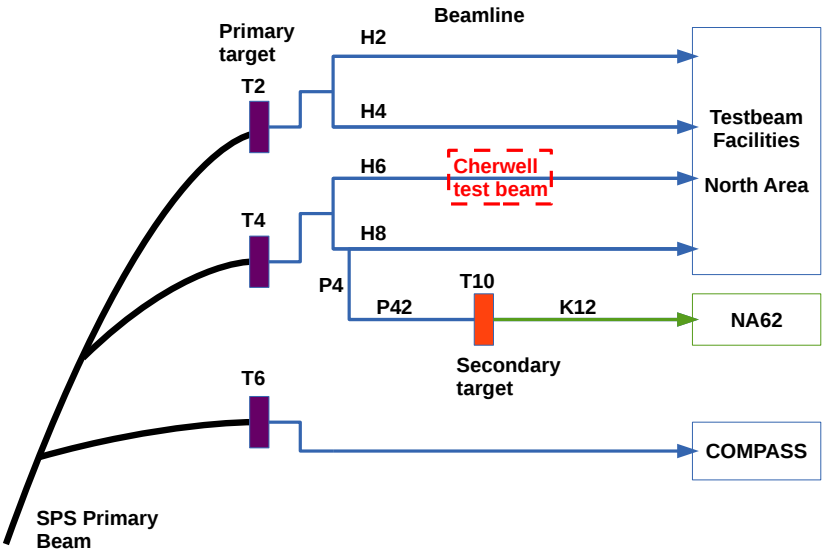

Figure 6.5: Schematic showing how the beams are generated from the SPS in the experimental test beam area, with the area allocated for the Cherwell test highlighted in red.

CESAR software from the BEAM-PC in room HNA-453/HNA-457. The H6B area is equipped with a telescope for the alignment, and it can be controlled using the EUDAQ RunControl software from the computer located in HNA-457.

6.3.1 EUDET pixel telescope

The EUDET pixel telescope or simply EUDET telescope, shown in Fig. 6.7, can be used to obtain an alignment between the detector(s) and the beam[2]. The telescope consists of a number of sub-components and these are:
-the **MIMOSA** sensors, six planes of pixel sensors consisting of 576×1152 pixels with a pitch of 18.5 μm.
-the **EUDRB**, which is the EUDET DAQ system,

[2]A more detailed description can be found in [52].

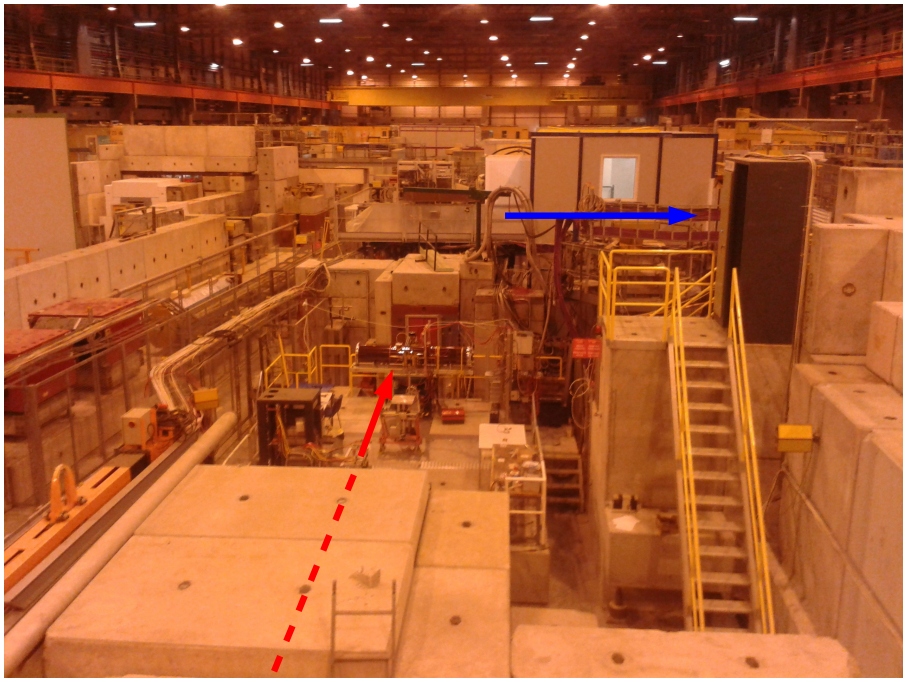

Figure 6.6: View of the H6B area allocated to the ARACHNID Collaboration for the Cherwell test beam at CERN, the blue line show the entrance to the area and the red line the direction of the π-beam.

-**MVME**: VME board computer MVME6100 to read the EUDRBs,
-**BBLA**: Blue box level adapters,
-**BBCB**: Blue box (little one) for buffering the clocks,
-**JTAG**: MIMOSA sensors are programmed via JTAG chain,
-**TLU**: Trigger Logic Unit.
Three computers control the EUDET system. In the beam area the Linux machine (zenpixell3) is used for communication with the **TLU**, and a windows PC to program **JTAG**, control the steering of the XY table and monitor the currents of the sensors in the telescope. In the Control Room a Mac PC is used to run a VNC connection to control zenpixell3 and to run EUDAQ. The VME crate powers up the DAQ system and this is the first component to be turned on. The power switches of the DAQ boards are located in the front side of the devices. The power for the sensors is provided by two AGILENT E3644A power supplies (for the **MIMOSA** sensors at +8

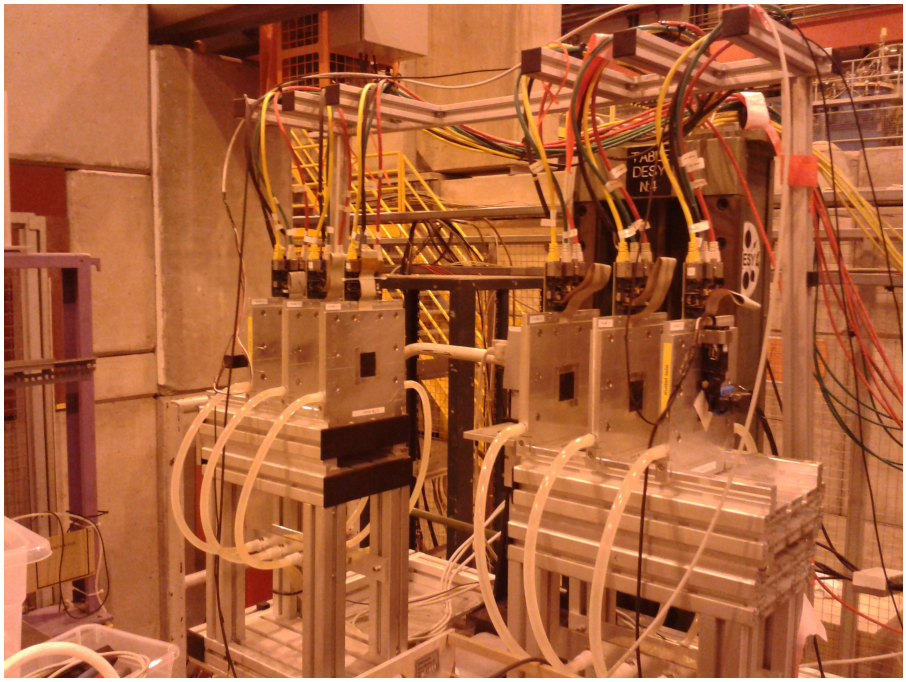

Figure 6.7: View of EUDET telescope.

V with current drawn around 2.88 A, and one at +5 V for the **JTAG**). Currents can be monitored from the control room by connecting to the zenpixelw machine.

6.3.2 Cherwell Stack

Six Cherwell sensors have been tested at CERN during test beam operation with the following classification:
-A for two standard wafers with a low noise Vt implant for the source-drain,
-B for two high-resistivity wafers with a low noise Vt implant for the source-drain,
-C two standard wafers with a standard noise Vt implant for the source-drain.

The six sensors have been mounted (Fig. 6.8) inside a stack as parallel layers as shown in Fig. 6.9, where three additional scintillators have been mounted on the front and back side of the stack as shown in Fig. 6.10. The stack

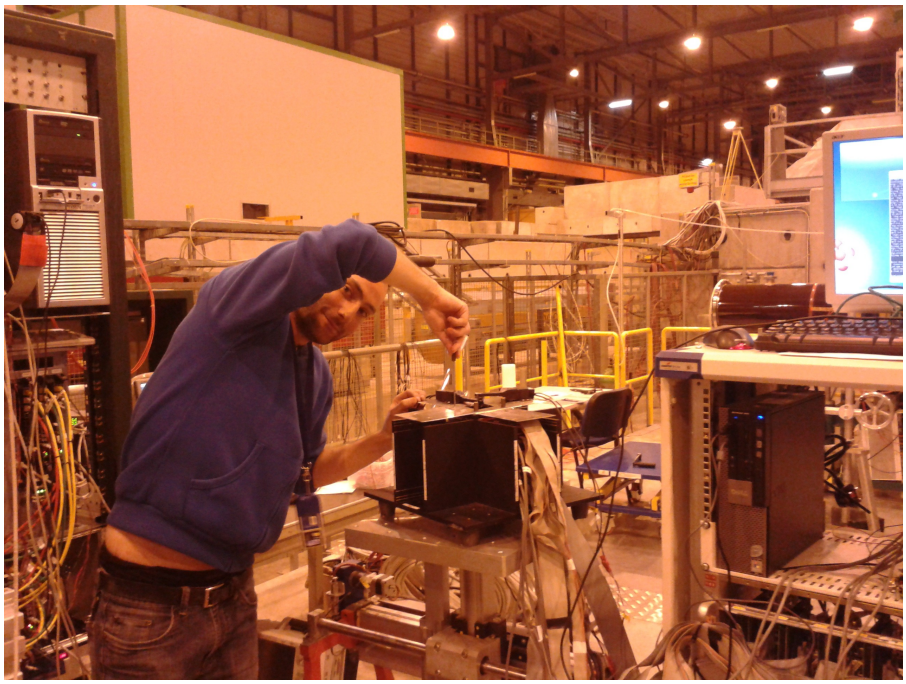

Figure 6.8: The set up of the Cherwell stack of sensors in the H6B experimental hall.

was then placed on a mechanical $x - y$ stage controlled from the control room[3]. All the sensor layers were connected to our data acquisition system (DAQ) and connected to a computer that was kept in the experimental hall through a USB DAQ interface to allow data storage, shown on the right side of Fig. 6.8. This computer was connected to the control room, allowing us to perform real time data quality checks and online analysis.

6.3.3 Positioning of the Cherwell stack

The EUDET telescope shown in Fig. 6.7, can be used for alignment. However, for the alignment we decided first to use a rudimentary procedure consisting

[3]The stage and the controller used to control it were connected to the same power supply. This would have represented a problem during test beam operations, since no access to the experimental area is permitted during beam time. However, a secure 20 m long electric cable was found to enable the stage to be controlled remotely from the control room. This simple operation resulted in an extremely simple alignment procedure.

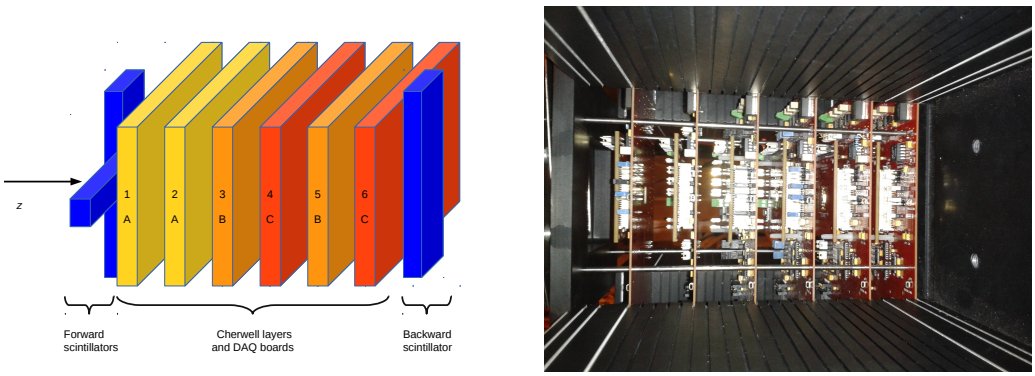

Figure 6.9: Schematic of the six Cherwell sensors where in yellow and indicated by the letter A are shown the standard resistivity wafers with low noise Vt implants, in orange and indicated by letter B the high-resistivity wafers with low noise Vt implant for the source-drain and in red and indicated by the letter C the standard wafers with standard noise Vt implant for the source-drain implant placed in the stack. Three scintillators of the trigger unit are represented by blue blocks (left), the numbering on each sensor block indicates the position of the sensor in the stack. Picture of the six sensors assembled in the stack (right).

of placing the stack containing the six sensor layers on the mechanical $x-y$ stage and to make sure that the axis passing through the centre of each plane where the Cherwell sensors were positioned was on, or parallel to, the beam line. Moving the stage from the control room during data taking allowed us to improve the physical alignment by performing a check on all the sensors (online) and ensuring that each of them was irradiated during test beam. The procedure consisted of moving the stack first in line with the centre of the last wafer of the EUDET telescope: this alignment was done by pointing an $x-y$ laser to the centre of the last sensor layer and then rotating the stack so that the intersection point of the two forward scintillators was on the same line of the center of the EUDET telescope as shown in Fig. 6.11 (top) and then we added the last (backward side) scintillator as shown in Fig. 6.11 (bottom) and in Fig. 6.12: as a final check, the laser crosshair was seen to be in the centre of the active area of the backward scintillator. Thus any further required improvement could be done during data acquisition (between runs)

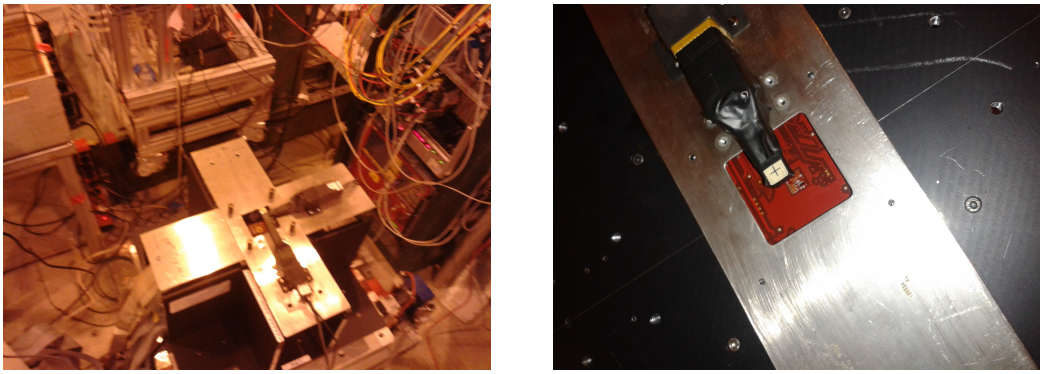

Figure 6.10: Scintillators mounted on the forward (upstream) and backward (downstream) side of the stack.

by controlling the $x - y$ stage. If all the sensors are aligned correctly one then should observe a correlation between the charge deposited in the rows and columns of each sensor, and in particular a correlation between the first sensor (sensor 0) and the sixth sensor (sensor 5) should be observed. After performing the mechanical alignment the full apparatus was then covered with a light tight black cover as shown in Fig. 6.13. During beam time we evaluated the quality of the alignment of the sensors relative to beam and improved it using the mechanical stage. Correlation plots between the sensors are shown in Fig. 6.14, showing that we observed the expected correlation and obtained a reasonable alignment of all the sensors relative to the beam line (the plots were produced by Tamsin Nooney who was responsible for performing an offline alignment study of the Cherwell sensor stack [53]).

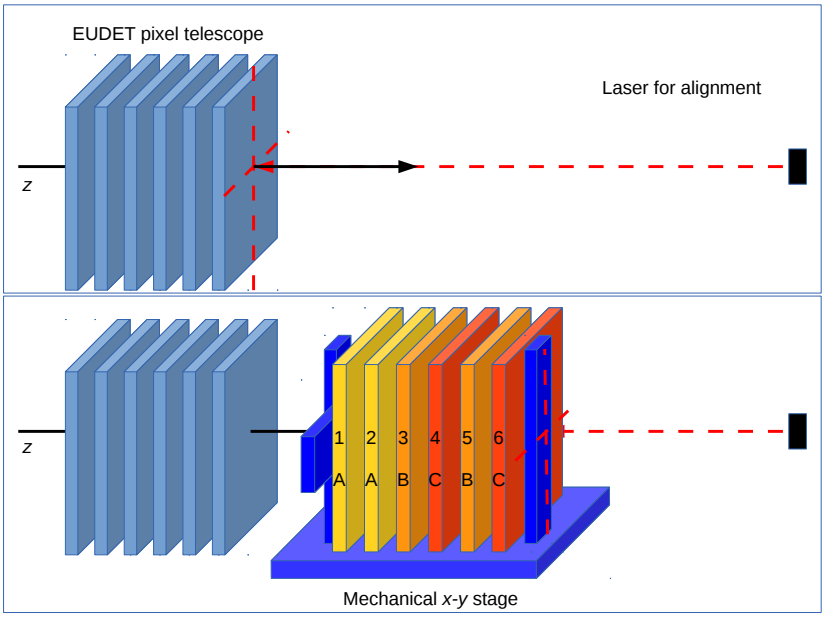

Figure 6.11: Schematics of the procedure followed to align the sensors to the EUDET telescope. A laser was first used to point at the centre of EUDET system (top) and repeated along the Cherwell stack and scintillators (bottom).

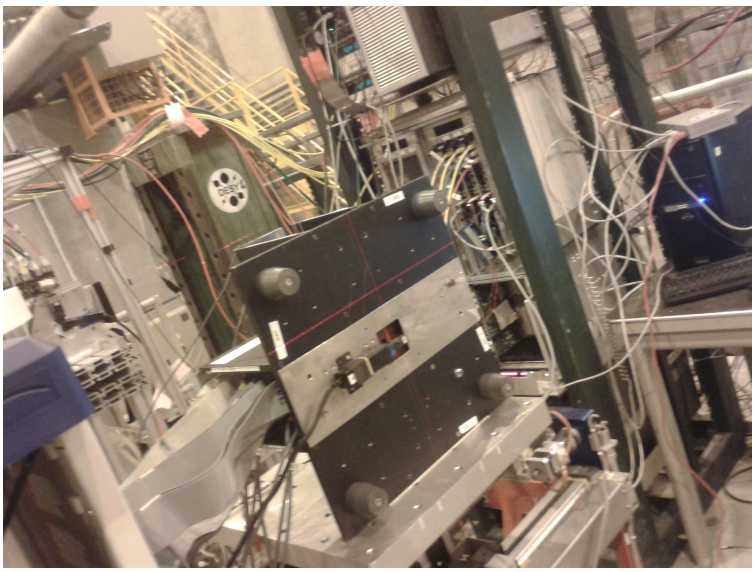

Figure 6.12: Laser used for mechanical alignment pointing at the back side of the stack.

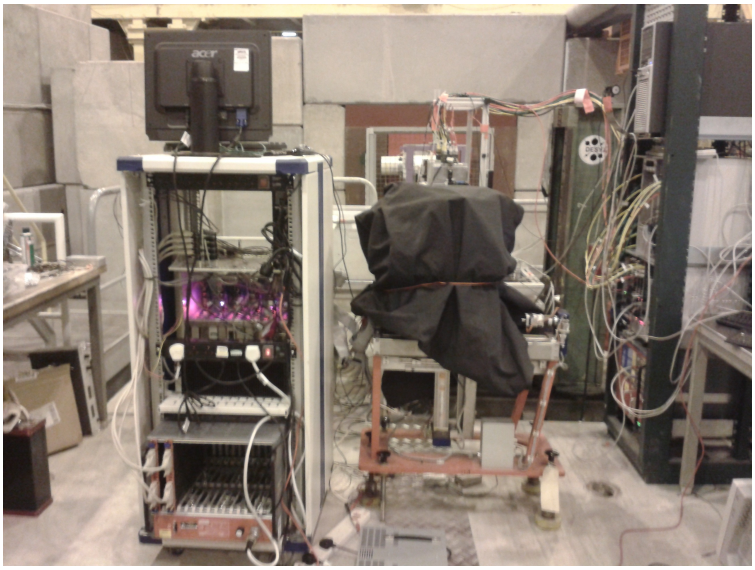

Figure 6.13: View of the Cherwell test beam apparatus covered with a high absorbing light tight cover ready for data taking. On the left side the computer used for data acquisition with USB DAQ boards lit up showing a functioning of the system.

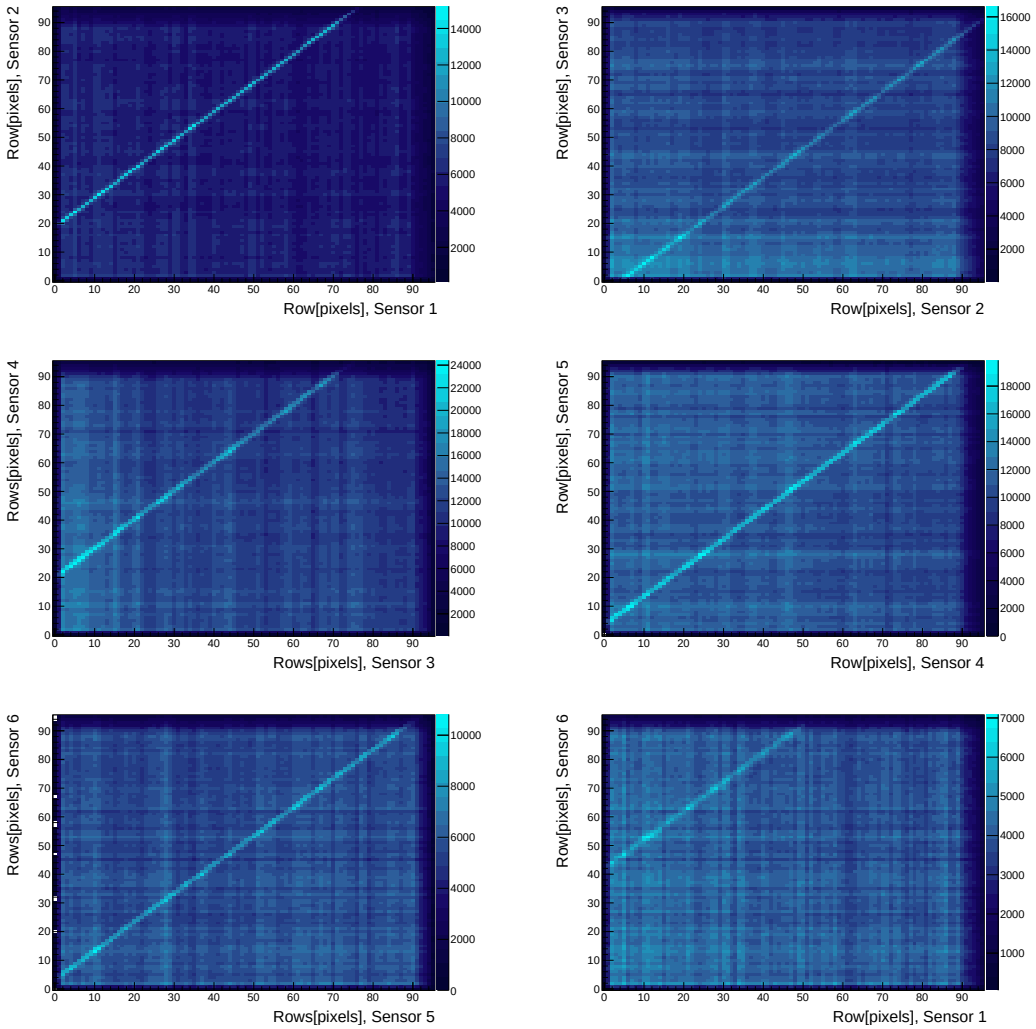

Figure 6.14: Correlation plots for sensor 1 with respect to sensor 2 (top left), sensor 2 with respect to sensor 3 (top right), sensor 3 with respect to sensor 4 (centre left), sensor 4 with respect to sensor 5 (centre right), sensor 5 with respect to sensor 6 (bottom left), sensor 1 with respect to sensor 6 (bottom right), showing correct alignment between the rows of the sensors. Similar correlation plots are obtained in terms of the pixel columns.

6.3.4 Trigger and data acquisition system

The trigger requirement for data acquisition was related to particles passing through the scintillators, and in particular we required a triple coincidence trigger on the three scintillators to acquire the data. The trigger system was sampled at the rate of 1 KHz with an acquisition (trigger) rate of ≈3Hz. Since the three scintillators were aligned with the sensors and that we require for all the three to be hit by particles, the sensor stack should also be hit. As shown in Fig. 6.15, data are acquired and stored on a Linux machine: the triple coincidence trigger activates the DAQ boards for data acquisition (USB DAQ systems inherited from the SPiDeR Collaboration), data are transferred to the PC, and backed up on external hard drives for subsequent analysis offline.

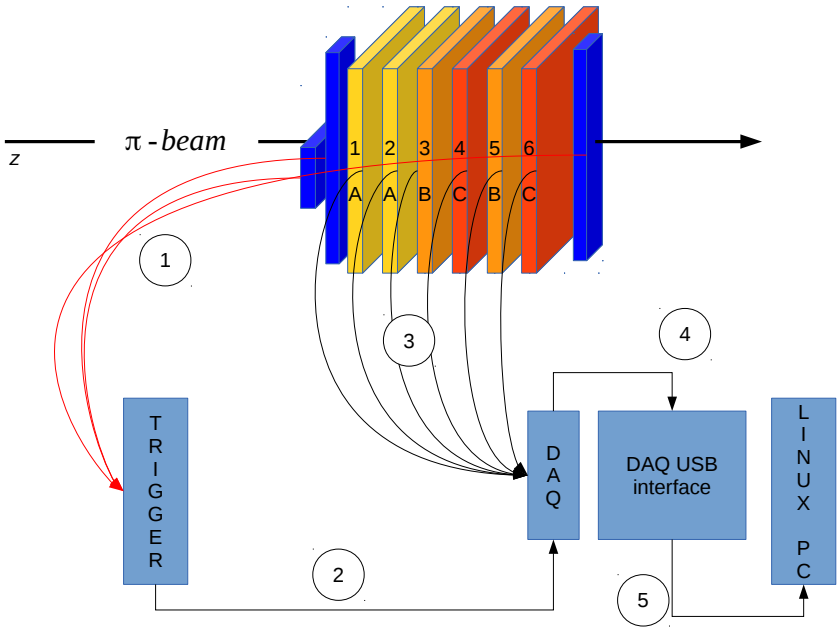

Figure 6.15: Data acquisition procedure. The triple coincidence trigger (1) activates the DAQ boards which readout the Cherwell sensors (2 and 3), the data recorded are transferred via the USB DAQ systems to the PC (4) and stored on disk (5).

Chapter 7

Cherwell test beam results

Shortly after the test beam performed at CERN, each group involved in the ARACHNID Collaboration started to perform the analysis of the data. At Queen Mary University of London we were interested in the study of the reference pixels data, and my involvement in the analysis was related to the reconstruction of so-called clusters. Clusters are related to the region of the sensor which shows charge deposited when a charged particle passes through it. Ideally the particle passes through one pixel, however electric charge is deposited and may also be collected by the surrounding pixels creating a cluster. This chapter describes the work done in order to understand the most appropriate way to reconstruct clusters of deposited energy for a subsequent high level analysis of the test beam data. A rectangular clustering algorithm centred on a single seed pixel was studied and the results of that work are presented in this chapter.

Section 7.1 describes reconstruction of the raw data, and clustering and sensor alignment is discussed in section 7.2. The latter section includes a summary of sensor efficiency and signal to noise estimated for the sensors in the testbeam stack. In order to produce these results it was necessary to align the sensors relative to each other using correlation plots for rows/columns. Then a selected cluster seed on one sensor is used to build a cluster in the adjacent sensor. This enables one to compute the efficiency for each sensor. Section 7.3 discusses the use of a seagull plot to investigate cluster size, control sample noise performance and clustering in adjacent sensors to that of a

given seed.

7.1 From raw to reconstructed data

The reference pixels, as said in the previous chapter, constitute a matrix of 48×96 pixels (48 being the number of columns and 96 the number of rows), however in order to remove potential edge effects due to irregularities at the edge of the array, the first and last two rows and columns have not been taken into account when analysing data, reducing the area that can be used to a matrix of 92×44 pixels. The remaining pixels have been processed further to remove defective pixels and common mode noise, and these are discussed below.

7.1.1 Masking

Some pixels exhibit defective behaviour or are consistently noisy, as shown in Fig. 7.1, where one can see for example that some columns (13, 24, 35, ...) present a constantly high noise level and the pixel (42,15) is a dead pixel. At the top right corner of the matrix one can see that the sensor did not collect data[1]. All these effects need to be removed, through a process called *masking*, in which the defective columns and pixels were removed from the data, i.e. masked out in any further analysis.

7.1.2 Offset corrections

In electronic experiments offset corrections are needed due to the fact that even when there is no signal, a current between the pixels output and the ADC input exists. This generates an offset, called a pedestal, in the collected data and it has to be removed because it would otherwise create a bias in the analysis. The results of subtracting the pedestal values from the raw data for the first 400 events, for the following 200 events, and for the full sample is shown in Fig. 7.2, where one can see that a very similar distribution for the three possibilities is found. However, due to the fact that in some cases

[1]This issue is not yet understood at the time of writing this thesis.

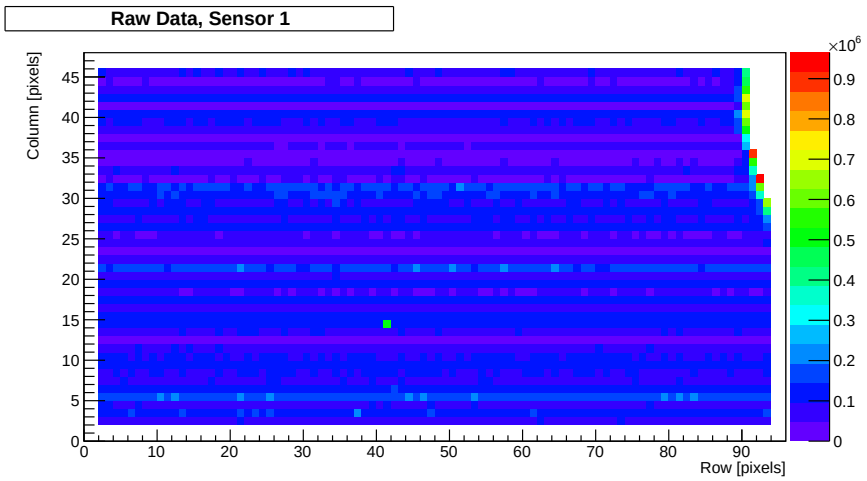

Figure 7.1: An example of raw ADC counts per pixel during one run of data acquisition for a single time frame.

we noticed that in the first few hundred events the pedestal was unstable, so we decided to omit these in the analysis in order to allow the pedestal offset to stabilise. Of the remaining events the next 200 have been considered to be representative of the run, after the pedestal was stable, and the mean ADC counts per pixel has been computed from these. In addition to this, the distribution of the noise defined as the RMS of the pedestal values is shown as an example in Fig. 7.3 for sensor 1 (standard resistivity, low noise).

7.1.3 Common mode subtraction

After masking the data and after the offset correction, an additional correction to the data was required: fluctuations in the data due to both correlated noise between different pixels on the same row and power supply variations were removed performing what is called common mode subtraction (CMS). CMS was performed evaluating the mean ADC count of each row and then subtracting this value from each pixel in the same row. Figure 7.4 shows one example of a raw data distribution, after correcting this by subtracting the pedestal value and performing the common mode subtraction the distri-

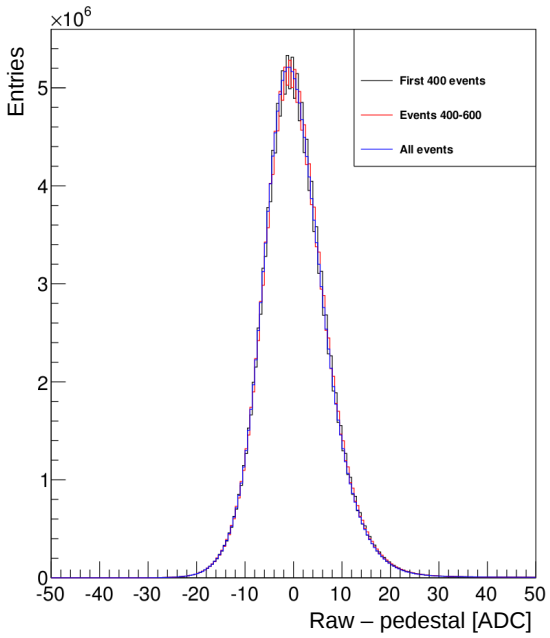

Figure 7.2: An example of pedestal values subtracted from the raw ADC counts. The first 400 events (black histogram), the sample 400-600 (red histogram), and the full data sample (blue histogram) are used to evaluate the pedestal values and this is subtracted from the raw data.

bution obtained in Fig. 7.5 was obtained together with the pull distribution shown in Fig. 7.6. The full detailed analysis performed by the ARACHNID Collaboration is available in [54].

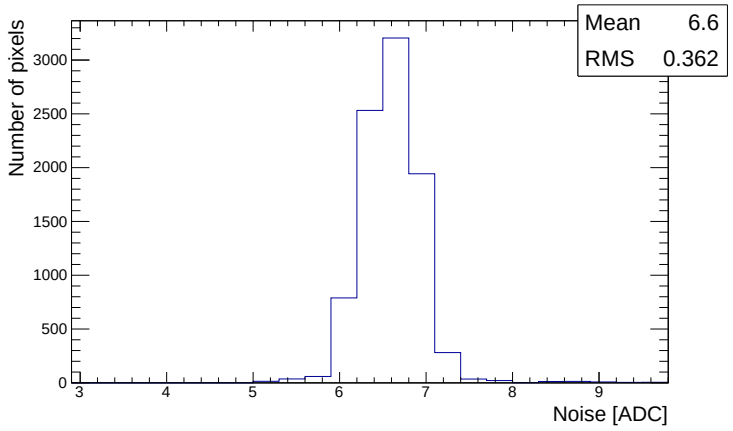

Figure 7.3: Noise distribution for sensor 1 (standard resistivity, low noise).

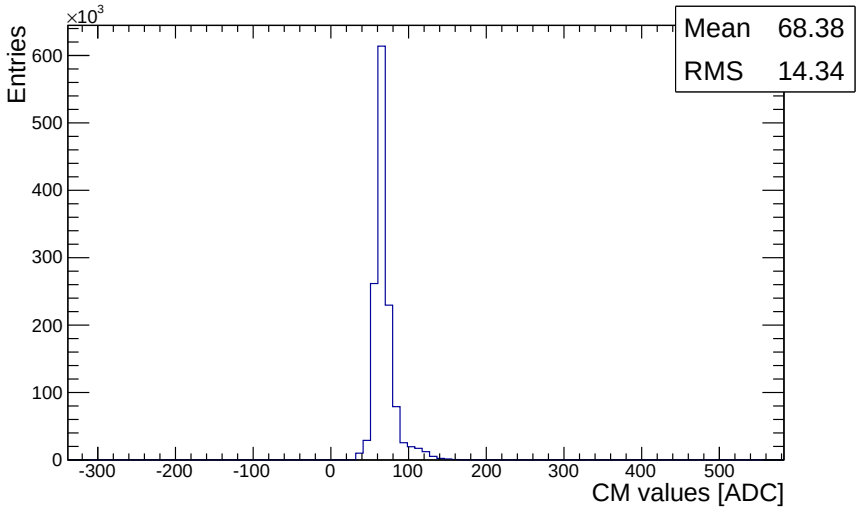

Figure 7.4: An example of the common mode distribution for sensor 1 (standard resistivity, low noise).

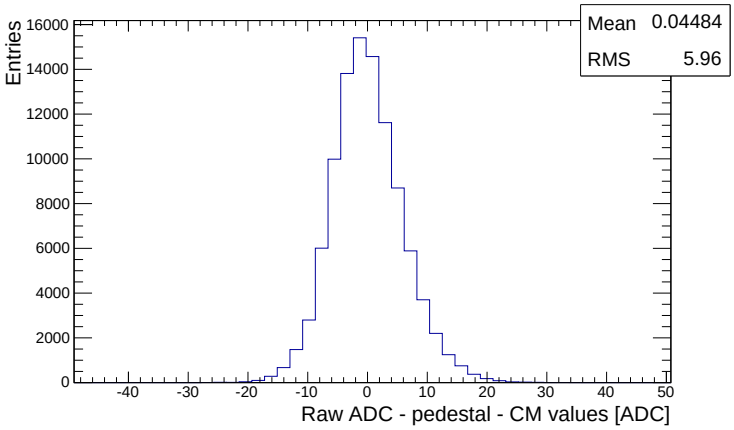

Figure 7.5: An example of the observed distribution after pedestal and common mode subtractions are applied to the raw data to sensor 1 (standard resistivity, low noise).

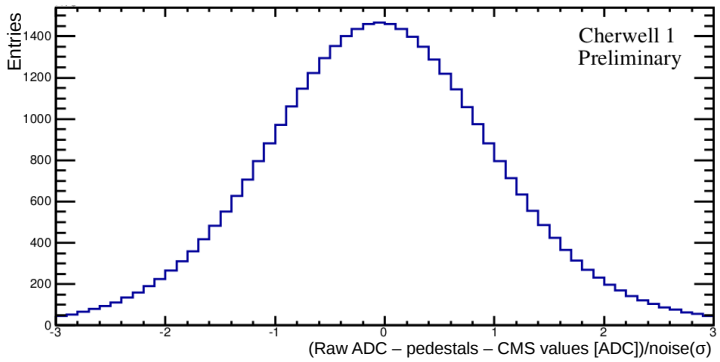

Figure 7.6: An example of the "pull" distribution obtained dividing the distribution of the corrected data by the noise.

7.2 Cluster identification

Clusters are built around a central pixel above some threshold level using the cluster model discussed in section 7.3 (Fig. 7.10). To identify the central pixel, or the cluster seed, I require a charge deposit threshold in the pixel, which typically can be of three, five or seven σ with respect to the average noise after CMS. All the pixels in the neighbourhood of the seed with a charge deposit which is less than three σ in terms of ADC counts, with respect to the average noise after CMS, are assumed to be noise and are not accounted for in the study[2]. An example of a single time frame showing hits on the sensor is shown in Fig. 7.7, where the hits are read from left to right and numbered following the left-to-right order.

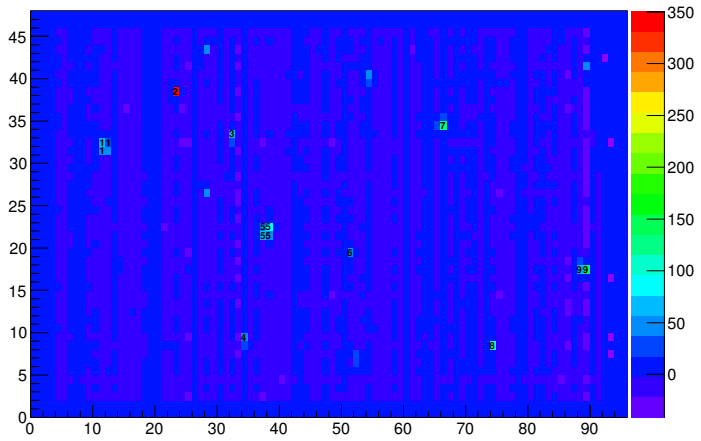

Figure 7.7: An example of a single time frame showing hits on the sensor numbered in a left-to right order. The pixels showing a number are those pixels that passed the selection criteria.

[2]This requirement is relaxed with respect to the seagull plots described at the end of this chapter, where both signal and noise fluctuations are included in the ADC count sum used to construct this plot.

After identifying each cluster I then study the distribution of the charge deposited in the cluster itself and fit it with a Landau function [55]. A comparison for all the sensors when the threshold for the seed is three, five or seven σ and the inclusion threshold for the surrounding neighbourhood pixel is fixed to three σ is shown in Fig. 7.9. A reasonable compromise between event yields and the reconstruction of the clusters is obtained when one selects a minimum threshold of five σ for the seed pixel and three σ for the neighbourhood. The main parameters of the fits are given in Table 7.3 where the most probable value (MPV),the scaling factor S, the detection efficiency, and the signal to-noise ratio are shown, the fits to the data are shown in Fig. 7.9. The scaling factor S is the full width half maximum (FWHM) of the Landau distribution which itself represents the fluctuations in the shower development in the silicon. In order to evaluate the efficiency of the various sensors an alignment algorithm described below had to be implemented prior to calculating efficiencies and studying tracking performance etc. [3]. The correlation plots shown in the previous chapter in Fig. 6.14 indicate that particles are being tracked through every sensor. By inspecting Fig. 6.14 one can see that there is an offset between the various sensors, represented by the intercept to the y-axis (the same is observed in the correlation plots of the columns, not shown). The observed offsets are a consequence of a misalignment of one sensor relative to another and need to be corrected. To perform the misalignment correction the following procedure has been applied:

- a 1 dimensional histogram equivalent to the distribution of the correlation plots has been generated. This will contain only the coordinates of the "the highest" pixels,

- to select the "highest" pixels, the location of the bin with the maximum value was identified[4],

[3]The alignment procedure and efficiency calculations have been implemented by Tamsin Nooney as main tasks of her involvement in the ARACHNID Collaboration. The procedures and results have been approved by the ARACHNID Collaboration.

[4]The common mode subtraction implemented is not working perfectly and this leads to some noisy columns and rows remaining in the data, which can misdirect the alignment

- the mean values of the maximum bin (and neighbouring bins for improved error calculations) was then used to recreate the correlation plots in a 1D histogram, which was then fitted,
- the fit is performed in terms of two free parameters; the gradient, P0, from 0 to 1, and the intercept, P1, representing the difference in position between two sensors in units of pixels (25μm),
- the results of the fit to both rows and columns are given in Table 7.1 for the rows and in Table 7.2 for the columns, respectively.

A more powerful algorithm which takes into account also the angles between sensors is currently been developed by the ARACHNID Collaboration.

Table 7.1: Results extracted from the fit to the 1D projection of the correlation plots of the rows.

Sensors	Gradient	σ_{grad}	Offset/μm	σ_{Offset}/μm
1 to 2	1	0.004	487.5	4.79
1 to 3	1	0.004	387.5	4.89
1 to 4	1	0.007	889.5	5.87
1 to 5	1	0.008	987.5	6.03
1 to 6	0.99	0.009	1073.6	6.36

These offsets have been used to correct the mechanical alignment of the six sensor planes relative to the the first sensor in the stack, for example, if one looks at Fig. 7.8, the top histogram shows an event for sensor 1 and the histogram at the bottom shows the same event for sensor 2 where a threshold of 5σ was required for the seed pixel and an inclusion threshold of 3σ was required for the neighbour pixels. Applying the correction coefficients from sensor 1 to sensor 2 as shown in Table 7.1 and in Table 7.2, when considering

algorithm to follow noise rather than true particle hits. This was temporarily overcome by identifying not only the location of the maximum bin, but also looking in the two bins either side of the selected bin and finding the location of the maximum bin in both of these.

Table 7.2: Results extracted from the fit to the 1D projection of the correlation plots of the columns.

Sensors	Gradient	σ_{grad}	Offset/μm	σ_{Offset}/μm
1 to 2	1	0.003	-48.7	5.48
1 to 3	1	0.003	556.0	6.65
1 to 4	0.99	0.005	531.3	6.55
1 to 5	1	0.005	559.2	6.69
1 to 6	1	0.006	637.0	13.1

the hit indicated by a yellow circle on sensor 1 with the centroid coordinates in terms of pixels being (12,32), then one would expect to find a hit in sensor 2 with the position of centroid in (31,30) if the hit is due to a beam particle, as shown in the bottom histogram of Fig. 7.8. This particular event is given as an example.

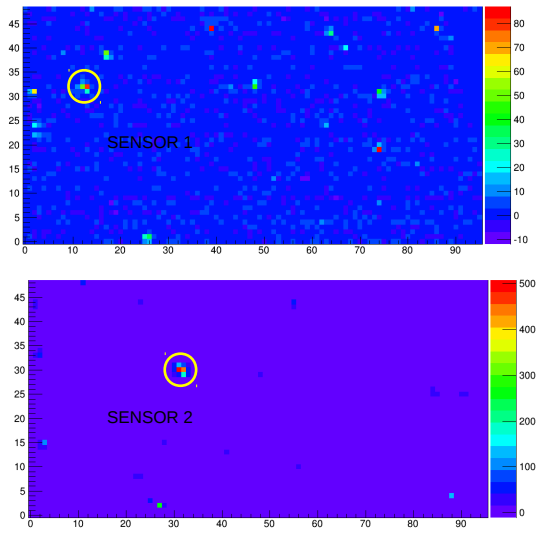

Figure 7.8: An example of a single time frame showing hits on the sensor numbered in a left-to right order. The pixels showing a number are those pixels that passed the selection criteria.

As reported by Tamsin Nooney, despite the careful alignment of the sensors using the X-Y stage as described in the previous chapter, the alignment coefficients increase to relatively large distances throughout the stack, such that the offset between the first and the last sensor precludes half the last sensor being used in the analysis.
To calculate the efficiency, the centroid of each cluster was calculated by weighting the position according to the signal, as follow

$$x = \frac{\sum_{i=1}^{Events} ADC_i \times x_i}{ADC_i}, \tag{7.1}$$

$$y = \frac{\sum_{i=1}^{Events} ADC_i \times y_i}{ADC_i}. \tag{7.2}$$

The efficiency of each sensor was then calculated using two other sensors as a double coincidence trigger and looking for a correlation of clusters seen in the trigger system with the detection of a cluster in the sensor under study. Explicitly, if a cluster was found in the two reference sensor planes within 5 pixels of the centroid of each other, then a corresponding cluster was expected in the third test sensor. Hence, the detection efficiency is a parameter of a binary distribution, whereby the number of clusters found in the reference system is counted as N_{tot} and the number successfully found within all three sensors, N_{succ}. The efficiency, ϵ, is given by:

$$\epsilon = \frac{N_{succ}}{N_{tot}}, \tag{7.3}$$

and the error on the efficiency is given by

$$\sigma_\epsilon = \sqrt{\frac{\epsilon(1-\epsilon)}{N_{tot}}}. \tag{7.4}$$

The values of the efficiency observed for each sensor are given in Table 7.3, while the the value of σ_ϵ has been found to be of the order of 10^{-3} for all the sensors. Looking at Table 7.3 one can see that sensor 2 (standard resistivity, low noise) and sensor 4 (standard resistivity, standard noise) show the best signal-to-noise ratio (or MPV/N), and sensors 3 and 5 (both high resistivity, low noise) smaller fluctuations in the shower development (the parameter S)

are observed, and for all the sensors the MPV increases as the seed threshold increases. In the next session I show the seagull analysis for both beam and noise, however the contribution of the noise still does not help describing the the behaviour observed in the MPV as shown in Table 7.3.

Table 7.3: Main fit parameters for the charge deposited in a cluster when different thresholds are applied to the cluster seed for the selection of the cluster itself with an inclusion threshold of three σ for the cluster seed neighbourhood pixels.

Sensor	Seed inclusion Threshold	MPV (ADC)	S (ADC)	Noise (ADC)	efficiency (%)	MPV/N
Sensor 1	3σ	60.9	30.45	6.5	99.9	9.3
	5σ	83.8	26.09	6.5	99.9	12.8
	7σ	109.6	46.2	6.5	99.7	16.8
Sensor 2	3σ	44.1	25.9	2.9	99.9	15.5
	5σ	61.6	22.0	2.9	99.9	21.4
	7σ	84.61	32.2	2.9	99.7	29.2
Sensor 3	3σ	7.9	7.9	2.6	99.9	3.0
	5σ	26.3	9.1	2.6	99.9	10.1
	7σ	28.7	15.2	2.6	99.8	11.0
Sensor 4	3σ	30.4	21.4	3.0	99.8	10.1
	5σ	52.2	22.3	3.0	99.7	17.4
	7σ	77.6	24.6	3.0	99.7	25.9
Sensor 5	3σ	7.7	7.3	2.6	99.9	3.0
	5σ	24.4	8.8	2.6	99.9	9.4
	7σ	28.8	13.8	2.6	99.9	11.1
Sensor 6	3σ	42.7	20.6	5.0	99.8	8.54
	5σ	66.2	28.7	5.0	99.8	13.2
	7σ	85.4	36.8	5.0	99.7	17.8

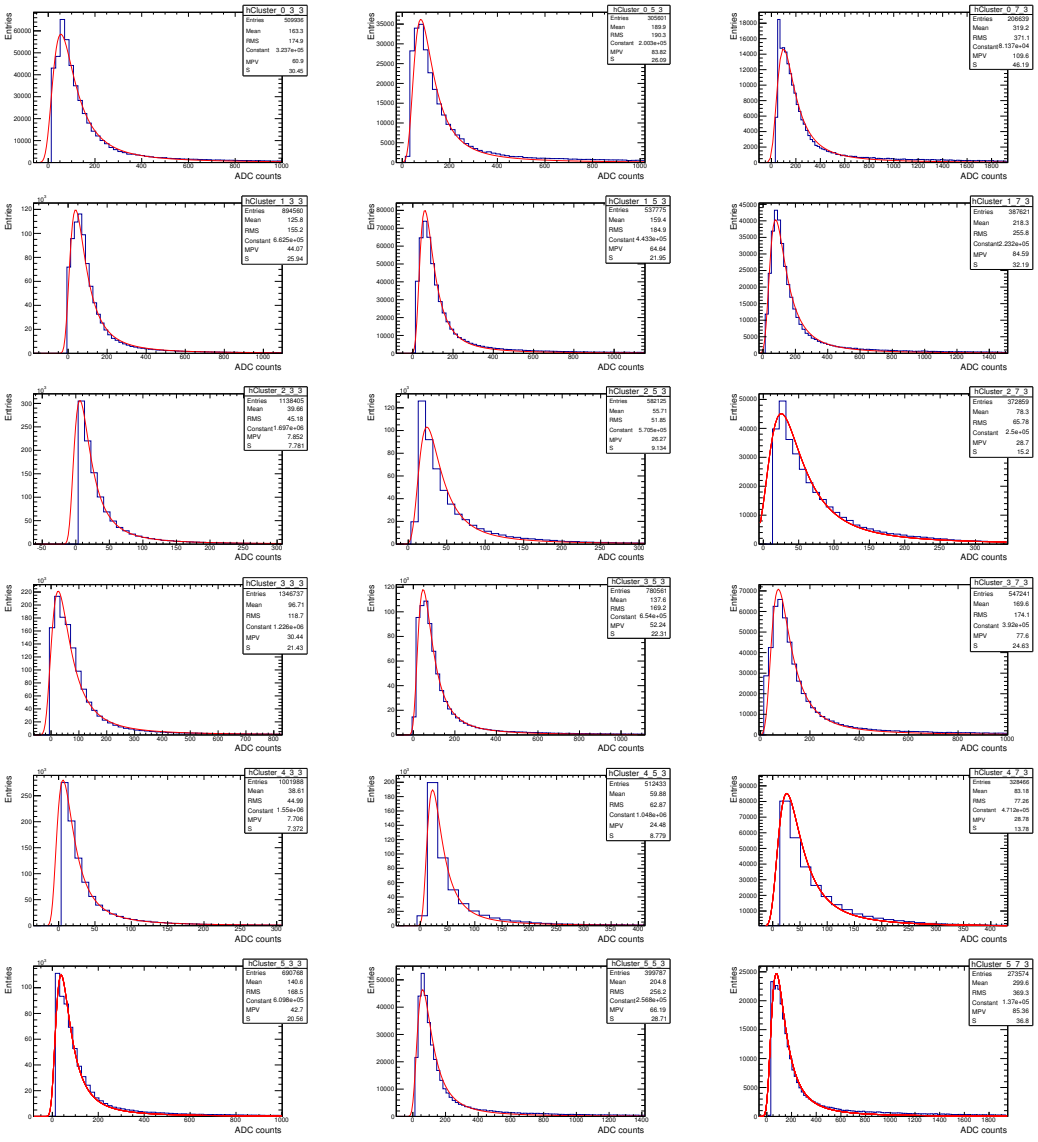

Figure 7.9: Distributions of the charge deposited in the clusters. Histograms are called hCluster followed by a sequence of numbers i, j, k, where i indicates the sensor number (being 0 the first and 5 the sixth sensor, respectively), j the charge deposit threshold required for the seed and k is the charge deposit threshold required for the pixels surrounding the seed pixel.

7.3 Cluster properties: seagull plots

To evaluate the size of a cluster in terms of pixels I have performed an analysis called a seagull analysis, used to generate seagull plots. Seagull plots contain all the required information to estimate the size of a cluster [56] [57] [58]. The analysis consists of the identification of the seed pixel as previously discussed, and the study of the surrounding pixels in the neighbourhood of the seed. The algorithm described below is designed to show the increase in signal as a function of the cluster size (in pixels). Any apparent decrease in signal observed in a seagull plot corresponds to adding a negative noise fluctuation to the sum of signal collected. To find a cluster, first I select the cluster seed requiring a 5σ threshold with respect to the average noise after CMS. As shown in Fig. 7.10, I then consider two possible matrices of pixels having the seed at the centre: a 3×3 matrix in which the seed pixel is surrounded by an 8 pixel ring and a 5×5 matrix in which the seed pixel is surrounded by 24 pixels. The seagull plots are obtained studying the charge deposited in the pixels of the 3×3 and 5×5 matrices. The seagull plot consists of two parts or sides (the wings of the seagull): the 3×3 matrix contains the information shown on the left part of the plot (the left wing of the seagull), the 5×5 matrix contains information that will be used for the right side of the plot (the right wing of the seagull).

Seagull Plot Algorithm: "left wing"

1) find a seed pixel

2) generate 25 different "Landau" seagull histograms

3) fill the first Landau seagull histogram with the signal of the cluster seed

4) order the surrounding 8 pixels from high to low signal as shown in Fig. 7.10 (left)

5) fill the second Landau seagull histogram with the sum of the cluster seed signal and the signal of the next highest pixel signal from the eight pixels surrounding the cluster seed

6) fill the third Landau seagull histogram with the sum of the signal of the cluster seed, the signal of the next highest pixel signal from the eight pixels surrounding the cluster, and the signal of the second highest pixel signal from the eight pixels surrounding the cluster.

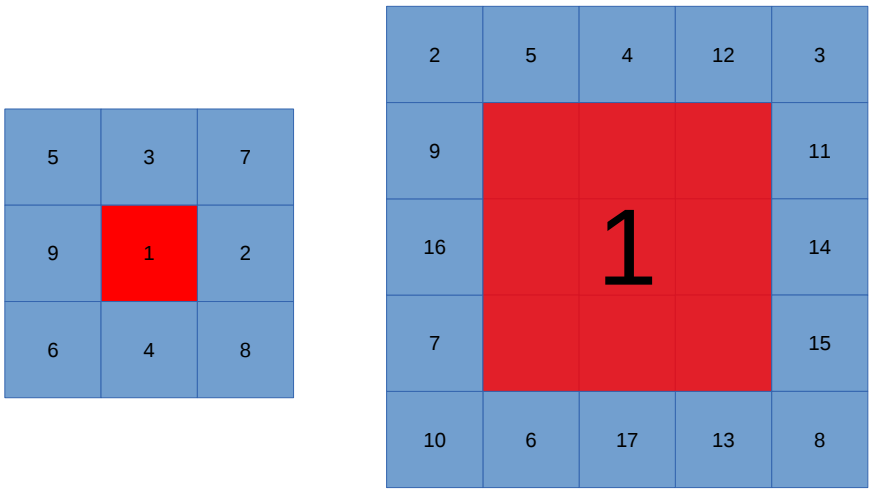

Figure 7.10: Cluster modeling. (left) A 3×3 matrix in which the seed pixel is surrounded by 8 pixels and (right) a 5×5 matrix in which the seed pixel is surrounded by 24 pixels. The second matrix can be seen as a "big" (3×3) pixel surrounded by 16 pixels.

The procedure is then repeated until the full ring of 8 pixels surrounding the seed is processed. As an example, the histograms obtained for sensor 3 (high resistivity, low noise) are shown in Fig. 7.11 and are fitted with a Landau function with main parameters given in Tab. 7.4. If one plots the number of pixels considered versus the MPV of the Landau functions extracted from the data one obtains the "left wing" of the seagull plot in terms of the relative intensity of each contribution.

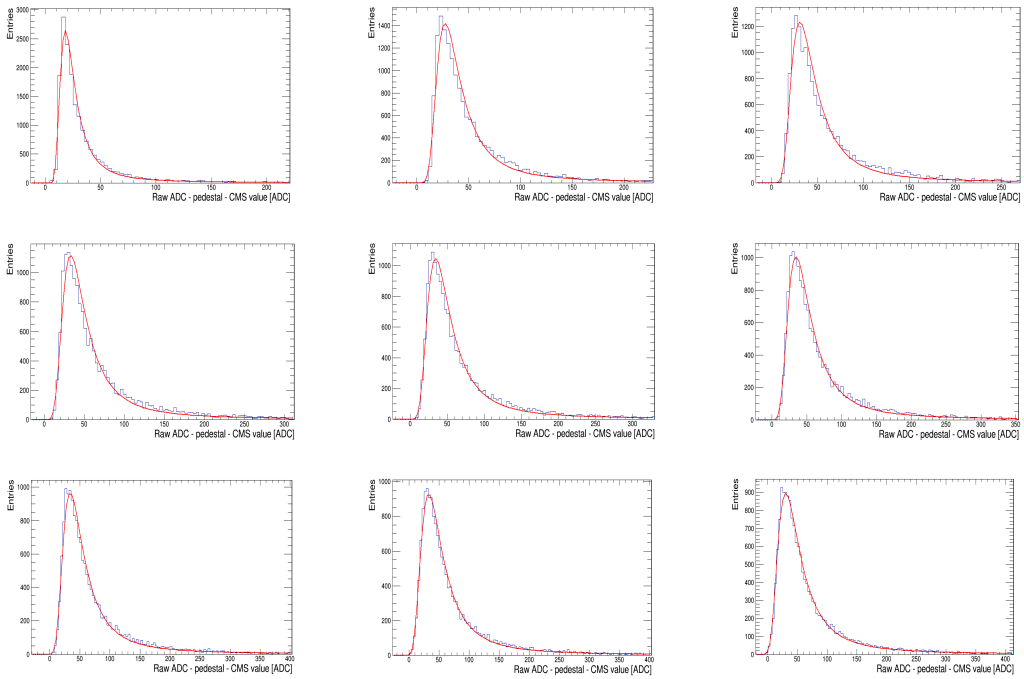

Figure 7.11: Landau seagull histograms obtained for the 3×3 matrix of pixels containing the seed in the centre. They are arranged as follows: the top-left seagull histogram contain the signal of the cluster seed, the top-centre histogram contains the sum of the seed with the higher signal from the surrounding 8 pixels, and so on. The bottom-right seagull histogram contain the sum of all the signal (and noise) contained in the 3×3 matrix of pixels.

Table 7.4: Main parameters extracted from the fit to the Landau seagull histograms for a 3×3 matrix of pixels corresponding to the left wing of the seagull plot for sensor 3 (high resistivity, low noise).

Seagull	MPV (ADC)	S (ADC)
hist. 0	18.9	4.4
hist. 1	27.4	7.4
hist. 2	32.7	8.5
hist. 3	35.0	9.4
hist. 4	36.4	10.2
hist. 5	36.8	10.6
hist. 6	36.5	11.2
hist. 7	35.3	11.7
hist. 8	32.9	12.1

To obtain the right wing of the seagull one has to apply a similar procedure to the ring surrounding the 3×3 matrix containing the cluster seed.

Seagull Plot Algorithm: "right wing"

1) The 3×3 matrix of pixels used to obtain the left side (left wing) of the seagull plot described above is now considered as a single pixel, in particular it is considered as a cluster seed or as a matrix seed.

2) order the 16 pixels surrounding the new seed (the 3×3 matrix) from high to low signals as shown in Fig. 7.10 (right)

3) Fill the the tenth Landau histogram with the sum of the total signal of the 3×3 matrix and the signal of the first "higher" pixel signal from the sixteen pixels surrounding the 3×3 matrix.

4) Fill the eleventh Landau histogram with the sum of the total signal of the 3×3 matrix, the signal of the higher pixel signal from the sixteen pixels surrounding the 3×3 matrix, and the signal of the second higher pixel signal from the sixteen pixels surrounding the 3×3 matrix.

The procedure is then repeated until the full ring of 16 pixels surrounding the central 3×3 matrix is processed. These histograms are shown in Fig. 7.12 and are fitted with a Landau function; from each of these one extracts the MPV (the main parameter extracted from the fit are given in Tab. 7.5) as done for the "left wing" to plot it as function of the number of pixels considered, in the right side of the seagull plot.

Table 7.5: Main parameters extracted from the fit to the Landau seagull histograms for the seed matrix and for the ring of 16 pixels surrounding the 3×3 seed matrix for sensor 3 (high resistivity, low noise).

Seagull	MPV (ADC)	S
hist. 8	32.9	12.1
hist. 9	37.9	12.9
hist. 10	40.8	13.3
hist. 11	42.6	13.4
hist. 12	44.0	13.6
hist. 13	44.9	13.8
hist. 14	45.4	13.9
hist. 15	45.7	14.1
hist. 16	45.7	14.3
hist. 17	45.3	14.4
hist. 18	44.7	14.6
hist. 19	43.9	14.8
hist. 20	42.6	14.9
hist. 21	41.0	15.0
hist. 22	38.8	15.1
hist. 23	36.2	15.4
hist. 24	32.8	15.6

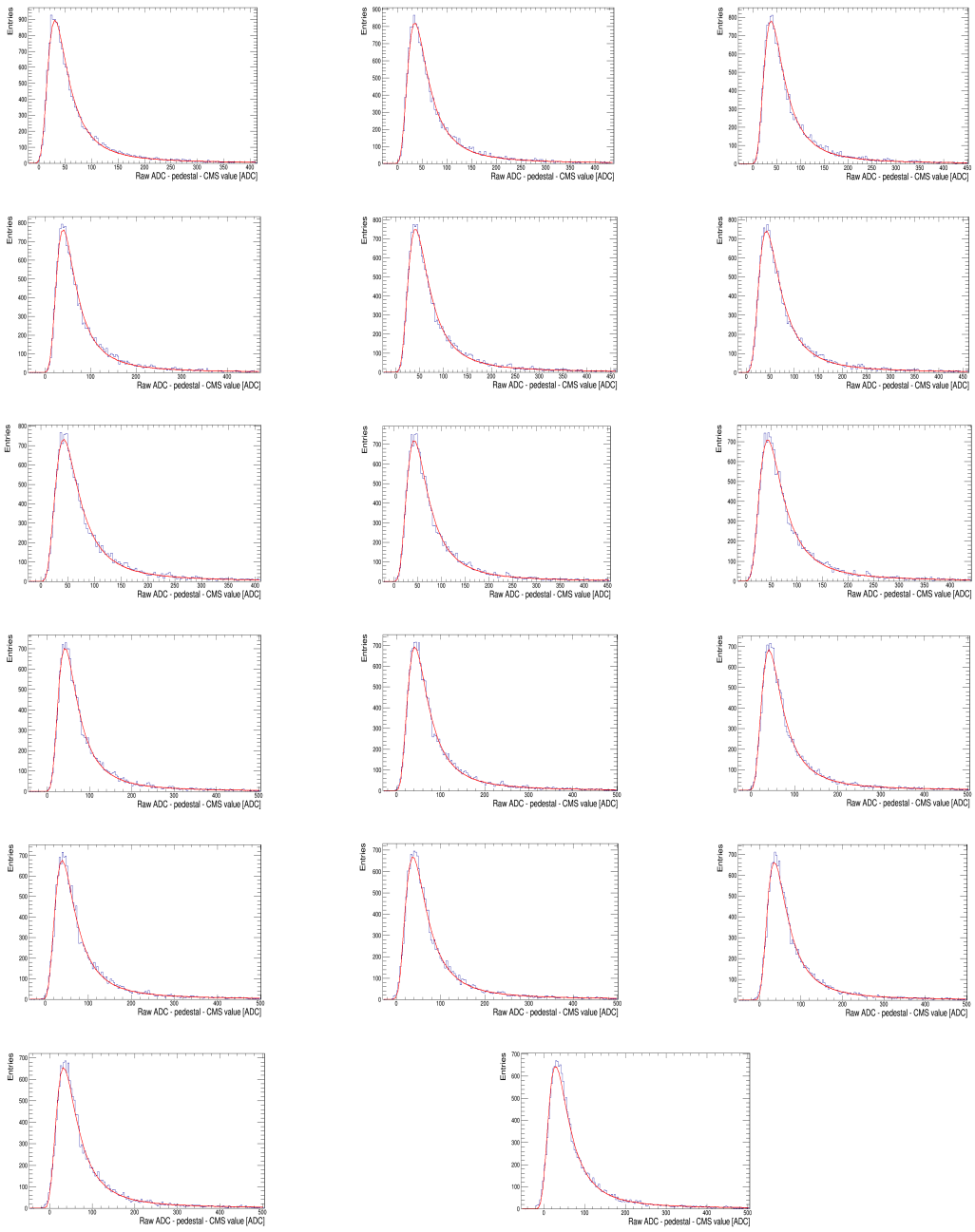

Figure 7.12: Landau seagull histograms obtained for the 3×3 seed matrix of pixels and the surrounding 16 pixels. These are arranged as follows: the top-left seagull histogram contain the signal of the matrix seed, the top-centre histogram contains the sum of the matrix seed with the higher signal from the surrounding 16 pixels, and so on. The bottom-right seagull histogram contain the sum of all the signal (and noise) contained in the ring of 16 pixels for sensor 3 (high resistivity, low noise).

If one considers an ideal sensor without noise, then the seagull plot would represent the charge deposited from the highest to the lowest measured pixel value. This signal only contribution would be evident by a sharp increase in the relative intensity plotted as a function of the cluster size, and would plateau once all charge had been collected. In this scenario the optimal cluster size would be indicated by the onset of the plateau region. Any additional pixels added to the cluster beyond that threshold would not add any information. In reality one has to consider noise, and so one can balance the ideal expectation with the other extreme of what would happen in the total absence of a signal, i.e. the noise dominated regime, where one would have to relax the 5 sigma seed constraint. Instead of the Landau seagull distributions of Fig. 7.11 and Fig. 7.12, over time each pixel would record Gaussian distributions corresponding to electronic noise after pedestal and CMS correction, like that shown in Fig. 7.5. The noise contributions would be ranked from largest to smallest values in the inner 3x3 and outer 5x5 rings of pixels. As a result a seagull plot of only noise would show a slight rise over the first 4 or five bins, with a corresponding fall off. This corresponds to measuring noise fluctuations in rank order from highest to lowest values. On average one would expect the positive fluctuations to be washed out by the negative ones. A similar pattern should be seen for the outer ring (the right side of the seagull plot). In reality we have neither of these two extreme cases, rather a combination of the signal and noise. So we expect a seagull plot to start rising on the left size and if the signal is contained completely within the inner 3x3 array, then we would expect no additional signal to be accumulated when adding the outer pixels so that the 9th and 25th bins would have the same content. A test to check that what was observed was due to signal was performed. In particular a "control region" far from the selected pixels (those above the required threshold) was chosen; in this region, in absence of signal one would expect to observe Gaussian distributions corresponding to electronic noise after pedestal and CMS corrections similar to the one shown in Fig. 7.5. A 3×3 matrix of pixels containing only noise was selected and the observed distributions for this non-signal region are shown in Fig. 7.13 for sensor 3, and the main parameters extracted from the the Gaussian fit for the same sensor are given in Tab. 7.6.

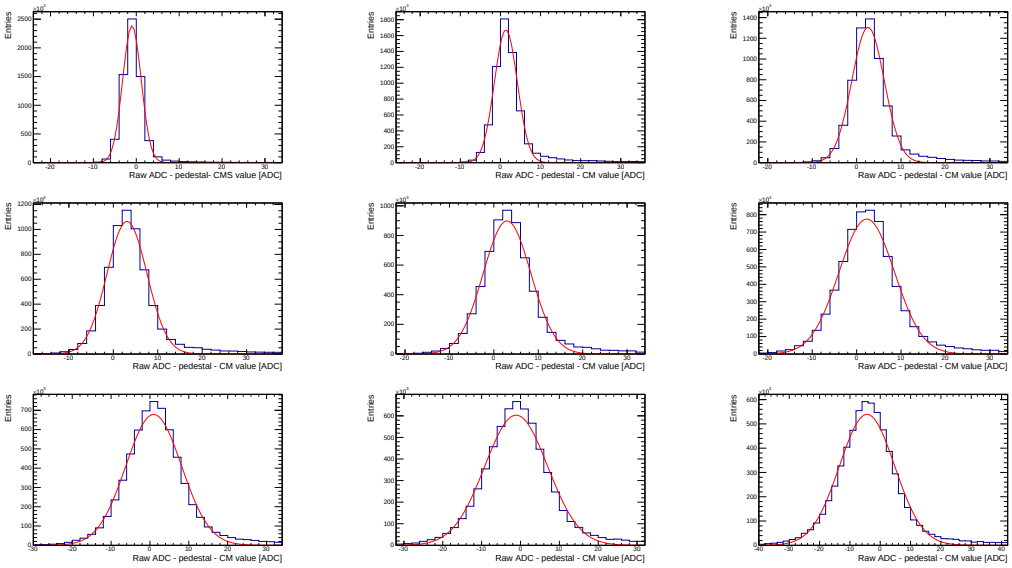

Figure 7.13: Gaussian seagull histograms obtained for the 3×3 matrix of pixels in the control region. They are arranged as follows: the top-left seagull histogram contains the "signal" of the central pixel, the top-centre histogram contains the sum of the seed with the higher signal from the surrounding 8 pixels, and so on. The bottom-right seagull histogram contains the sum of all the signal (and noise) contained in the 3×3 matrix of pixels for sensor 3 (high resistivity, low noise).

Table 7.6: Main parameters extracted from the fit to the Gauss seagull histograms for a 3×3 matrix of pixels in the control region corresponding to the left wing of the seagull plot for sensor 3 (high resistivity, low noise).

Seagull	μ (ADC)	σ_s (ADC)
hist. 0	-1.2	2.2
hist. 1	1.4	2.8
hist. 2	2.4	3.6
hist. 3	3.0	4.5
hist. 4	3.0	5.4
hist. 5	2.8	6.3
hist. 6	0.9	7.2
hist. 7	-1.1	8.1
hist. 8	-4.3	9.1

7.3.1 Seagull plots

The results of the full seagull analysis are shown in Fig. 7.14 where, referring to the letter classification of the previous chapter for the different sensors, the black data points indicate the standard resistivity wafer with low noise implant previously indicated as 1A, the red data points indicate the standard resistivity wafer with low noise implant 2A, the green data points indicate the high resistivity wafer with low noise implant 3B, the dark purple data points indicate the standard resistivity wafer with standard noise implant 4C, the blue data points indicate the high resistivity wafer with low noise implant 5B, and the light purple data points indicate the standard resistivity wafer with standard noise implant 6C. The seagull plots contain information

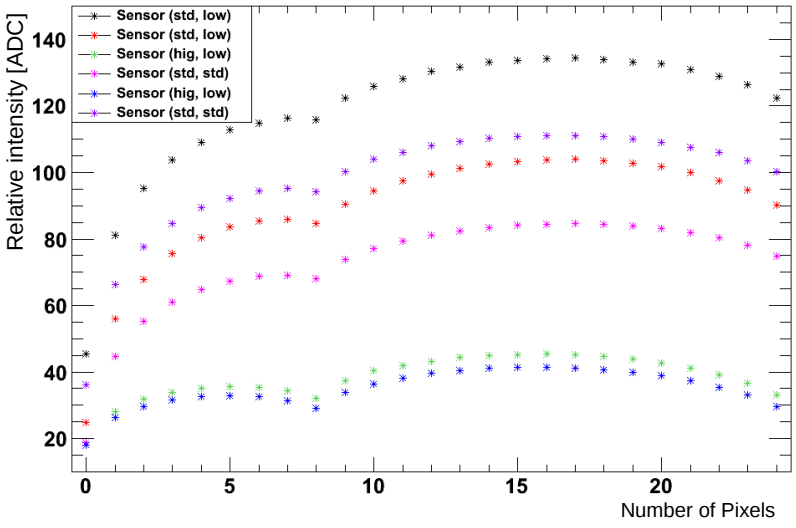

Figure 7.14: Seagull plots for the six tested Cherwell sensors, where the clusters have been selected requiring a 5σ inclusion threshold for the central seed, showing that charge is collected in the seed and in the first ring of pixels surrounding it.

about the cluster and about properties of the sensors. Looking at the two

wings separately, the left rise in the wing is due to signal plus noise while the right fall off is only due to noise [56] [57] [58]. If in the right wing there is a substantial rise with respect to the left one that means that the second ring contains useful information in terms of signal. On the other hand if in the right wing there is no substantial rise and the first and last point (of the second ring only) are at the same MPV value, it means that, since the rise is due to signal plus noise and fall is only due to noise, there is no substantial information contained in the second ring, and the cluster can be well identified by the first 3×3 matrix given by the the seed pixel and the 8 pixels ring around it.

We conclude, by examining the results, that the clusters can be described well by a 3×3 matrix of pixels. One can also learn something about the charge distribution, or charge spread, among the pixels from the seagull plots. In fact, if one looks at Fig. 7.14 on the left wing, then it can be seen that in standard resistivity sensors (for example the black and red data points) the charge is spread between more pixels, reaching the maximum of charge collection at a point corresponding to eight pixels, than required for the high resistivity sensors (blue and green data points), where the maximum charge collection is reached in five pixels. The same analysis has been performed in the control region and the results are shown in Fig. 7.15, where as expected for a region in which no signal is present no net gain in the sensors is observed. Figure 7.15 clearly show that a bias is introduced in the analysis in the CMS procedure; this can explain the negative values. The Arachnid Collaboration had agreed upon the CMS procedure adopted here, however in light of this work the Collaboration may want to revisit the CMS procedure to remove the effect of signal greater than 5σ when computing the offset corrections to minimise possible bias. A final test to check that the observed signal in the clusters is due to beam particles has been performed. After the identification of clusters in each sensor, the relative alignment of each sensor, determined using the method outlined in section 7.2, is applied in order to extrapolate the hit position from a given sensor into an adjacent one. If after applying this corrections a hit is seen in all the sensors in a range of $\pm$ 5 pixels (equivalent to 125 μm) from the expected position, then the event is stored for the seagull analysis and considered as a signal event due to the beam hitting

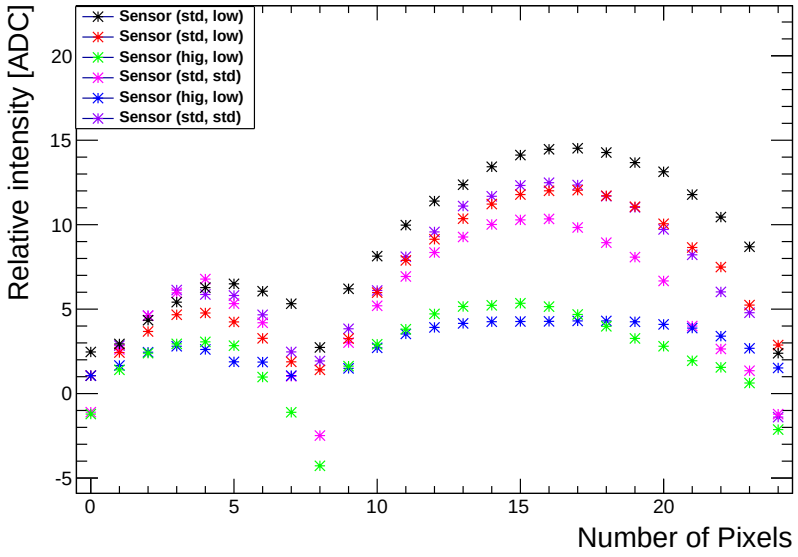

Figure 7.15: Seagull plots for the six tested Cherwell sensors in the only noise control region.

the sensors. If one considers that an online triple coincidence trigger has been required to collect data as described in previous chapter (see Fig. 6.15), then it is reasonable to assume that all the data stored are due to the beam of particles hitting the two front scintillators, the six sensors, and the back scintillator. In this case, when requiring that a hit is seen two adjacent sensors within the defined range from the expected position, and then using a seed position from an adjacent sensor to make the seagull plot one would expect to obtain a plot that looks exactly as the one shown in Fig. 7.14. This additional analysis has been performed and the resulting seagull plots are shown Fig. 7.16. The similarity of Figs. 7.16 and 7.14, along with the high efficiencies tabulated in Tab. 7.3 prove that the cluster seed positions used to construct the seagull plots are from beam particles, rather than noise. This is also highlighted by the contrasting shape of the seagull plot shown in Fig. 7.15 for a control region away from a cluster seed above threshold.

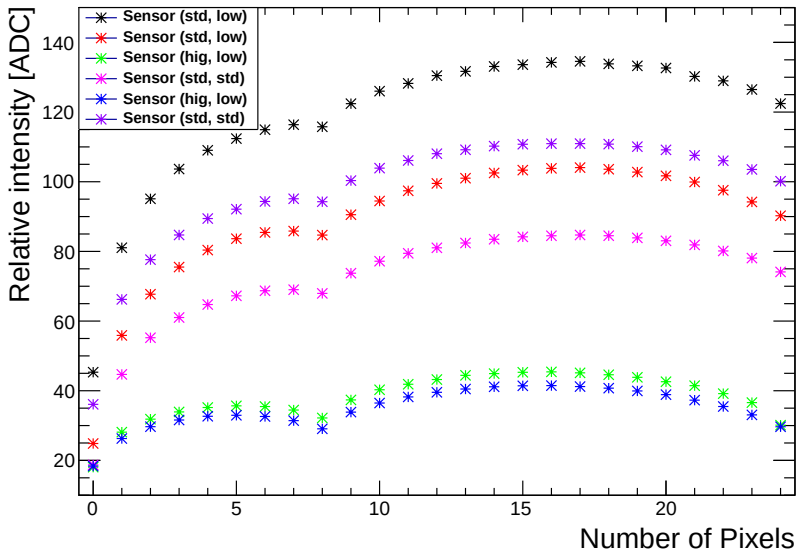

Figure 7.16: Seagull plots for the six tested Cherwell sensors, where the clusters have been selected requiring a 5σ inclusion threshold for the central seed, with the each hit required to be seen in all the sensors within a range of 125 μm from the expected position.

Chapter 8

Conclusions

Time-dependent CP violation in charm decays can provide very important information that can be used to test the flavour structure of the standard model. I have shown how a time-dependent measurement can be used to measure ϕ_{MIX} and to constrain $\beta_{c,eff}$ when one ignores penguin contributions or when these can be controlled and understood[1]. Additional theoretical work is required , in particular due to the lack of understanding of penguin contributions in $D^0 \to K^+K^-$. I have shown the predictions on the expected sensitivities of ϕ_{MIX} and $\beta_{c,eff}$ of a numerical analysis (Chapter 2). Subsequently a more refined analysis was then implemented considering a potential run at the charm threshold of the (now cancelled) Super$B$ experiment, for which the decay chains

$$e^+e^- \to \Psi(3770) \to (D^0)(\overline{D}^0) \to (K^-e^+\nu_e)(K^+K^-),$$
$$e^+e^- \to \Psi(3770) \to (\overline{D}^0)(D^0) \to (K^+e^-\overline{\nu}_e)(K^+K^-),$$
$$e^+e^- \to \Psi(3770) \to (D^0)(\overline{D}^0) \to (K^-e^+\nu_e)(\pi^+\pi^-),$$
$$e^+e^- \to \Psi(3770) \to (\overline{D}^0)(D^0) \to (K^+e^-\overline{\nu}_e)(\pi^+\pi^-),$$

have been studied assuming a machine configuration with a boost factor $\beta\gamma = 0.28$. I have shown that it is possible to correctly reconstruct masses, decay vertices, and decay time distribution for all the decays, with selection criteria based on the properties of the beam constrained mass M_{BC} and ΔE.

[1]If one assumes U-spin symmetry then this statement can be relaxed as the penguin pollution in KK and $\pi\pi$ modes should be equal. However it should also be noted that U-spin is broken at the 20% level in these decays hence this assumption may not be valid for large penguin pollution.

The observed time distribution Δt has been used to evaluate detector effects by constructing the so called resolution function. A Monte Carlo RooFit-based study has then been performed to evaluate the precision obtainable for the parameter $\beta_{c,eff}$. This refined study highlights the need to consider detector resolution carefully when making statements about achievable precision. In particular we predicted a resolution of 3.3° when collecting 1.0 ab^{-1} of data at the charm threshold when performing flavour tagging using semileptonic D^0 decays, and 1.4° when combining yields from semileptonic tagged D^0 mesons with K tagged D^0 mesons and we found a precision of 13.6° for the low boost configuration ($\beta\gamma = 0.28$). Several factors play a role here. First I considered only the four semileptonic $\overline{D}^0$ (D^0) decays with an electron (positron) in the final state, while considering the semileptonic $\overline{D}^0$ (D^0) decays with a muon (antimuon) in the final state would have doubled the yields, improving our sensitivity by a factor $\sqrt{2}$. Second, the numerical estimate of the resolution did not account for the time resolution of the detector, that due to the short lifetime of the D^0 mesons of 0.41 ps becomes of paramount importance. A boost factor $\beta\gamma = 0.28$, even if it allows one to nicely perform time-dependent measurements in the D system as done in the past at B factories for B mesons, does not allow one to obtain a high resolution on the decay vertices of the D^0 mesons, and in turn translates in a poor resolution on Δt. This problem however does not affect D^0 mesons which are produced in a hadron machine where the D^0 mesons are produced both promptly and as decay products of b-hadron decays, or in an asymmetric energy e^+e^- collider running at the cms energy equivalent to that of the $\Upsilon(4S)$ where the D^0 mesons are produced in the decay of boosted B mesons or from $c\bar{c}$ continuum. For an asymmetric e^+e^- collider running at the charm threshold, a better resolution on Δt can be obtained by changing the machine parameters to achieve a larger $\beta\gamma$ factor, for example $\beta\gamma = 0.5$-0.9, and improving the vertexing/tracking detector technologies by obtaining detectors that can operate closer to the beam pipe, i.e. requiring higher radiation hardness and higher granularity to improve the resolution. For the boost option $\beta\gamma = 0.9$ it has been found that one might measure (constrain) $arg[\lambda_f(D^0 \to \pi^+\pi^-)] = \phi_{\pi\pi}$ with a precision $\sigma_{\phi_{\pi\pi}} = 6.7°$ which is equivalent to a precision $\sigma_{\beta_{c,eff}} = 3.4°$ on $\beta_{c,eff}$.

A new type of vertexing/tracking technology is represented by the Cherwell chip, currently under study within the ARACHNID Collaboration. We tested the Cherwell sensor at CERN using a 120 GeV/c pion beam delivered as secondary beam from the 450 GeV/c SPS proton beam impinging on a primary target. The technology is quite suitable for use in a tracking system and the possibility to use high resistivity epitaxial layers would improve the radiation hardness, allowing the sensor to be placed in relatively high radiation environments such as the region around a beam pipe in an e^+e^- collider, for example within 1.0 cm from the interaction point. I studied how the charge deposit due to charged particles passing through the sensors can be reconstructed as clusters, finding that all the information in terms of charge deposit/spread is collected inside an eight pixel ring surrounding the central seed pixel (each pixel being 25×25 μm). This work also showed that high resistivity epitaxial layers reduce the charge spread through the sensor allowing the charge deposited to be typically collected by 5 pixels, and that the efficiency calculated for all the types of Cherwell sensor is high ($\geq 99.7\%$), which agrees with the official ARACHNID efficiency study performed by T. Nooney. The ARACHNID work on the Cherwell chip has been developed further by CERN/RAL TD for use in ALICE inner tracker upgrade at the LHC.

Appendix A

A.1 $e^+e^- \rightarrow \Psi(3770) \rightarrow (D^0)(\overline{D}^0) \rightarrow (K^-e^+\nu_e)(K^+K^-)$

The study discussed in Chapter 4 has been applied to the decay chain $e^+e^- \rightarrow \Psi(3770) \rightarrow (D^0)(\overline{D}^0) \rightarrow (K^-e^+\nu_e)(K^+K^-)$, this being the charge conjugate chain of $e^+e^- \rightarrow \Psi(3770) \rightarrow (D^0)(\overline{D}^0) \rightarrow (K^+K^-)(K^+e^-\overline{\nu}_e)$. The Final distributions obtained after the selection criteria given in Tab. A.1 have been applied to the 380000 generated events of $e^+e^- \rightarrow \Psi(3770) \rightarrow (D^0)(\overline{D}^0) \rightarrow (K^-e^+\nu_e)(K^+K^-)$ are shown in Fig. A.1, for which an efficiency $\epsilon = 53.9\%$ was found, in agreement with what was observed in the decay chain $e^+e^- \rightarrow \Psi(3770) \rightarrow (D^0)(\overline{D}^0) \rightarrow (K^+K^-)(K^+e^-\overline{\nu}_e)$, where an efficiency $\epsilon = 53.8\%$ was found. Figures A.2-A.6 show the distributions of the central values, the errors, and the pull on the errors, obtained from the RooFit study of the resolution function and Fig. A.7 shows the distributions of the central value, the errors, and the pulls for $\phi = arg[\lambda_f]$, showing a sensitivity on the latter $\sigma_\phi = 12.32°$, in agreement with that obtained for the conjugate decay chain where $\sigma_\phi = 12.6°$ was found, see Fig. 5.16.

Table A.1: Allowed range of values for ΔE, M_{BC}, $\sigma_{\Delta t}$ and χ^2.

Parameter	min.	max.
ΔE $[GeV]$	-0.01	0.01
M_{BC} $[GeV]$	1.8605	1.868
$\sigma_{\Delta t}$ $[ps]$	-	10.0
χ^2	-	15

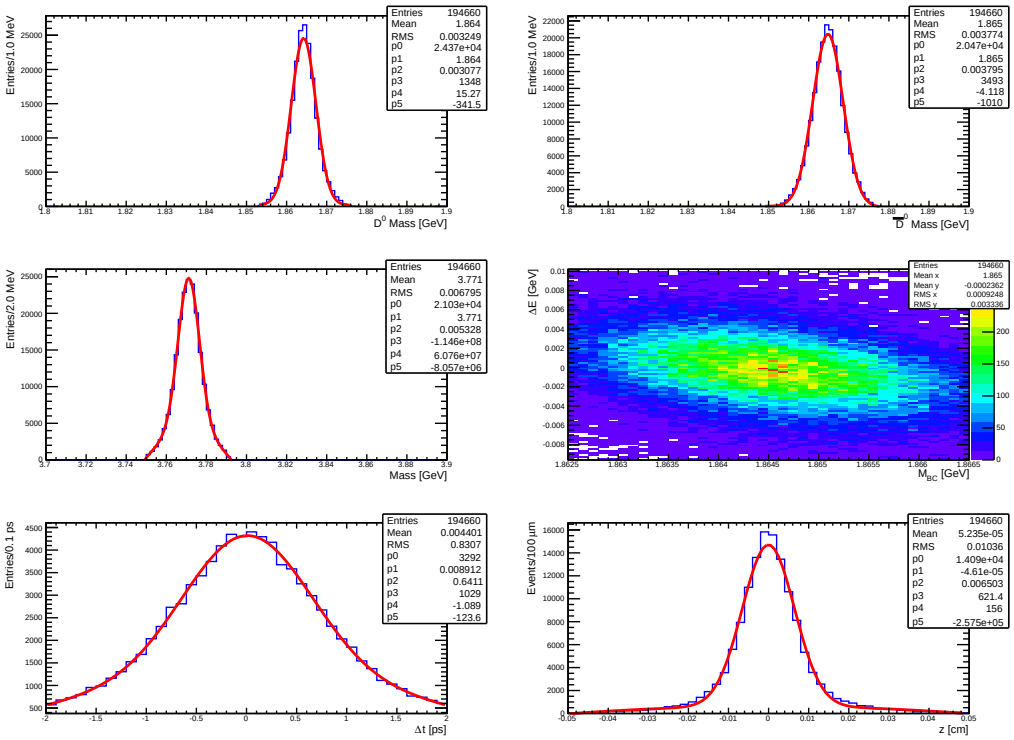

Figure A.1: Final distributions obtained after selection criteria have been applied to the 380000 generated chains $e^+e^- \rightarrow \Psi(3770) \rightarrow (D^0)(\overline{D}^0) \rightarrow (K^-e^+\nu_e)(K^+K^-)$. D^0 mass (top left), $\overline{D}^0$ mass (top left), $\Psi(3770)$ Mass (centre left), ΔE vs. M_{BC} correlation plot (centre right), Δt distribution (bottom left), Δz distribution (bottom right).

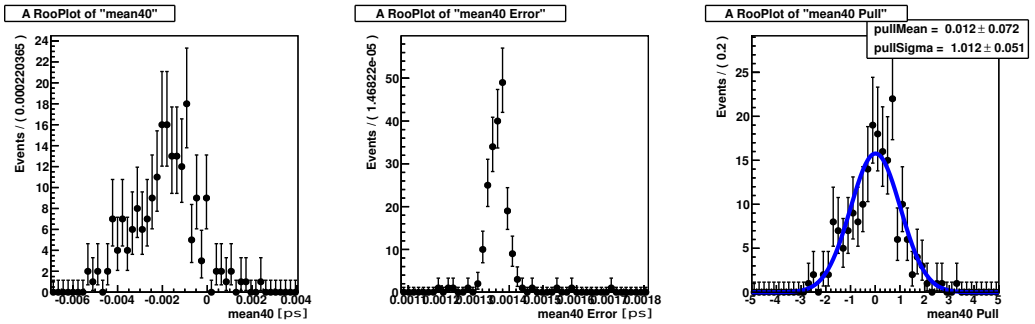

Figure A.2: Mean of the core Gaussian function (left), error on the mean (centre), and the pulls of the errors (right) for $e^+e^- \to \Psi(3770) \to (\overline{D}^0)(D^0) \to (K^+K^-)(K^-e^+\nu_e)$.

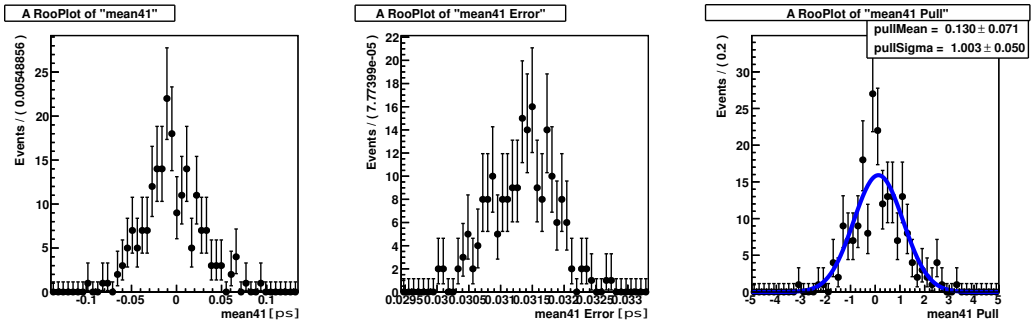

Figure A.3: Mean of the tail Gaussian function (left), error on the mean (centre), and the pulls of the errors (right) for $e^+e^- \to \Psi(3770) \to (\overline{D}^0)(D^0) \to (K^+K^-)(K^-e^+\nu_e)$.

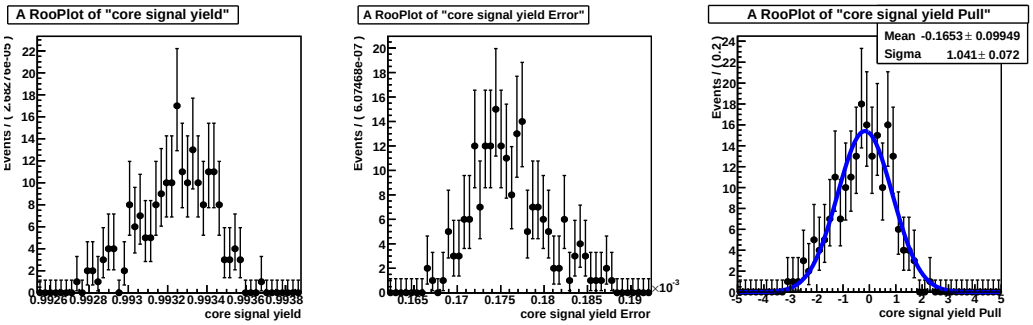

Figure A.4: Core signal fraction (left), error (centre), and the pulls of the errors (right) for $e^+e^- \to \Psi(3770) \to (\overline{D}^0)(D^0) \to (K^+K^-)\ (K^-e^+\nu_e)$.

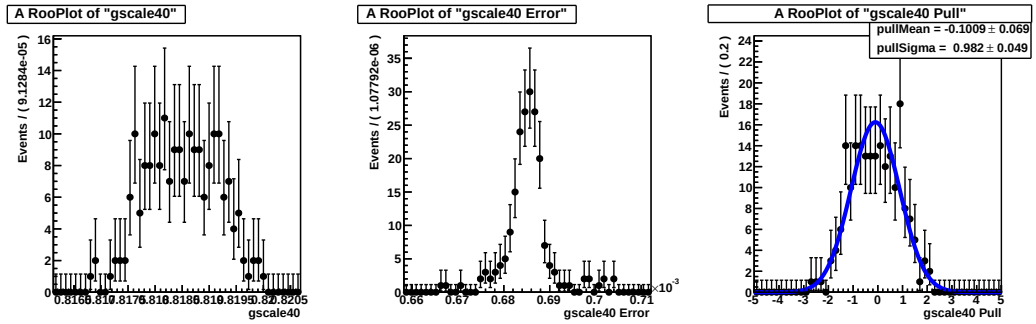

Figure A.5: Scale factor of the core Gaussian function (left), error (centre), and the pulls of the errors (right) for $e^+e^- \rightarrow \Psi(3770) \rightarrow (\overline{D}^0)(D^0) \rightarrow (K^+K^-)(K^-e^+\nu_e)$.

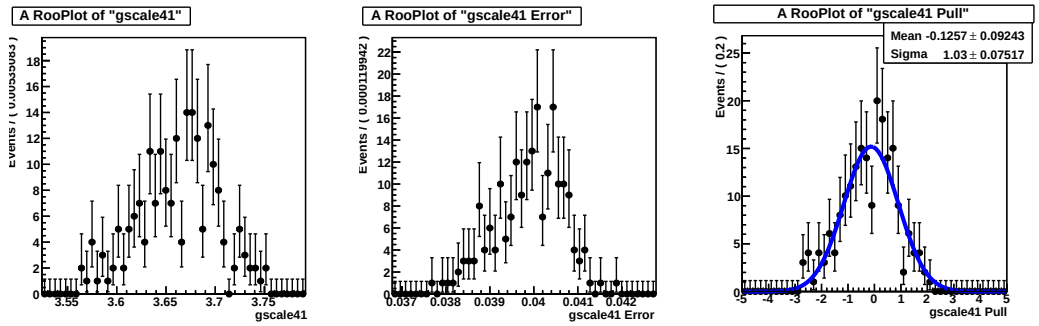

Figure A.6: Scale factor of the tail Gaussian function (left), error (centre), and the pulls of the errors (right) $e^+e^- \rightarrow \Psi(3770) \rightarrow (\overline{D}^0)(D^0) \rightarrow (K^+K^-)(K^-e^+\nu_e)$.

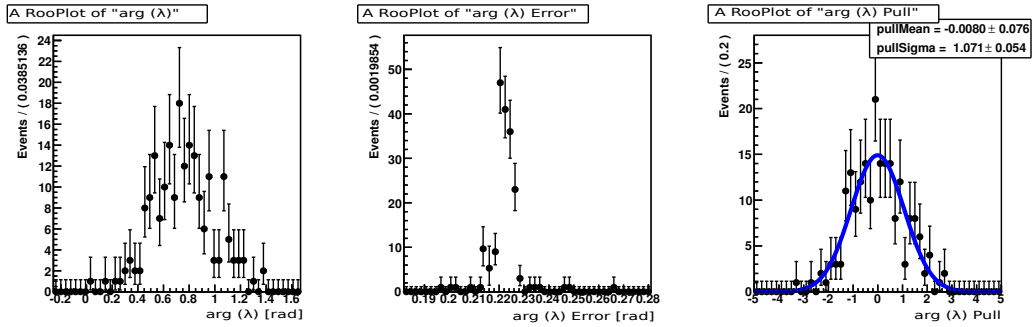

Figure A.7: Measured value of $\phi_{KK} = \phi_{MIX}$ (left), error on ϕ_{MIX} (centre), pulls of the errors (right).

Appendix B

B.1 $e^+e^- \rightarrow \Psi(3770) \rightarrow (D^0)(\overline{D}^0) \rightarrow (K^-e^+\nu_e)(\pi^+\pi^-)$

The study discussed in Chapter 4 has been applied to the decay chain $e^+e^- \rightarrow \Psi(3770) \rightarrow (D^0)(\overline{D}^0) \rightarrow (K^-e^+\nu_e)(\pi^+\pi^-)$, being this the charge conjugate chain of $e^+e^- \rightarrow \Psi(3770) \rightarrow (D^0)(\overline{D}^0) \rightarrow (\pi^+\pi^-)(K^+e^-\overline{\nu}_e)$. The Final distributions obtained after the selection criteria given in B.1 have been applied to the 200000 generated chains $e^+e^- \rightarrow \Psi(3770) \rightarrow (D^0)(\overline{D}^0) \rightarrow (K^-e^+\nu_e)(\pi^+\pi^-)$ are shown in Fig. A.1, for which an efficiency $\epsilon = 54.2\%$ was found, in agreement with what was observed in the decay chain $e^+e^- \rightarrow \Psi(3770) \rightarrow (D^0)(\overline{D}^0) \rightarrow (\pi^+\pi^-)(K^+e^-\overline{\nu}_e)$, where an efficiency $\epsilon = 52.9\%$ was found. Figures B.2-B.6 show the distributions of the central values, the errors, and pull of the errors, obtained from the RooFit study of the resolution function and Fig. B.7 shows the distributions of the central value, the errors, and the pulls of the errors for $\phi = arg[\lambda_f]$, showing a sensitivity on the latter $\sigma_\phi = 24.6°$, in agreement with the obtained sensitivity shown in Fig. 5.17 for the conjugate decay chain where $\sigma_\phi = 24.1°$ was found.

Table B.1: Allowed range of values for ΔE, M_{BC}, $\sigma_{\Delta t}$ and χ^2.

Parameter	min.	max.
ΔE [GeV]	-0.01	0.008
M_{BC} [GeV]	1.862	1867
$\sigma_{\Delta t}$ [ps]	-	10.0
χ^2	-	15

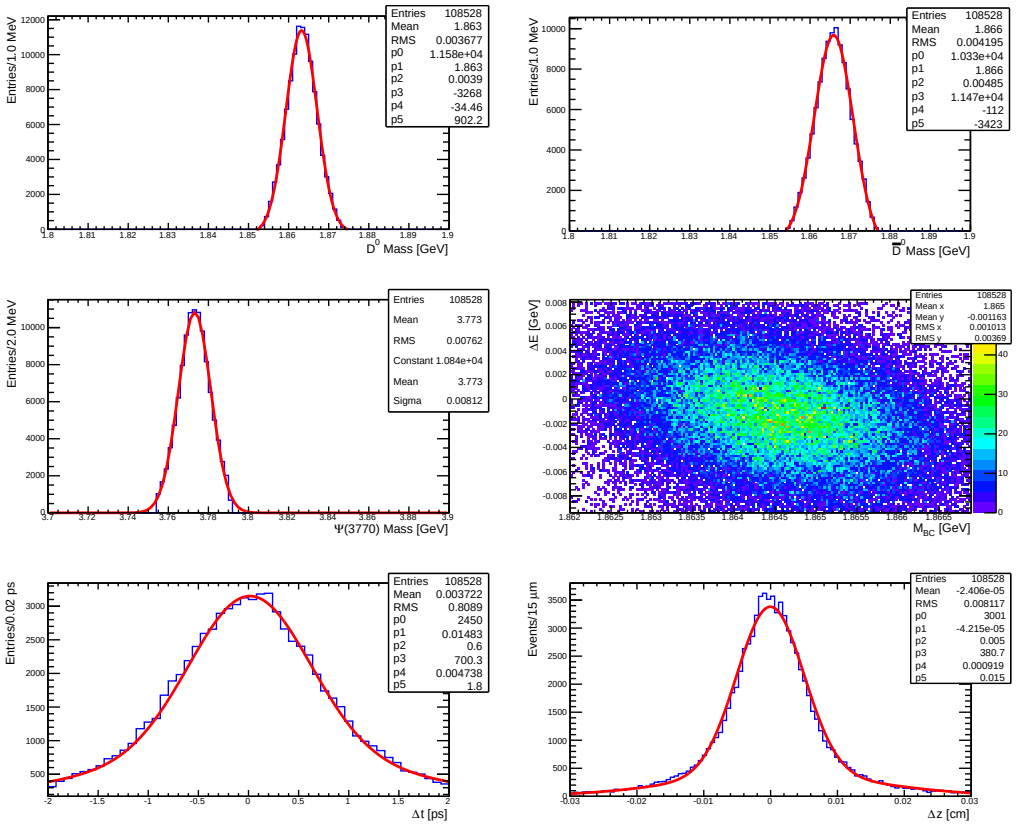

Figure B.1: Final distributions obtained after selection criteria have been applied to the 200000 generated chains $e^+e^- \to \Psi(3770) \to (D^0)(\overline{D}^0) \to (\pi^+\pi^-)(K^+e^-\overline{\nu}_e)$. $\overline{D}^0$ mass (top left), D^0 mass (top left), $\Psi(3770)$ Mass (centre left), ΔE vs. M_{BC} correlation plot (centre right), Δt distribution (bottom left), Δz distribution (bottom right).

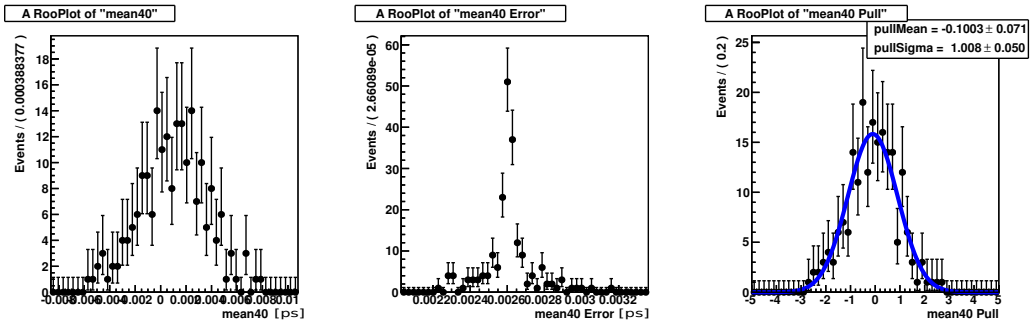

Figure B.2: Mean of the core Gaussian function (left), error on the mean (centre), and the pulls of the errors (right) for $e^+e^- \to \Psi(3770) \to (\overline{D}^0)(D^0) \to (K^+e^-\overline{\nu}_e)(\pi^+\pi^-)$.

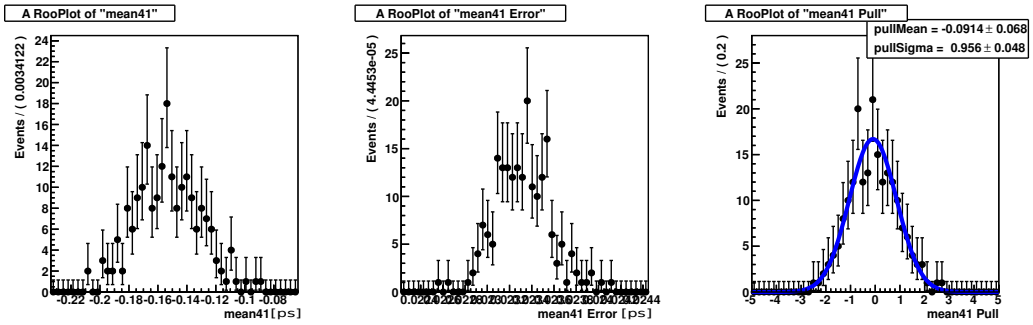

Figure B.3: Mean of the tail Gaussian function (left), error on the mean (centre), and the pulls of the errors (right) for $e^+e^- \to \Psi(3770) \to (\overline{D}^0)(D^0) \to (K^+e^-\overline{\nu}_e)(\pi^+\pi^-)$.

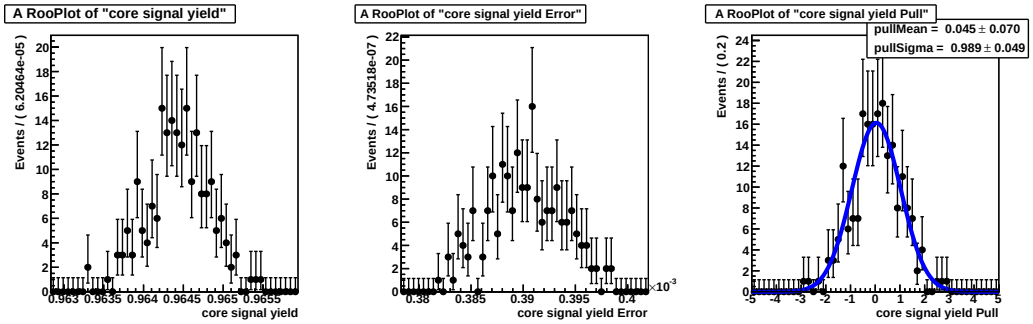

Figure B.4: Core signal fraction (left), error (centre), and the pulls of the errors (right) for $e^+e^- \to \Psi(3770) \to (\overline{D}^0)(D^0) \to (K^+e^-\overline{\nu}_e)\ (\pi^+\pi^-)$.

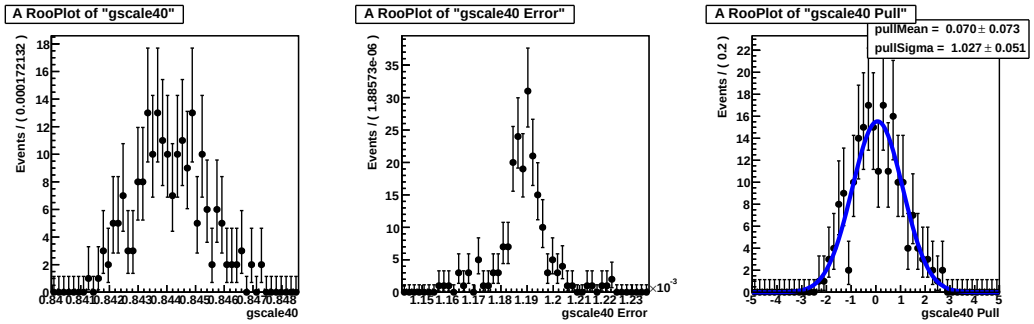

Figure B.5: Scale factor of the core Gaussian function (left), error (centre), and the pulls of the errors (right) for $e^+e^- \to \Psi(3770) \to (\overline{D}^0)(D^0) \to (K^+e^-\overline{\nu}_e)(\pi^+\pi^-)$.

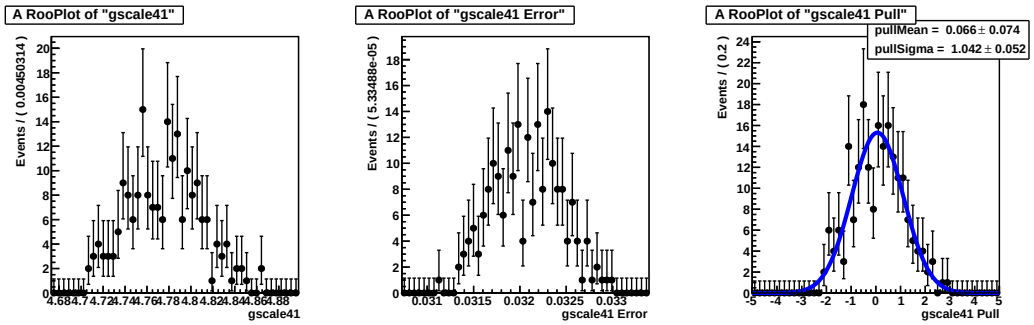

Figure B.6: Scale factor of the tail Gaussian function (left), error (centre), and the pulls of the errors (right) for $e^+e^- \to \Psi(3770) \to (\overline{D}^0)(D^0) \to (K^+e^-\overline{\nu}_e)(\pi^+\pi^-)$.

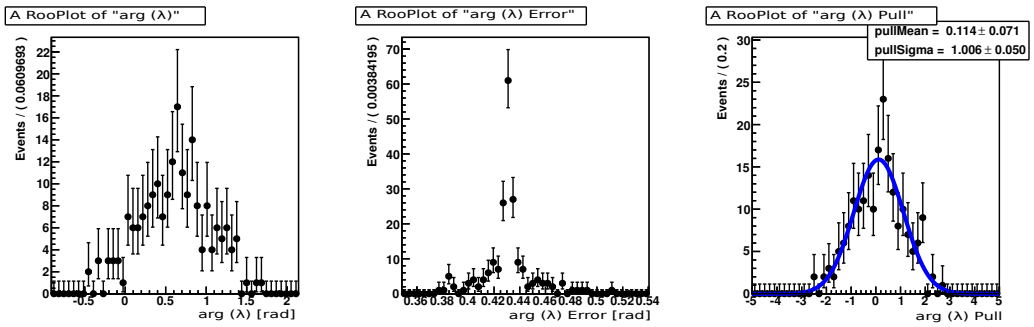

Figure B.7: $\phi_{\pi\pi} = \phi_{MIX} + 2\beta_{c,eff}$ (left), error on $\phi_{MIX} + 2\beta_{c,eff}$ (centre), pulls of the errors (right).

Appendix C

C.1 The case for an high luminosity τ-*charm* factory

C.1.1 An alternative approach for time dependent studies in symmetric collisions

After cancellation of the Super$B$ project in November 2012, the Cabibbo-Lab Consortium started work on preliminary studies for a smaller project, a high luminosity ($2 \times 10^{35} cm^{-2} s^{-1}$) τ-*charm* factory. Due to funding limitations various options (boost configuration) have been discarded to favour a symmetric beam energy machine. A method to study time-dependent CP asymmetries in symmetric B factories was proposed in 1995 [59]. I applied then the same methodology to the study of CP violation in the D^0 system. The method consists in the identification of the usual decays of interests (one for the tag and one for the CP side) in the x-y plane ignoring the effects along the z-axis as shown in Fig. C.1, where a schematic view of the process and the main quantity needed for the analysis are shown. Eqns C.1 and C.2 show the covariance matrices for a symmetric machine configuration.

$$C_{e^-,sym} = \begin{pmatrix} 3.10693 \times 10^{-7} & 0 & -3.48357 \times 10^{-8} \\ 0 & 7.71152 \times 10^{-8} & 0 \\ -3.48357 \times 10^{-8} & 0 & 1.47049 \times 10^{-6} \end{pmatrix}, \quad \text{(C.1)}$$

$$C_{e^+,sym.} = \begin{pmatrix} 3.10693 \times 10^{-7} & 0 & 3.48357 \times 10^{-8} \\ 0 & 7.71152 \times 10^{-8} & 0 \\ 3.48357 \times 10^{-8} & 0 & 1.47049 \times 10^{-6} \end{pmatrix}. \quad \text{(C.2)}$$

I generated a dataset of 158000 $\overline{D}^0 \to \pi^+\pi^-$, $D^0 \to K^-e^+\bar{\nu}_e$-tagged, equivalent to an integrated luminosity of 500 fb^{-1} with a symmetric machine configuration. To reject mis-reconstructed events we follow the procedure described in this thesis and in particular with selected events according to the limits shown in Tab. C.1. The analysis is performed along the y-direction[1],

Table C.1: Allowed range of values for ΔE, M_{BC}, $\sigma_{\Delta t}$ and χ^2.

Parameter	min.	max.
ΔE [GeV]	-0.007	0.05
M_{BC} [GeV]	1.863	1.8665
$\sigma_{\Delta t}$ [ps]	-	10.0
χ^2	-	15

by separating events in which the decay to a CP eigenstate is upward in the up-side of Fig. C.1 from those in which the decay to a CP eigenstate is downward in the down-side of Fig. C.1. In particular the variable y_f represent the y coordinate of the decay vertex of the D^0 ($\overline{D}^0$) decaying to the CP eigenstate, y_0 represents the D^0 ($\overline{D}^0$) production point, which is represented by the beamspot, and y_{tag} is the coordinate of the decay vertex of the D^0 ($\overline{D}^0$) decaying semileptonically. To observe CP violation one defines a new parameter, $\langle\overline{y}\rangle_\pm$ (+ for events where the decay to the CP eigenstate is in the top of Fig. C.1, − in the other case), which refers to the average difference between the y coordinate of the CP side decay and the y coordinate of the

[1]Due to the fact that the machine is configured for symmetric collisions a boost along the z-direction is not available so that it is not possible to perform a time-dependent analysis along that direction, so that one would prefer to perform a test on the other directions, x or y. Due to flatness properties of the beams on y one would choose it as a preferred direction where a potentially higher resolution on the decay vertex of a D^0 meson might be achieved

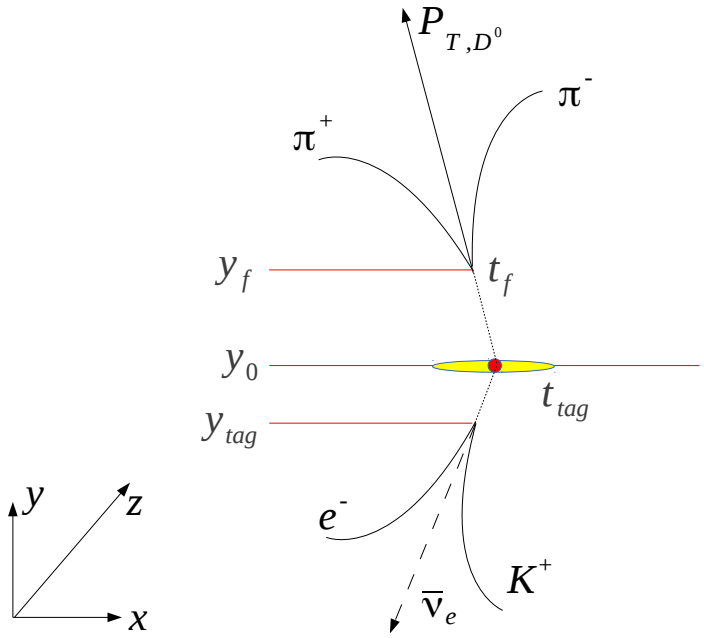

Figure C.1: Berkelman variables in typical D^0 and $\overline{D}^0$ decays.

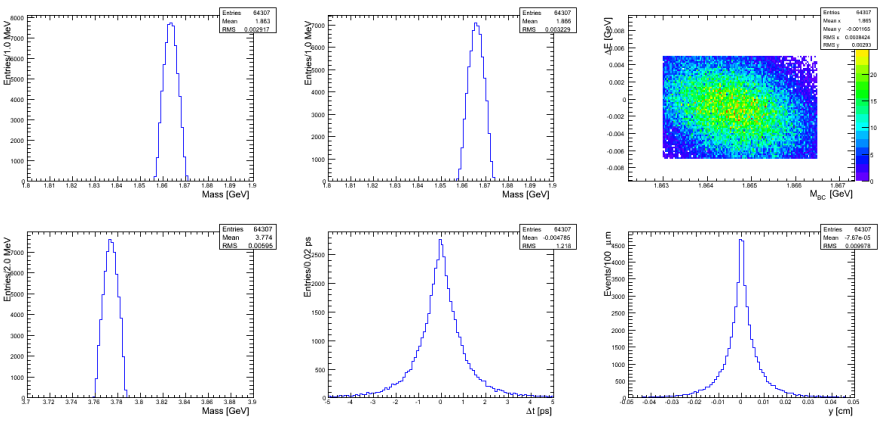

Figure C.2: Final distributions after selection criteria have been applied. $\overline{D}^0 \to \pi^+\pi^-$ mass (top left), $D^0 \to K^-e^+\bar{\nu}_e$ mass (top centre), M_{BC} vs. ΔE correlation plot (top right), $\Psi(3770) \to \overline{D}^0 D^0$ mass (bottom left), Δt distribution (bottom centre), y distribution (bottom right).

semileptonically decayed D^0 used to perform flavour tag. One takes the difference, on an event by event basis of $< \overline{y} >_{\pm}$ and y_0, and if the difference is non-zero, then CP has been violated. The results of this study are shown in Fig. C.3 where, looking at the two bottom figures, one can see that there is no sensitivity to CP violation with the generated set of events. The data show a low efficiency of 42.9% due to the fact that, while using symmetric collisions, I considered an asymmetric detector (no symmetric detector implementation was available for the project at the time of this study).

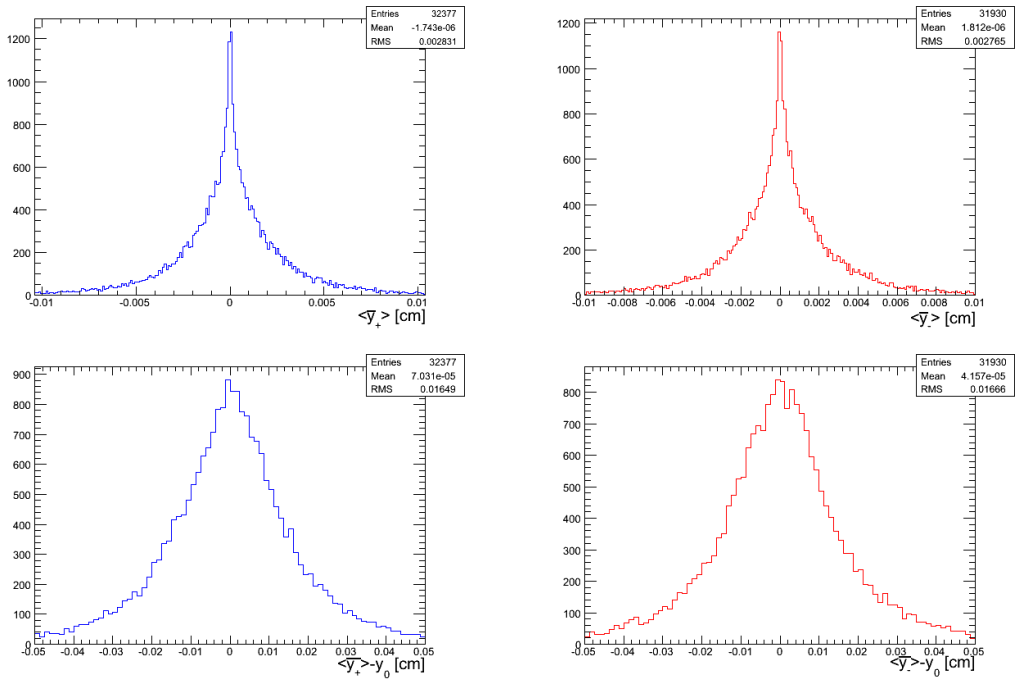

Figure C.3: Reconstructed $< \overline{y} >_+$ (top left), $< \overline{y} >_-$ (top right), $< \overline{y} >_+ - y_0$ (bottom left) and $< \overline{y} >_+ - y_0$ (bottom right). The two figures at the bottom show that no sensitivity on CP violation is achieved.

Bibliography

[1] A.D. Sakharov, Violation of CP Invariance, C Asymmetry, and Baryon Asymmetry of the Universe, Pisma Zh. Eksp. Teor. Fiz.: 5:32–35, 1967.

[2] J. H. Christenson, J. W. Cronin, V. L. Fitch, and R. Turlay, Evidence for the 2π decay of the k_2^0 meson, Phys. Rev. Lett. 13: 138–140, 1964.

[3] Bernard Aubert et al., *BABAR* Collaboration, Observation of direct CP violation in $B^0 \to K^+\pi^-$ decays, Phys. Rev. Lett. 93: 131801, 2004.

[4] Y. Chao et al., Belle Collaboration, Evidence for CP violation in $B^0 \to K^{+-}\pi^{-+}$ decays, Phys. Rev. Lett. 93: 191802, 2004.

[5] R. Aaij et al., LHCb Collaboration, First Observation of CP Violation in the Decays of B_s^0 Mesons, Phys. Rev. Lett. 110: 221601, 2013.

[6] R. Aaij et al., LHCb Collaboration, Observation of CP violation in $B^\pm \to D^0 K^\pm$ decays, Phys. Lett. B 712, 203, 2012.

[7] J. P. Lees et al. [*BABAR* Collaboration]. Observation of Time Reversal Violation in the B^0 Meson System, Phys. Rev. Lett. 109, 211801, 2012 [arXiv:1207.5832 [hep-ex]].

[8] http://www.isgtw.org/spotlight/go-particle-quest-first-cern-hackfest.

[9] HFAG Collaboration, arXiv: 1207.1158 [hep-ex], 2012, plus additonal updates on HFAG website: http://www.slac.stanford.edu/xorg/hfag/.

[10] S. Borghi, talk presented to the conference CHARM 2013.

[11] A. J. Bevan, G. Inguglia, B. Meadows. Time-dependent CP asymemtries in D and B decays. Phys. Rev. D 84, 114009, 2011, [arXiv:1106.5075 [hep-ph]].

[12] Nicola Cabibbo. Unitary symmetry and leptonic decays. Phys. Rev. Lett. 10, 531, 1963.

[13] M. Kobayashi and T. Maskawa. CP Violation in the Renormalizable Theory of Weak Interaction. Prog. Theor. Phys. 49, 652, 1973.

[14] J. Beringer et al. (Particle Data Group), Phys. Rev. D 86, 010001, 2012.

[15] L. Wolfenstein. Parametrization of the Kobayashi-Maskawa Matrix. Phys. Rev. Lett. **51**, 1945, 1983.

[16] M. Gersabeck et al., On the interplay of direct and indirect CP violation in the charm sector, arXiv:1111.6515 [hep-ph].

[17] LHCb Collaboration. Evidence for CP violation in time-integrated $D^0 \to h^+h^-$ decay rates. Phys.Rev.Lett. 108, 111602, 2012 [arXiv: 1112.0938 [hep-ex]].

[18] LHCb Collaboration. LHCb-CONF-2013-003, 2013.

[19] LHCb Collaboration. Phys. Lett. B 723 33-43, 2013, [arXiv: 1303.2614 [hep-hex]].

[20] E. Lunghi and A. Soni. Demise of CKM its aftermath, 2011, arXiv: 1104.2117 [hep-ph].

[21] CDF note 10784, 2012.

[22] B. R. Ko (Belle Collaboration), arXiv: 1212.1975v1.

[23] Y. Grossman, A. L. Kagan, Y. Nir. New Physics and CP Violation in Singly Cabibbo Suppressed D Decays, Phys. Rev. D 75, 036008, 2007 [arXiv: 0609178 [hep-ph]].

[24] J. Brod, Y. Grossman, A. L. Kagan, J. Zupan. A Consistent Picture for Large Penguins in $D \to \pi^+\pi^-, K^+K^-$, JHEP 10, 1210, 2012 [hep-ph ¿ arXiv: 1203.6659 [hep-ph]].

[25] A. Bevan, G. Inguglia, M. Zoccali. Neutral meson tests of time-reversal symmetry invariance, 2013, arXiv: 1302.4191 [hep-ph].

[26] J. S. Bell, Physics 1, 195, 1964.

[27] A. Bevan, B. Meadows. Bounding hadronic uncertainties in $c \to u$ decays, 2013, arXiv: 1310.0050 [hep-ph].

[28] M. Artuso et al. (CLEO Collaboration). Amplitude analysis of $D^0 \to K^+K^-\pi^+\pi^-$, Phys. Rev. D 85, 122002, 2012 [arXiv:1201.5716 [hep-ex]].

[29] D. M. Asner et al. (CLEO Collaboration). Determination of the $D^0 \to K^+\pi^-$ relative rtrong phase using quantum-correlated measurements in $e^+e^- \to D^0\overline{D}^0$ at CLEO. Phys. Rev. D 78, 012001, 2008, [arXiv: 0802.2268 [hep-ex]].

[30] P. del Amo Sanchez et al. (*BABAR* Collaboration). Measurement of D0-anti-D0 Mixing using the Ratio of Lifetimes for the Decays $D^0 \to K^-\pi^+$, K^-K^+, and $\pi^-\pi^+$. Phys. Rev. Lett. 105, 081803, 2010, [arXiv: 1004.5053 [hep-ex]].

[31] B. O'Leary et al. (SuperB), Super$B$ Progress Report - Physics - 2010, arXiv: 1008.1541.

[32] E. Grauges et al. (SuperB), Super$B$ Progress Report - Detector - 2010, arXiv: 1007.4241.

[33] M.E. Biagini et al. (SuperB), Super$B$ Progress Report - Accelerator - 2010, arXiv: 1009.6178.

[34] B. Meadows et al. (Super$B$), The impact of Super$B$ on flavour physics - 2011, arXiv: 1109.5028.

[35] Belle II Collaboration, Belle II Technical Design Report - 2012, arXiv: 1011.0352.

[36] Super$B$ Collaboration, Super$B$: a high luminosity asymmetric e^+e^- factory - 2007, arXiv: 0709.0451v2.

[37] M. Biagini, talk presented at the 2^{nd} Super$B$ Collaboration Meeting, 2011.

[38] F. Bosi, talk presented at the 2^{nd} Super$B$ Collaboration Meeting, 2011.

[39] A. J. Bevan, G. Inguglia et al. (Super$B$ Collaboration). Super$B$ technical design report, 2013. ArXiv: 1306.5655 [hep-ex].

[40] W. D. Hulsbergen, Decay chain fitting with a Kalman filter, Nucl. Instr. and Meth. A 552 556-574, 2005, arXiv: 0503191 [phys.comp-ph].

[41] B. Aubert et al., *BABAR* Collaboration, A Study of Time-Dependent CP-Violating Asymmetries and Flavor Oscillations in Neutral B Decays at the $\Upsilon(4S)$, Phys.Rev.D 66, 032003, 2002, arXiv: 0201020 [hep-ex].

[42] B. Aubert et al., *BABAR* Collaboration, Measurement of Time-Dependent CP Asymmetry in $B^0 - > c\bar{c}K(*)^0$ Decays, Phys.Rev.D 79, 072009, 2009, arXiv: 0902.1708 [hep-ex].

[43] TowerJazz Semiconductor Ltd. Home Page. http://www.towerjazz.com/

[44] G. Aad et al., ATLAS pixel detector electronics and sensors, J. Instrum., 3 P07007, 2008.

[45] L. Vitale et al., SLIM5 beam test results for thin striplet detector and fast readout beam telescope, Nucl. Instr. and Meth. A, 617 p. 601, 2010.

[46] ARACHNID Collaboration research proposal, https://heplnm061.pp.rl.ac.uk/pages/viewpage.action?pageId=8716393, 2012.

[47] C. Troncon, Radiation hardness performance of ATLAS pixel tracker, Nucl. Instr. and Meth. A, 2010.

[48] R. E. Coath, J. P. Crooks, A. Godbeer, M. D. Wilson, Z. Zhang, M. Stanitzki, M. Tyndel, and R. A. D. Turchetta, A Low Noise Pixel Architecture for Scientific CMOS Monolithic Active Pixel Sensors, Nuclear Science, IEEE Transactions, Sci. Vol. 57, No. 5, 2010, 2490-2496.

[49] M. Stanitzki, Advanced monolithic active pixel sensors for tracking, vertexing and calorimetry with full CMOS capability, Nucl. Instr. and Meth. A, 2010.

[50] J. A. Ballin et al., Monolithic Active Pixel Sensors (MAPS) in a quadruple well technology for nearly 100% fill factor and full CMOS pixels, arXiv: 0807.2920, 2008.

[51] CERN, short introduction to the use of H6 beam, version 3.0, 2000.

[52] EUDET Pixel Telescope Data Taking Manual - Version CERN TB, 2011.

[53] T. Nooney et al., Intrinsic n-well MAPS for particle physics, PoS (EPS-HEP), 507, 2013.

[54] ARACHNID confluence website. https://heplnm061.pp.rl.ac.uk/display/arachnid/Results+and+Plots.

[55] L. Landau, On the Energy Loss of Fast Particles by Ionization, J. Phys. USSR 8, 201, 1944.

[56] F. Wilson, Experimental results with the Cherwell 1 sensor. Talk presented at IPRD conference, Siena, 2013.

[57] Private communications with Jaap Velthuis (University of Bristol).

[58] Internal communications within the ARACHNID Collaboration.

[59] K. Berkelman, CP violation in neutral B decays on the $\Upsilon(4S)$ with symmetric energies, Mod. Phys. Lett. A 10, 165-172, CLNS-94-1310, 1995.